NOVEL UPCONVERSION NANOSTRUCTURE FOR HIGH EFFICIENCY PHOTOVOLTAICS: THEORETICAL MODEL AND MATERIAL STUDY

by

Jing Zhang

A dissertation submitted to the Faculty of the University of Delaware in partial fulfillment of the requirements for the degree of Doctor of Philosophy in Chemistry and Biochemistry

Fall 2018

NOVEL UPCONVERSION NANOSTRUCTURE FOR HIGH EFFICIENCY PHOTOVOLTAICS: THEORETICAL MODEL AND MATERIAL STUDY

by

Jing Zhang

Approved: _____
Brian J. Bahnson, Ph.D.
Chair of the Department of Chemistry and Biochemistry

Approved: _____
John A. Pelesko, Ph.D.
Interim Dean of the College of Arts and Sciences

Approved: _____
Douglas J. Doren, Ph.D.
Interim Vice Provost for Graduate and Professional Education

I certify that I have read this dissertation and that in my opinion it meets the academic and professional standard required by the University as a dissertation for the degree of Doctor of Philosophy.

Signed: _____

Joshua M. O. Zide, Ph.D.
Professor in charge of dissertation

I certify that I have read this dissertation and that in my opinion it meets the academic and professional standard required by the University as a dissertation for the degree of Doctor of Philosophy.

Signed: _____

Lars Gundlach, Ph.D.
Professor in charge of dissertation

I certify that I have read this dissertation and that in my opinion it meets the academic and professional standard required by the University as a dissertation for the degree of Doctor of Philosophy.

Signed: _____

Matthew F. Doty, Ph.D.
Member of dissertation committee

I certify that I have read this dissertation and that in my opinion it meets the academic and professional standard required by the University as a dissertation for the degree of Doctor of Philosophy.

Signed: _____

Andrew V. Teplyakov, Ph.D.
Member of dissertation committee

I certify that I have read this dissertation and that in my opinion it meets the academic and professional standard required by the University as a dissertation for the degree of Doctor of Philosophy.

Signed: _____

Karl S. Booksh, Ph.D.
Member of dissertation committee

ACKNOWLEDGEMENTS

It's been a great journey. I would not have had this achievement without the help from many people. First, I would like to express my deep appreciation to my advisor Dr. Joshua Zide. I'm grateful that Josh gave me the opportunity to explore an area of study which is very different from my undergraduate background. He provided valuable advice throughout my time in the lab. Josh and Dr. Matthew Doty gave me enormous amount of freedom in research, and were always ready to offer help whenever needed. I really appreciate the patient guidance and encouragement they have provided. I'm also grateful that Josh trusted me with responsibilities in running the MBE. He was very supportive and understanding during the the difficult time with the MBE.

Also I would like to thank my committee members Dr. Matthew Doty, Dr. Lars Gundlach, Dr. Andrew Teplyakov and Dr. Karl Booksh. They have provided many helpful advice for the dissertation. To Dr. Gundlach, thank you for kindly agree to be the chair of the committee. To Dr. Teplyakov, thank you for giving very detailed advice to the dissertation. To Dr. Booksh, thank you for offering help with the job-searching.

I really enjoy the 5 years in the Zide group. I couldn't ask for a more friendly group environment. Many thanks to our current group members Yuejing (Crystal) Wang, Dr. Eric Chen, Bo Tew, Lauren McCabe, James Bork and Dr. Bruce Chase. I appreciate the help provided by Crystal, Lauren and James, together with Dongxia Wei and Patrick Sohr from the Law group, on the MBE growth and maintenance. I enjoy working with Eric on the upconversion project. I want to thank our former group members Dr. Matthew Lewis, Dr. Cory Bomberger, Dr. Pernell Dongmo and Dr. Yujun Zhong. I have learned so much from Cory and Pernell. Matt and Bo provided a lot of help with the research and MBE maintenance. I want to thank the

undergraduate students that I have worked with, Charlie Jabbour and Noah Kennedy. I want to thank Mr. Kjeld Jensen for all the generous help and support. I also want to thank Dr. Robert Opila, for I would not have had the chance to work with all these awesome people without his kind referral.

I want to extend the gratitude to all my friends here in UD and in other parts of the United States. I enjoyed the times we have spend together. I will always miss the trips that we have took. I would like to thank Grand master Thomas Welsh, my taekwon-do instructor. I was extremely lucky to have the opportunity to learn from Master Welsh. Thanks to all the friends I have met in the taekwon-do practice. You all make me feel at home.

Finally, I want to thank my families. Completion of the dissertation is not possible without the unconditional support from my parents and my sister.

TABLE OF CONTENTS

LIST OF TABLES

LIST OF FIGURES

ABSTRACT

Upconversion is a process that converts two low energy photons to one high energy photon. It could be applied to solar cell to increase the solar power conversion efficiency. A novel upconversion nanostructure consisting of InAs quantum dots (QDs) and Al-containing dilute Bismuthides was proposed previously[92]. Here I will discuss the kinetic rate equation model that was developed to describe the kinetic processes and predict the upconversion nanostructure performance. Combined with detailed balance approach for the solar cell, the calculation showed that the structure could potentially improve the solar cell performance significantly. We also analyze the robustness of the model by considering how the performance of both the upconverter and an upconverter-backed solar cell are affected by variations in the assumptions made in the model, including QD absorption cross section, solar spectrum splitting and carrier lifetimes. We further analyze the performance of the nanostructure as a function of solar concentration. The theoretical performance of this upconversion paradigm under concentrated sunlight exceeds 60% solar energy conversion efficiency. Moreover, the results show that the predicted performance is relatively insensitive to the assumptions made in the model, suggesting that practical realization of such a semiconductor upconverter heterostructure paradigm is possible.

Incorporating a small amount of bismuth could cause a large band gap reduction. Previous studies on GaBiAs and InGaBiAs have shown that the band gap reduction occurs mostly in the valence band[64, 5]. This property is helpful for application in the aformentioned upconversion nanostructure. MBE growth of Al-containing dilute bismuthides (In)AlBiAs at low temperature was demonstrated. Good quality InAlBiAs thin films was achieved. However, AlBiAs growth condition needs to be further explored to improve the material quality. We estimate band gap reduction from Bi

incorporation of 47 meV/%Bi and 63 meV/%Bi for InAlBiAs and AlBiAs respectively (linear band gap reduction value is often used when discussing the Bi-induced band gap reduction). The experimental determined InAlBiAs band gap agree with valence band anticrossing (VBAC) theory fairly well when Bi% is less than 3%. Further investigation on the VBAC model and optimization of the (In)AlBiAs quality are needed.

Chapter 1

TOWARDS HIGH EFFICIENCY SOLAR CELL

Global energy demand is projected to expand by 30% between 2017 and 2040, which is the equivalent of adding another China and India to today's global consumption[3]. Transitioning towards renewable energy is the approach to both reducing greenhouse gas emission in combating the global climate change, and ensuring energy security. Among the renewable energy sources, solar energy is the fastest growing. In recent years, the solar market has been growing strongly as a result of cost reduction and policy support, surpassing the growth of any other fuel. New PV capacity around the world grew by 50%, reaching over 74GW in 2016[2]. International Energy Agency forecasts that the total global PV capacity reaches 740 GW by 2022, with the capacity addition well above wind and hydro[2]. Improvement on the solar cell efficiency can further drive the growth. Upconversion, together with other techniques, shows great potential in improving solar cell efficiency.

This chapter is focused on the introduction to the background information related to the research, which includes the theory and research development of PV technology(section 1.1 and section 1.2, and finally on the upconversion(section 1.3).

1.1 Efficiency Limit of Solar Cells

In a solar cell, sunlight is absorbed in the semiconductor material, where electron-hole pairs are generated. The applied electric field across the p-n junction separates the electrons and holes that flow through and power the external load (see figure 1.1).

The main loss mechanisms in the solar cell operation are: 1) the photons with energy lower than the band gap cannot be absorbed; 2) photons with energy higher than the band gap lose the extra energy through thermalization (figure 1.2. The theoretical

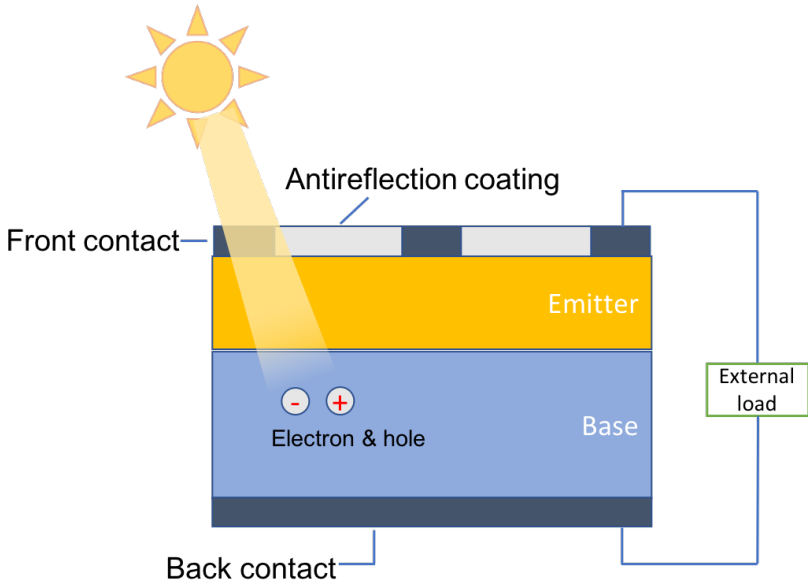

Figure 1.1: Solar cell structure [81]

efficiency limit for a single junction solar cell is called Shockley-Queisser limit, and could be derived from detailed balance method which will be discussed in the following text.

1.1.1 Detailed Balance Model

The efficiency of the solar cell is presented in the form of power conversion efficiency η, which is defined as the fraction of the power of the incident sunlight that is converted to electricity:

$$\eta = \frac{P_{SC}}{P_{inc}} = \frac{J \cdot V}{P_{inc}} \tag{1.1}$$

where P_{SC} is the power of the solar cell, J is the current, V is the voltage, and the P_{inc} is the power of the incident sun light. The net solar cell power conversion efficiency is calculated with the detailed balance model introduced by Shockley and Queisser in 1961[97]. We could assume complete absorption of photons above the band gap by the solar cell, and that each photons absorbed creates exactly one pair of electron and hole.

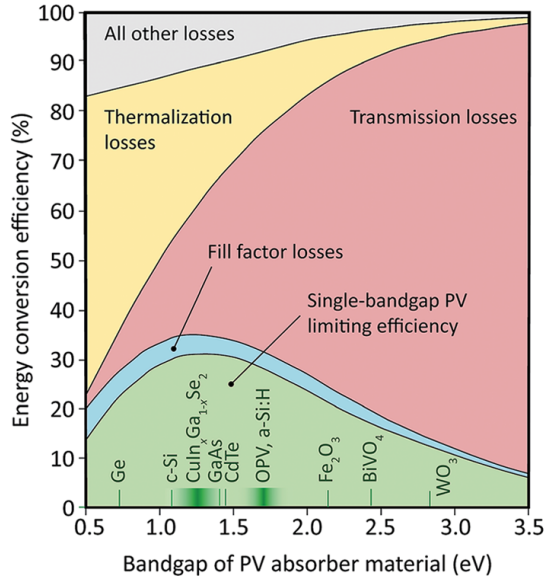

Figure 1.2: Fundamental loss mechanisms in solar cell operation as a function of the band gap [51]

The absorption of sub-band gap photons is zero. The detailed balance model examines all the electron generation and recombination process to extract the electrical current flow out of the cell to power up the external device, i.e.,

$$\begin{aligned} \varphi_{out} =& \varphi_{ab} - \varphi_{emi} \\ J =& e \cdot (\varphi_{ab} - \varphi_{emi}) \end{aligned} \tag{1.2}$$

where φ_{ab} is the absorption flux, φ_{emi} stands for the emission flux, and e is the electron charge. The thermal radiation could be described in the form of Plank's distribution for blackbody radiation:

$$\varphi(E_a, E_b, T, \mu) = \frac{2\pi}{c^2 h^3} \int_{E_a}^{E_b} \frac{E^2}{exp(\frac{E-\mu}{k_B T}) - 1} dE \tag{1.3}$$

$$\varphi_{emi}(E_g, \infty, T, \mu) = \frac{2\pi}{c^2 h^3} \int_{E_g}^{\infty} \frac{E^2}{exp(\frac{E-\mu}{k_B T}) - 1} dE \tag{1.4}$$

$$\approx J_0\Big(exp(\frac{eV}{k_B T})) - 1\Big) \tag{1.5}$$

$$\text{where } J_0 = \frac{2\pi}{c^2 h^3} \int_{E_g}^{\infty} \frac{E^2}{exp(\frac{E}{k_B T}) - 1} dE \tag{1.6}$$

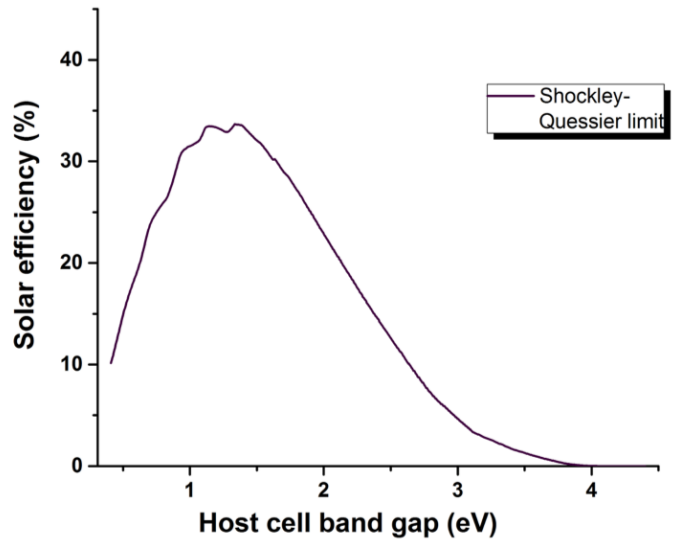

Figure 1.3: Solar energy conversion efficiency limit for a single junction cell, calculated with AM1.5-global spectrum[1]

where μ is the quasi-Fermi level separation. J_0 is called saturation current. The current in the solar cell could be rewritten as:

$$J = e\varphi_{ab} - J_0\Big(exp(\frac{eV}{k_B T}) - 1\Big) \tag{1.7}$$

$$= J_L - J_0\Big(exp(\frac{eV}{k_B T}) - 1\Big) \tag{1.8}$$

In the work presented in this dissertation, AM1.5 spectrum at 1976 US standard atmosphere (288.15K @ 1 atm) is applied to calculate the P_{inc} and J_L. The efficiency limit of single junction solar cell illuminating under one sun condition, with band gap ranging from 0.4 eV to 4.3 eV calculated from the detailed balanced method is shown in figure 1.3. The maximum solar cell efficiency is 33.7%, occurring around band gap value of 1.3 eV. For the most popular solar cell material, silicon, the efficiency limit is calculated to be 32%.

1.2 Emerging Technologies for High Efficiency Solar Cell

Solar cells could be classified into three generations. The first generation solar cell is the traditional crystalline silicon based solar cell. Thin film solar cells, such as amorphous silicon, CdTe and CIGS cells are called second generation cells. The third generation of solar cells includes both new cell materials like dye-sensitized solar cell (DSSC), organic solar cell and perovskite cells, and new technologies to increase the solar cell efficiency past the Shockley-Queisser efficiency limit, such as multi-junction solar cell. Third generation aiming at achieving high solar conversion efficiency, thus reducing the cost per watt since smaller area is needed for power generation. The goal is to reduce the cost from $1 per watt to $0.5, or potentially $0.2 per watt [26].

The efficiency of single junction GaAs and Si solar cell has reach 27.8% and 26.1% respectively [40], close to the Shockley-Queisser limit. As mentioned in section 1.1, the thermalization of hot carriers and transmission of sub-band gap photons are the main loss pathways of the solar energy (figure 1.2). In this dissertation, the transmitted sub-bandgap photons are called low energy photons, corresponding to the high energy photons that refers to the photons with energy higher than the solar cell band gap. The approach to solving the challenge of further increasing efficiency is to maximize the utilization of solar spectrum by harvesting the lost energies, either from the transmitted low energy photons or the thermalization losses of the high energy photons. This could be achieved by introducing multiple energy levels into the system to effectively collect photons with different energies, or by capturing carriers before thermalization. There are several implementations that work on different mechanisms, which will be discussed in details in the following sections.

Multi-junction solar cell, or tandem solar cell, combines p-n junctions of different materials into the stack, each section can absorb different photon energies, thus increasing the efficiency by broadening the solar spectrum absorption range. The highest solar cell efficiency is 46.5%, achieved with a 4-junction cell by Tibbits et al. [105]. The predicted efficiency limit depends on the number of subcells. The maximum is

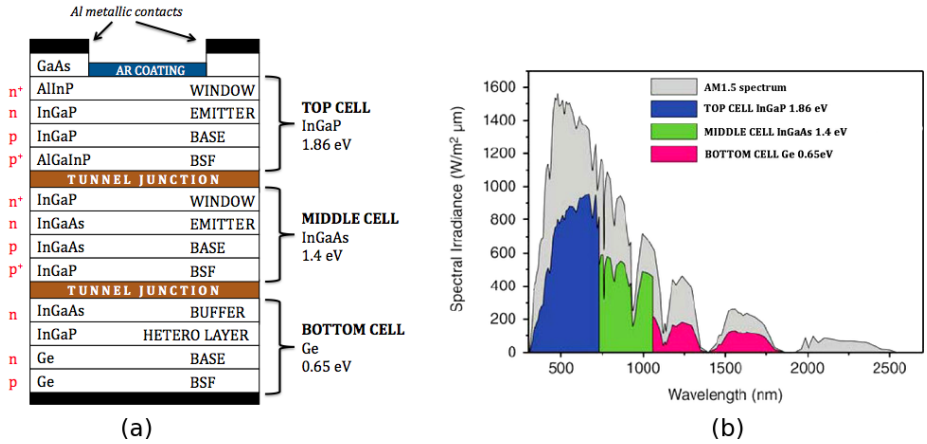

Figure 1.4: Left: Structure of multi-junction solar cell[73]. Right: AM1.5 solar spectrum, with the maximum electricity conversion efficiency for every junction as a function of the wavelength[67].

68.2%(unconcentrated sunlight) and 86.8%(concentrated sunlight) with infinite number of subcells[110]. However, for the multiple subcells connected in series, the current is very sensitive to spectral variation during the day, for terrestrial application.

Intermediate band solar cell (IBSC) contains an intermediate band (IB) materials between the original p- and n- section of the original single-junction solar cell (Fig.1.5). By introducing an IB between the conduction and valence band, the sub-bandgap photons could be absorbed through the VB to IB, and IB to CB transitions, in addition to the VB to CB transition. Theory based on the detailed balance model suggested IBSC efficiency could reach 47%[59]. However, the impurity band could also be non-radiative recombination center, which prevents overall gain of extra current from low energy photon harvesting. relaxation of excited electrons to IB is very fast. Quantum dots (QD) could be used to generate IB. QD-IBSC are most widely studied, however, no experimental cell have been able to demonstrate an increase of solar cell efficiency compared to a single-junction reference cell. They all suffer from inability to preserve voltage[60]. Using novel HMA Bulk IB materials like ZnTeO, has been reported to have an 50% increase of power conversion efficiency compared to the ZnTe reference cell[113].

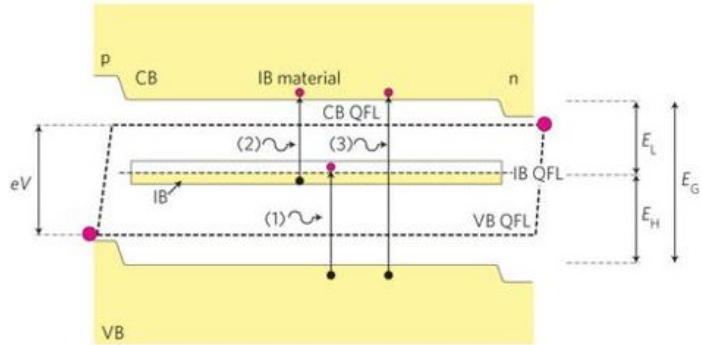

Figure 1.5: Band diagram of an intemediate band solar cell, (1) and (2) represent sub-band gap photon absorption and (3) represents above-band gap photon absorption.[60]

Another way to increase the solar cell efficiency past Shockley-Queisser limit for single junction cell is upconversion, which will be discussed more thoroughly in the next section.

1.3 Upconversion: Principle and Progress

Instead of introducing multiple band gaps within the solar cell, one can recycle the low energy photons by converting them into high energy photons through a process called upconversion. Upconversion is very useful in various applications, such as bioimaging[30], medical therapy[111], lasers[90], and photovoltaics. In the upconversion process, two or more low energy photons are absorbed and promote an electron from ground state to high energy excited state through an intermediate state, the relaxation of the electron emits one high energy photon. Gibart et al. proposed to apply upconversion process to enhance solar cell efficiency in 1996, and demonstrate the feasibility with a ultra thin GaAs cell[39]. Trupke et al. first constructed a theoretical model that predicted a maximum solar cell efficiency of 47.6% under non-concentrated light.

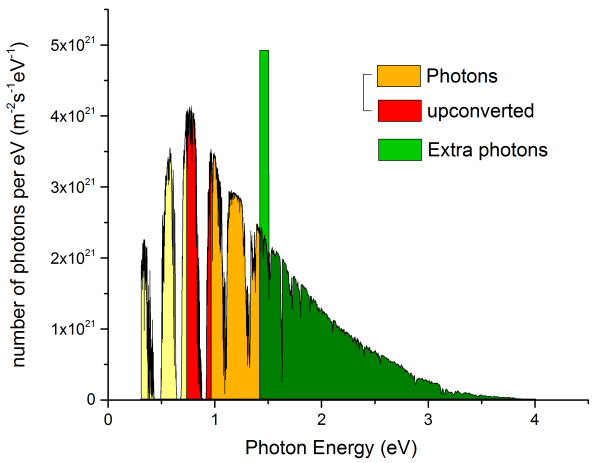

Figure 1.6: AM1.5 spectrum with the orange and red sections representing the low energy photons to be upconverted, the emitted high energy photons in bright green. The effective photon flux for the solar cell is the bright green plus dark green.

1.3.1 Constraints and Requirements on the Upconverting System

An upconversion device, or upconverter, will be placed on the back of the solar cell, electrically isolated from the solar cell with an transparent insulating layer as back contact (as shown in figure.1.7 (a)). The low energy photons that transmit through the solar cell will be converted into high energy photons in the upconversion layer. The reflective layer helps reflecting the high energy photons to the solar cell to be utilized. Integrating an upconversion layer, with the solar cell can increase the effective photon flux on the solar cell, thus increasing the photocurrent while still preserving the voltage. With the upconversion layer being electrically isolated from the solar cell, the intermediate-energy states utilized for low-energy photon absorption are not located within the host solar cell. The addition of the upconversion layer will not degrade the solar cell performance, which is a key advantage of upconversion compared to IBSC. The performance of the solar cell and upconversion materials could be independently optimized.

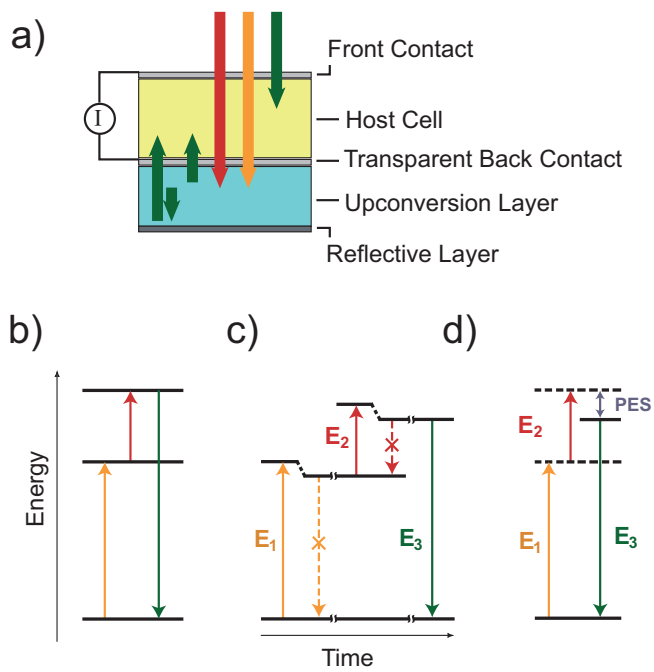

Figure 1.7: a). Schematic of a single-junction solar cell backed by an upconverter. High energy photons (green) is absorbed by the host solar cell, while low energy photons (orange and red) transmit through to be converted to high energy photons and return to the host cell. Schematic depiction of upconversion process with b): no energy loss, c)-d): intentional energy loss used to suppress radiative and nonradiative loss.[93]

Schematic upconversion process is shown in figure 1.7(b). Sequential low energy photon absorption excites the electron to high energy state, and the radiative recombination of the electron across the entire gap emits one high energy photon. The upconversion efficiency is limited by relaxation after each absorption step. To improve the efficiency, it is necessary to move the electron to a lower lying state after excitation to suppress the radiative and non-radiative loss(figure 1.7 (c) and (d)).

Photon energy sacrifice (PES) is defined as the intentionally introduced energy lost during the upconversion process, analogous to the relaxation energy defined by Trupke[107]. In Trupke's work, including some amount of relaxation energy, which comes from allowing the electrons or holes in excited states to relax to slightly lower energy states, improves the upconversion efficiency significantly[9]. The theoretical maximum of 47.6% solar cell efficiency is achieved based upon 330 meV of relaxation energy in the system. Some intemediate band solar cell designs have also adopted this concept of photon ratchet and proposed to implement with a quantum cascade design [118, 27].

Another important parameter in the upconversion system is the absorption bandwidth (AB), which is the spectral range of low-energy photons that can be absorbed by the upconversion material. For an upconverison system to make a significant improvement on the solar cell efficiency, AB should be engineered to be as wide as possible.

1.3.2 Upconverting Materials/Systems

Upconversion has been observed in various material systems. There are three typical upconversion materials available for photovoltaics application. One is the rare-earth-doped nanocrystals known as Lanthanides (e.g. $NaYF_4 : Er^{3+}, Yb^{3+}$) [36, 112]. The most efficient upconversion mechanism in Ln involving two ions is that the excitation energy of two ions in close vicinity is transferred by energy transfer resulting in one ion to be found in a higher excited state whereas the other ion is in a lower excited state, known as the energy transfer upconversion (ETU). The typical absorption

bandwidth of the Yb^{3+} ion sensitizer in Lanthanide materials is around 40 nm with a small absorption cross section; using organic dyes as the absorber could expand this range[114]. Current state of the art Lanthanides-doped nanocrystals could achieve upconversion efficiency of more than 16% [85].Multiple core-shell structure spatially separating different rare-earth ions could avoid the cross relaxation between the ions while widening the absorption bandwidth. Shao et al. demonstrated absorption bandwidth of 270 nm with $NaYF_4 : 10\%Er^{3+}@NaYF_4@NaYF_4 : 10\%Ho^{3+}@NaYF_4@NaYF_4 : 1\%Tm^{3+}@NaYF_4$ multiple core-shell structure [115]. Lanthanide ions doped upconversion layer integrated with solar cell has been demonstrated on various solar cell materials, including c-Si, a-Si, DSSC, and achieved noticeable improvement on the cell efficiency [28, 31, 58].

The other popular upconversion material is the organic molecules upconverting based on triplet-triplet annihilation (TTA) process that uses conjugated molecules as emitters and organometallic complexes as a sensitizer[98, 10], which is more promising compared to the rare-earth doped nanocrystals since it has higher upconversion quantum efficiency even at lower excitation power, for example, more than 30% upconversion quantum yield [77, 24]. In the upconversion process, a sensitizer is excited to the lowest singlet state and relaxes through intersystem crossing to the triplet state. The triplet state of the sensitizer transfers the energy to the emitter triplet state. Two emitter molecules in the triplet state annihilate yielding one emitter in the high energy singlet state that emit an high energy photon, and one in the ground state (see figure 1.8). Typical TTA systems have a narrow absorption bandwidth of tens of nm [14]. Recent advances that include multiple sensitizers could increase the absorption bandwidth in TTA systems to more than 100 nm[71, 44, 23]. Schulze et al. demonstrated a 0.2% increase in photocurrent under concentrated sunlight in a TTA-UC solar cell integrated system, and calculated to show that the maximum current enhancement from the PQ4PdNA sensitizer on a-Si:H solar cell could be $0.4mA/cm^2$.[91]. However, current successful TTA system emits at short wavelength ($\leq$780nm). Therefore for most solar cells, TTA cannot enhance the efficiency significantly. It could, however,

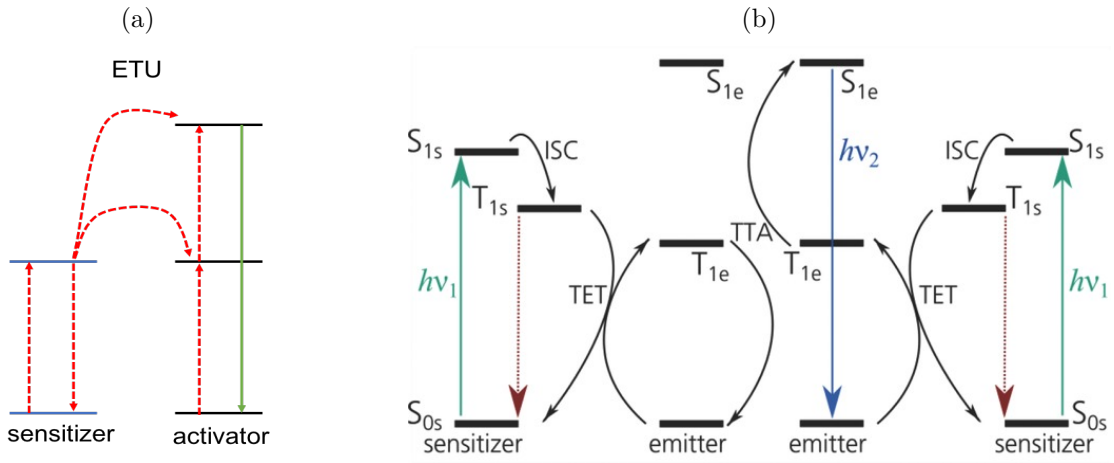

Figure 1.8: a) Energy transfer upconversion process in Lanthenides upconversion system (based on figure in reference [96]; b) The process in TTA upconversion. The singlet state S_{1s} of the sensitizer molecules is excited low-energy photons, followed by intersystem crossing (ISC) into the long-lived triplet state T_{1s}. Triplet–triplet energy transfer (TET) excites emitter molecules to their lowest triplet state T_{1e}. TTA excites a high-energy singlet state S_{1e} in one of the emitter molecules. Radiative decay into the ground state leads to the emission of one upconverted photon.[41]

work well with wide band gap solar cells, such as DSSC. TTA-backed DSSC has been demonstrated to achieve large photoncurrent enhancement of 18.8% and 35.2% under 1- and 2-sun illumination[57]. TTA is also used to construct IBSC [51].

The third type of material for application on photovoltaics is semiconductor quantum nanostructures. By carefully tailoring the band alignment in the nanostructure consisting of different compound semiconductor materials, the second photon absorption can be achieved through two step two photon absorption or Auger mediated energy transfer[32, 33]. Compared to the molecular systems, the semiconductor-based upconversion has the advantage of broad absorption bandwidth as well as good control of the electronic band structure. The Oron group demonstrated upconversion from near infrared to visible wavelengths in colloidally-synthesized PbSe/CdSe/CdS core/shell QDs under pulsed optical excitation [102] (see figure.1.9), as well as in the

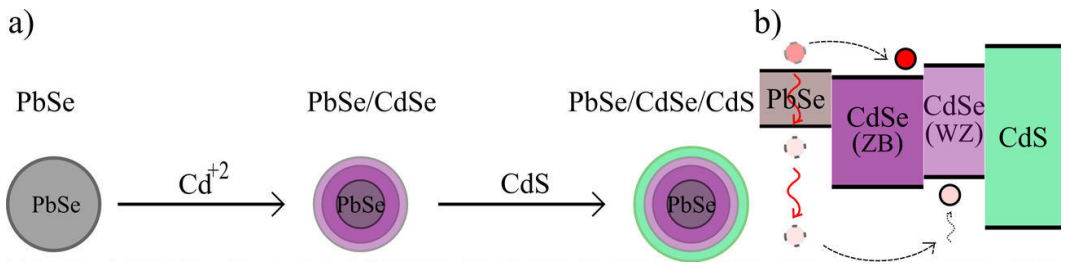

Figure 1.9: PbSe/CdSe/CdS upconversion structure and band alignment. [102]

system consisting two CdSe(Te) QDs seperated by CdS tunneling barrier that upconverts 680nm into 570nm light with upconversion quantum yield of 0.1%[32]. There are also recent reports on using a hybrid semiconductor nanocrystal-TTA upconversion system that takes advantages of the broad absorption bandwidth of the semiconductor materials[61, 70, 62].

Another paradigm of applying upconversion process to solar cell that is different from the electrically isolated upconversion system, is to achieve upconversion within the solar cell by redesigning the solar cell structure, similar to the IBSC. Two photon upconversion has been known to occur at the hetero-interfaces between III-V semiconductors and InAs/GaAs QD[103, 79, 50, 25]. Asahi et al. developed a two step photon upconversion solar cell(TPU-SC) with a hetero-interface where upconverted electrons are directly collected by the top electrode in solar cell[8], and observed an large increase in both the photocurrent and photovoltage. Solar cell efficiency exceeding 50% is possible using this TPU-SC structure [7].

In this chapter, I have introduced the main loss mechanisms that limit the solar cell power conversion efficiency and discussed several approaches to surpassing the limit. Upconversion, which converts two low energy photons to one high energy photon, is very promising in improving the solar cell efficiency. I will have in-depth discussion on both the theoretical and experimental work on a novel upconversion nanostrucutre using semiconductor material in this dissertation.

Chapter 2

KINETIC RATE EQUATION MODEL FOR A NOVEL UPCONVERSION NANOSTRUCTURE

With the aforementioned advantages over the molecular upconversion system, semiconductor based upconversion system has a great potential in the PV application. Figure 2.1 plots the potential improvement on the solar cell efficiency for the currently most-studied upconversion materials Lanthanides-doped nanocrystals and TTA systems based on the reported experimental upconversion efficiencies[85, 77]. Although the efficiency could be further increased for these materials, the potential impact is limited by the energy that these systems work in (around 1.3 eV for Ln-based, and around 2 eV for TTA based materials), which do not fall in the range where most solar photons reside. Ideally, the upconversion system should around 1.2-1.5 eV, where the Shockley-Queisser efficiency limit peaks. This is achievable with semiconductor upconversion system. A novel solid state nanostructure that implements upconversion for high efficiency photovoltaics was introduced by Sellers et al.[92]. In this chapter, I will discuss the details of the nanostructure, and the kinetic rate equation model that was developed to predict the theoretical performance of the upconversion nanostrucutre and its impact on the solar cell efficiency. This chapter is organized into three parts: section 2.1 introduces the proposed upconversion nanostructure, section 2.2 provides detailed description on the kinetic rate equation model and section 2.3 discuss the theoretical performance from the kinetic rate equation model calculation. The work presented in this chapter was performed in collaboration with Dr. Eric Y. Chen, Dr.Diane Sellers and Dr. Matthew Doty, and published in reference [21, 93, 92].

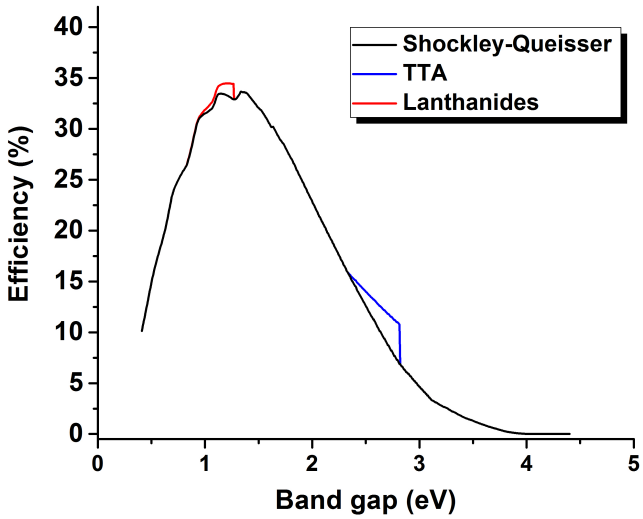

Figure 2.1: Calculated improved solar cell efficiency from addition of Ln-doped nanocrystals and TTA upconversion systems, compared to Shockley-Queisser limit for a single junction solar cell.

2.1 A Novel Solid-state Upconversion Nanostructure

The proposed solid-state upconversion nanostructure (shown in figure 2.2) consists of an epitaxially-grown heterostructure composed of an InAs quantum dot embedded in $In_yAl_{1-y}Bi_xAs_{1-x}$ (InAlBiAs) compositionally-graded barrier. The InAlBiAs graded funnel region is used to guide carriers to the recombination zone, via built-in quasi-electric field as a result of the energy difference between the left and right side of the funnel. Both low energy photons are absorbed within the InAs QD via two step two photon absorption. The active region is confined in InAlGaAs barrier. The new paradigm for photon upconversion engineering semiconductor nanostructures to make a small sacrifice of energy after each photon absorption step (the "photon ratchet"). This controlled energy sacrifice dramatically improves upconversion efficiency and minimizes the loss of energy to heat. To describe the processes taking place within the structure, we denotes the states that carriers could resides in with number 1 to 5. State 1 is the valence band edge of the InAs QD. State 2 is the lowest confined state of the

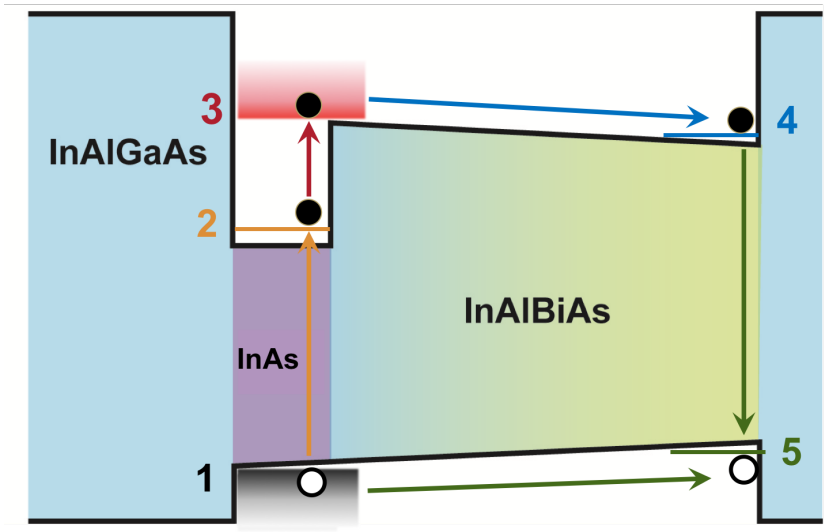

Figure 2.2: Schematic of the proposed novel upconversion nanostructure and available states. Pathways that carriers go through in the upconversion process are indicated by the colored arrows. The continuum band energy states are indicated by the red and black graded regions. The solid black dot represents electrons and the empty dot represents holes.

InAs QD conduction band. State 3 is the minimum energy of the continuum density of states above the InAlBiAs conduction band edge in the vicinity of the QD (i.e. it is the lowest energy state from which electrons have no energy barrier to escape to state 4). State 4 describes the conduction band states in the recombination zone. Electrons added to state 4 originate in the adjacent states 3 and 5. State 5 describes the valence band states in the recombination zone.

The first photon absorption step promotes the electron to the first excited state of the InAs QD (1→2) via an interband transition. The hole rapidly escapes to the right side of the graded InAlBiAs barrier due to the built-in electric field in the valence band of the InAlBiAs and the zero valence band offset between the InAlBiAs left barrier and the InAs QD (1→5). This spatial separation of the electron and hole suppresses the recombination loss pathway after the first photon absorption. The second low energy photon excites the electron to the bulk conduction band state (2→3) via an intraband transition. States 1 and 3 have a continuous density of states in the valence and

conduction bands, respectively. As a result, the optical absorption in both transitions is broadband, as the absorption of a direct gap semiconductor for photons with energy larger than the band gap. Electron relaxation within the QD is suppressed by phonon bottleneck effect, which occurs in low dimensional QDs where the mismatch between the discrete energy levels and phonon frequencies leads to a long carrier relaxation time[101, 108]. The slow relaxation allows a relatively high probability that electrons escape out of the QD to the right side of the InAlBiAs barrier. The electron can then recombine with the hole, emitting a high energy photon. The carrier escape to the recombination zone is driven by the potential energy sacrifice in the graded InAlBiAs region, which results in a photon energy sacrifice (PES, the amount of energy sacrifice is denoted as ΔE_{PES}). Note that ΔE_{PES} is the sum of two energy sacrifices, one in the valence band (ΔE_{VB}) of the InAlBiAs layer and the other in the conduction band (ΔE_{CB}).

$$\Delta E_{\mathrm{PES}} = \Delta E_{\mathrm{CB}} + \Delta E_{\mathrm{VB}} \tag{2.1}$$

The design for the upconverter backed solar cell would have 50 or more upconverter layers to fully absorb low energy photons in the sunlight (figure 2.3). No current is harvested from the upconversion nanostructure. This new paradigm for photon upconversion could be implemented with both epitaxially-grown Quantum Dots (QDs) embedded in semiconductor heterostructures and solution-processed colloidal core/multi-shell QDs, such as CdSe(Te)/CdSSe/CdSe system. Here I modeled an epitaxial system with the structure of InAs QD and InAlBiAs funnel barrier.

2.2 Kinetic Rate Equation Model

In the detailed balance calculation developed by Trupke et al.[107], the upconverter is modeled as two solar cells in series driving one large bandgap LED. This is an idealized model that provides a good framework for estimating the maximum solar energy harvesting that could be obtained via upconversion. However, practical realization of improved solar energy harvesting via upconversion depends on many details of the upconversion process. We develop a kinetic rate equation model that allows us to

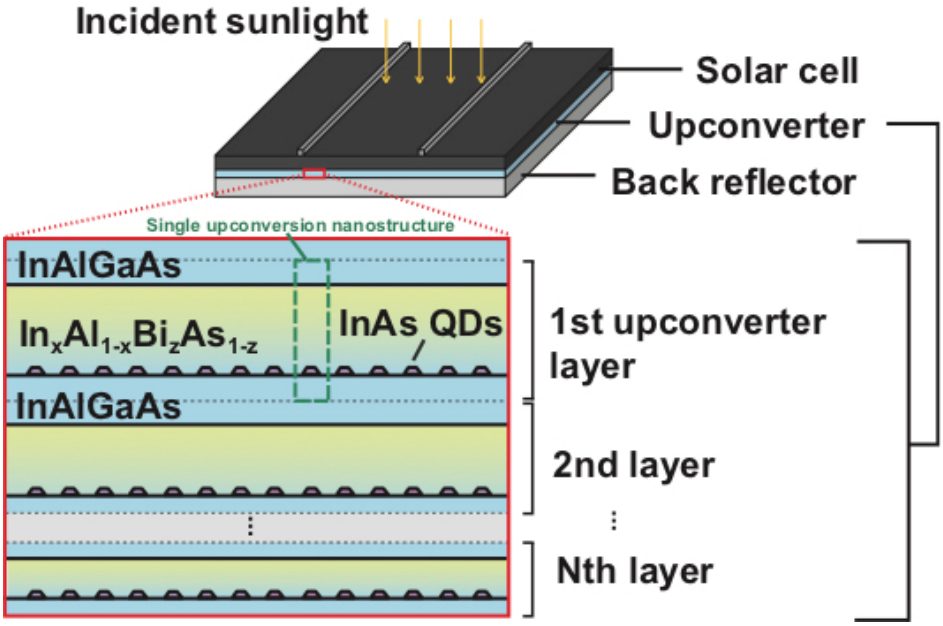

Figure 2.3: Schematic of upconverter-backed solar cell. The upconverster layer consist of multiply layers of the proposed nanostructure[21].

evaluate the performance of the proposed upconversion nanostructure using the known material parameters which provides an approach to optimize the structure by varying details including PES and spectrum splitting. In the following sections, I will discuss the methods used to compute and optimize net solar energy harvesting for a host solar cell backed by this upconversion material in detail.

The kinetic rate equation model computes the change of carrier concentration with time at each of the 5 possible states depicted in figure 2.4 as a function of the rates of the possible transitions associated with the carriers in the respective materials. The rate constant from state i to state j (i,j = 1 to 5) is denoted in k_{ij}.

The figure of merit that quantifies the upconversion material performance used here is the **internal upconversion quantum efficiency (iUQE)**, which is defined as the number of high energy photons upconverted per pairs of low energy photons absorbed. The maximum iUQE is 100% under this definition. Note that some literature use internal upconversion quantum yield that is defined as the number of high energy photons upconverted per number of low energy photons absorbed, which results in an

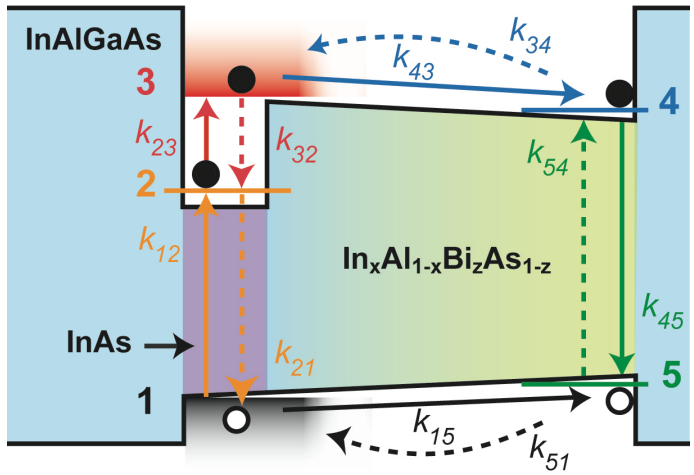

Figure 2.4: Schematic of the band diagram of a single upconverter nanostructure, with competing pathways indicated by the colored arrows. [21]

upper limit of 50%.

2.2.1 Solar Spectrum Splitting Between the Two Photon Absorption Processes

The two photon absorption processes in InAs QD target different bands of the solar spectrum, which will maximize the use of solar spectrum (figure 2.5 left). This is similar to the spectral utilization in multi-junction devices except that current-matching between the solar cell and upconversion layers is not necessary. We define several parameters related to the processes: E_3 is the energy of the emitted upconverted photon, E_1 is the minimum photon energy required for transition 1→2, E_2 is the minimum photon energy required for transition 2→3, and E_g is the host cell band gap (see figure 2.5). The model finds the optimal spectral bands for the low-energy photon absorption according to the following constraints:

$$E_3 = E_1 + E_2 - \Delta E_{\mathrm{PES}} \tag{2.2}$$

$$E_3 \geq E_g > E_1 > E_2 \tag{2.3}$$

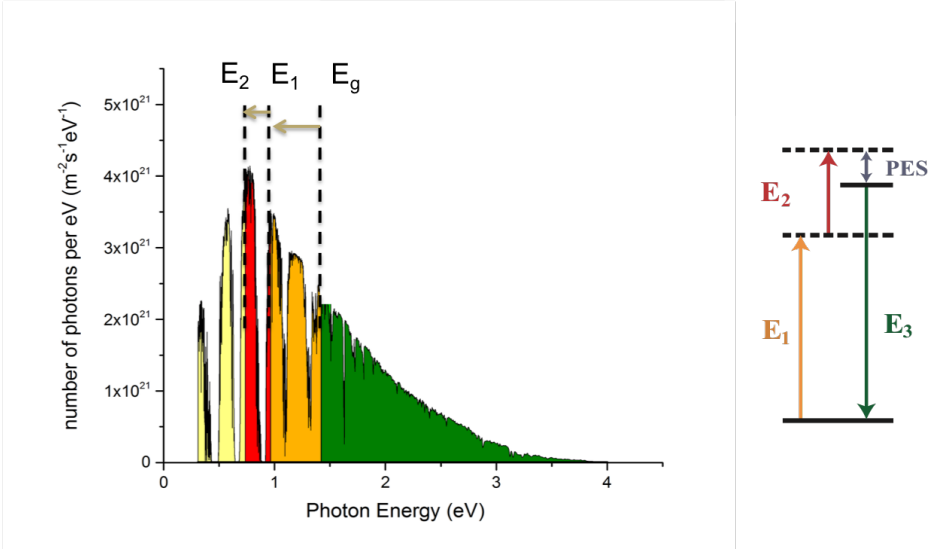

Figure 2.5: Solar spectrum with energy levels in the upcnoversion system labeled.[93]

Equation 2.2 states that the difference between the upconverted photon energy and the sum of the incoming low energy photon energies is equal to the total PES of the system. Equation 2.3 requires that the upconverted photon energy is greater than the energy of the host cell band gap. Photon selectivity, which constrains photons with energy in the range from E_1 to E_g only excite carriers via process 1→2 and photons with energy between E_2 to E_1 only excite carriers via process 2→3, is also assumed. This assumption is commonly applied in other theoretical calculations, as in the work by Trupke et al.[107]. Because two low-energy photons are required to produce one high-energy photon, the initial approach taken is to match the two photon absorption rate to achieve high iUQE, at the operating PES and absorption cross sections of our characteristic nanostructure. AM-1.5 spectrum is used to calculate the photon flux. The optimal energies for the E_1 and E_2 transitions are computed for every host cell band gap in order to achieve photon fluxes that result in approximately equal absorption rates (k_{ij}) for both transitions. k_{ij} is calculated by multiplying the total flux of solar photons within the absorption bandwidth of each transition ($N^{ij}_{photons}$) by the absorption cross section of that transition (α_{12} is the InAs QD interband absorption

cross section, α_{23} is the InAs QD intraband absorption cross section, both taken from literature reported values as summarized in table 3.1) as follows:

$$
\begin{aligned}
k_{12} &= \sum_{E_1}^{E_2} N_{photons}^{12} \times \alpha_{12} \\
k_{23} &= \sum_{E_2}^{E_3} N_{photons}^{23} \times \alpha_{23}
\end{aligned}
\tag{2.4}
$$

The results of this calculation are shown in figure.2.6. The photon absorption rate will depend on the AB, which varies as a function of the selected host cell band gap and the PES introduced into the system. As an example, the calculation below is performed for a GaAs solar cell backed by a 280 meV PES upconverter.The calculation using equation 2.4 yields a k_{12} and k_{23} on the order of 10^3 photons per second. We note that result is only valid for some spectral range as the achievable band gaps of the constituent materials is limited. Although some energy range is not feasible with the proposed material, the purpose of applying the model to the full spectral range is to examine how different host cell band gap response to the addition of an "ideal" upconversion layer.

The minimum photon energy that can drive process 1→2, for example, is the energy difference between the confined state in the QD and edge of the valence band. A photon with slightly higher energy could be absorbed by promoting an electron from deeper within the valence band. This optical absorption would result in an excited hole that rapidly relaxes to the valence band edge (state 1). The rate of this intraband relaxation is a few hundreds of femtoseconds, faster than all other processes in our model, and is therefore neglected in our models. The potential energy gradient implemented in the InAlBiAs zone allows us to control the carrier drift velocity and thus the rates at which electrons and holes are extracted from the QD region and transferred to the recombination zone.

2.2.2 Upconversion Kinetic Rate Equations

In the kinetic rate equation model, a system of rate equations that describes the carrier dynamics is solved. The equilibrium populations of the five states designated

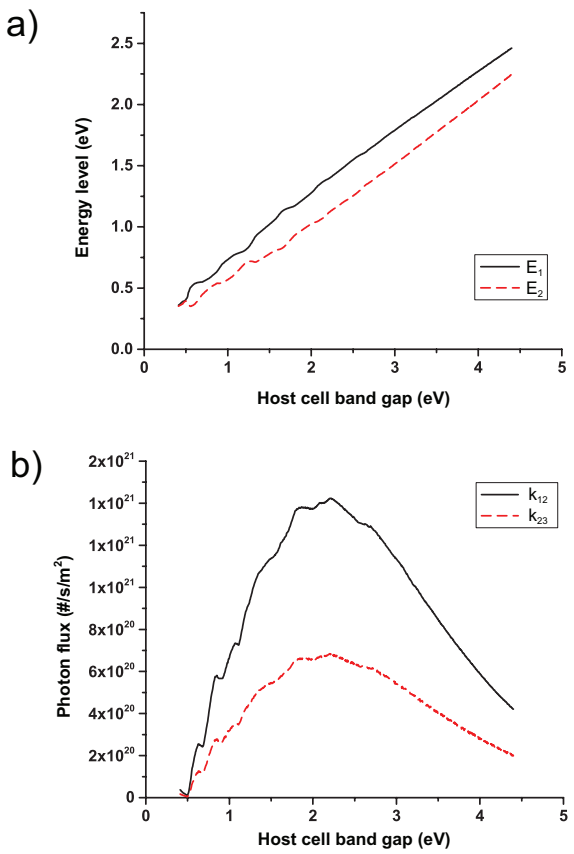

Figure 2.6: Band gaps E_1 and E_2 (a) and corresponding photon fluxes (b), plotted as a function of the host cell band gap E_g. Spectral selectivity is assumed, as is a PES of 280 meV.

in figure 2.2 are computed. Each equation describes the physical processes by which the carrier population of that state changes, including photon absorption, radiative recombination, carrier escape and non-radiative loss. Literature values for similar material systems for the radiative and non-radiative relaxation rates are used. All the rate constant values are compiled in table 2.1. And literature values used are complied in table 3.1. The population n in state i (or j) is given as a function of time t. n is not the conventional carrier density, but represents the state occupation of i. The subscripts h and e represent the hole and electron. n_c is the maximum number of states available in state 2. The equations that will be discussed in detail are:

$$\begin{aligned}\frac{\partial n_{1h}(t)}{\partial t} &= k_{12} \cdot \left(1 - \frac{n_{2,e}t}{n_c}\right) + k_{51} \cdot [n_{5,h}(t) \\ &- n_{1,h}(t)] - k_{21} \cdot n_{2,e}(t) \cdot n_{1,h}(t) \\ &+ k_{15} \cdot n_{1,h}(t)\end{aligned} \tag{2.5}$$

$$\begin{aligned}\frac{\partial n_{2,\mathrm{e}}(t)}{\partial t} &= [k_{12} + k_{32} \cdot n_{3,\mathrm{e}}]\left(1 - \frac{n_{2,\mathrm{e}}(t)}{n_{\mathrm{c}}}\right) - k_{23} \cdot n_{2,\mathrm{e}}(t) \\ &- k_{21} \cdot n_{2,\mathrm{e}}(t) \cdot n_{1,\mathrm{h}}(t)\end{aligned} \tag{2.6}$$

$$\begin{aligned}\frac{\partial n_{3,\mathrm{e}}(t)}{\partial t} &= k_{23} \cdot n_{2,\mathrm{e}}(t) + k_{43} \cdot [n_{4,\mathrm{e}}(t) - n_{3,\mathrm{e}}(t)] \\ &- k_{32} \cdot n_{3,\mathrm{e}}(t)\left(1 - \frac{n_{2,\mathrm{e}}(t)}{n_{\mathrm{c}}}\right) - k_{34} \cdot n_{3,\mathrm{e}}(t)\end{aligned} \tag{2.7}$$

$$\begin{aligned}\frac{\partial n_{4,\mathrm{e}}(t)}{\partial t} &= k_{34} \cdot n_{3,\mathrm{e}} + k_{54} - k_{43} \cdot [(n_{4,\mathrm{e}}(t) - n_{3,\mathrm{e}}(t)] \\ &- k_{45} \cdot n_{4,\mathrm{e}}(t) \cdot n_{5,\mathrm{h}}(t)\end{aligned} \tag{2.8}$$

$$\begin{aligned}\frac{\partial n_{5,\mathrm{h}}(t)}{\partial t} &= k_{15} \cdot n_{1,\mathrm{h}}(t) + k_{54} - k_{51} \cdot [n_{5,\mathrm{h}}(t) - n_{1,\mathrm{h}}(t)] \\ &- k_{45} \cdot n_{4,\mathrm{e}}(t) \cdot n_{5,\mathrm{h}}(t)\end{aligned} \tag{2.9}$$

2.2.2.1 Holes in State 1 - Equation 2.5

The rate at which holes in state 1 change with time depends on the equilibrium populations and rates of carriers transferring between adjacent states 1 and 2 (for electrons) and states 1 and 5 (for holes). The sign correspond to carrier generation or leaving the state.

Holes are generated by photon absorption with rate constant of k_{12} that is dependent on the AB and host cell band gap, and is on the order of 10^3 per second. In addition, the rate is limited by the maximum charge occupancy of state 2, n_{c}, which corresponds to the maximum number of electrons that can be contained in the InAs QD. In our model we take n_{c} to be 6 (2 electrons in each of the s, p_{x}, and p_{y} states).

Holes leave state 1 to state 5 via the built-in electric field, and is described as a drift process. The drift rate of holes from state 1 to state 5, k_{15}, is related to the electric field ϵ_{VB} from the potential difference between the initial and final state of the hole (equation 2.10). It is calculated using the mobility of holes (μ_h) in GaBiAs [53] and is directly proportional to the ΔE_{VB} (equation 2.11).

$$\epsilon_{\mathrm{VB}} = \frac{\Delta E_{\mathrm{VB}}}{l} \tag{2.10}$$

$$k_{15} = \mu_{\mathrm{h}} \frac{\epsilon_{\mathrm{VB}}}{l} \tag{2.11}$$

State 1 population increases when holes diffuse from state 5 to state 1. The diffusion of holes is described by a rate constant k_{51} and is proportional to the population difference between states 5 and 1 and the exponential of the ΔE_{VB}. The full expression for the diffusion process is shown in equation 2.13 based on Fick's Second Law, where the diffusivity D_{h} is obtained Einstein's relation (equation 2.12), and calculated using the mobility of holes μ_{h} in GaBiAs [53]. The full length of the InAlBiAs barrier is 100 nm. We assume that a hole at least $l_{\mathrm{eff}} = 20$ nm away from the QD is sufficiently far away to suppress k_{21} and can be considered to effectively be in state 5. The diffusion

process, which drives carriers up a potential energy gradient, is also dependent on the exponential term that considers the thermal contribution.

$$D_{\mathrm{h}} = \mu_{\mathrm{h}} \cdot k_{\mathrm{B}} \cdot T \tag{2.12}$$

$$\frac{\partial n_{5,h}(t)}{\partial t} = \frac{D_{\mathrm{h}}}{l - l_{\mathrm{eff}}} \left[\frac{n_{5,\mathrm{h}}(t) - n_{1,\mathrm{h}}(t)}{l - l_{\mathrm{eff}}} \right] \exp\left(-\frac{\Delta E_{\mathrm{VB}}}{kT} \right) \tag{2.13}$$

$$k_{51} = \frac{D_{\mathrm{h}}}{(l - l_{\mathrm{eff}})^2} \exp\left(-\frac{\Delta E_{\mathrm{VB}}}{kT} \right) \tag{2.14}$$

k_{21} describes the radiative recombination of an electron from state 2 with a hole from state 1, which decrease the hole population in state 1, and is equal to $1/\tau_{21}$ with τ_{21} being the radiative lifetime. We estimate the rate for our nanostructure to be two orders of magnitude slower than the rate for InAs quantum dots in a GaAs matrix [65, 94]. This estimate is supported by measurements of the radiative lifetime in type-II InAs/GaAs$_{1-x}$Sb$_x$ QDs being longer than the InAs/GaAs system[20, 75]. These lifetimes are attributed to the reduced overlap of the electron and hole wave functions, which may be a conservative estimate due to the zero valence band offset that allows for a broader spatial extent of the hole wave function in our nanostructure. All the literature values used in the model are listed in table 3.1.

2.2.2.2 Electrons in State 2 - Equation 2.6

The rate at which electrons population changes in state 2 depends on the equilibrium populations and rates of carriers flowing between state 2 its adjacent states 3 (for electrons) and 1 (for holes). The term containing rate constants k_{12} representing the electron-hole generation through photon absorption and the term containing k_{21} representing electron-hole recombination are thoroughly described in the previous part 2.2.2.1.

The term with k_{32} correspond to intraband relaxation within the InAs QD from state 3 to state 2, depending on the intraband relaxation lifetime. The rate constant k_{32} is equal to $1/\tau_{32}$ with τ_{32} being the intraband relaxation lifetime. The rate is weighted

by the occupation of the QD. Electron leaves state 2 via second photon absorption and excited out of the QD ground state. The rate depends on the photon arrival rate and the number of available electrons on state 2. k_{23} is on the order of 10^3 s^{-1} from calculation based on equation 2.4. Note that the absorption of a low-energy photon that drives the transition 2→3 does not depend on the occupancy of state 3 because of the continuous density of states in the conduction band of the InAs.

2.2.2.3 Electrons in State 3 - Equation 2.7

The rate constants k_{32} and k_{34} describe electrons leaving state 3, while k_{43} and k_{23} describe electrons entering state 3. Electron leaves state 3 via drift process and populates state 3 via diffusion process, same mechanism as described for holes in state 1 in subsection 2.2.2.1. The diffusion and drift rate of electrons is of the same form as equation 2.13 and 2.11, except for that the subscript is substituted from "h" into "e"and that the processes depend on the energy sacrifice in the conduction band. Literature value of the mobility of electrons μ_e in GaBiAs is used.

2.2.2.4 Electrons in State 4 - Equation 2.8

Population of electrons in state 4 increase from electrons escaping state 3 via drift process, and decrease from electrons diffusing back to state 3 and radiative recombination with holes in state 5 resulting in emission of high energy photons. The drift and diffusion process takes the same form as in equation describing electrons in state 3.

The recombination rate depends on the electron and hole population in state 4 and 5, and on the electron lifetime τ_{45} which is reflected in rate constant k_{45}. This lifetime is approximated as the radiative lifetime of carriers in a GaAs QW [48, 43]. Because our model considers only a single upconversion nanostructure, we assume that reabsorption of photons emitting from the same structure is negligible, i.e., k_{54}, the generation of excitons in the QW by optical absorption, is zero.

2.2.2.5 Holes in State 5 - Equation 2.9

Population of holes in state 5 increase from holes escaping state 1 via drift process, and decrease from electrons diffusing back to state 1 and radiative recombination with electrons in state 4. The drift and diffusion processes are described in subsection 2.2.2.1. The radiative recombination is described in subsection 2.2.2.4

2.2.3 Solving for Internal Upconversion Quantum Efficiency

We assume all states are empty at $t = 0$ and numerically solve the rate equations to find the steady-state solution, which returns the steady-state carrier population in all the five states. The internal upconversion quantum efficiency (iUQE) of a single upconversion nanostructure is calculated as:

$$iUQE = 100\% \times \frac{2 \cdot k_{45} \cdot n_{4,\mathrm{e}} \cdot n_{5,\mathrm{h}}}{k_{12}\left(1 - \frac{n_{2,\mathrm{e}}}{n_c}\right) + k_{23} \cdot n_{2,\mathrm{e}}} \tag{2.15}$$

The numerator accounts for the rate of high energy photon emission from state 4 to 5 electron-hole recombination. The denominator accounts for the inter- and intra-band photon absorption processes in the InAs QD. Steady-state population from solving the model are used for $n_{i,e/h}$. The factor "2" in the numerator is to correct the upper limit of iUQE to 100% from 50% given that one high energy photon is emitted per pair of low energy photon absorbed at maximum iUQE .

2.2.4 Calculating Solar Cell Efficiency

The results from the kinetic rate equation model for upconversion nanostructure is combined with the detailed balance method for solar cells to obtain the total solar energy conversion efficiency of a single-junction cell backed by an upconverter. The external upconversion quantum efficiency, which is defined as number emitted high energy photons per pairs of low energy photon incident on the upconverter, is assumed to be equal to the iUQE. We modified the current density equation 1.7 used in the

Rate constant	Rate (s^{-1})	Description	Approximations	Ref.
k_{12}	10^3	Incoming photon absorption rate for E1	InAs QD peak ground state absorption cross section (MBE grown sample)	[78]
k_{21}	10^7	Radiative recombination rate for electron in state 2 with a hole in state 1	Interband radiative lifetime of type-II InAs/$GaAs_{1-x}Sb_x$ QDs at <77K	[20, 75]
k_{23}	10^3	Incoming photon absorption rate for E2	InAs QD intraband absorption cross section (epi-grown sample)	[89]
k_{32}	10^{11}	Relaxation of carriers in continuum band into ground or first excited state of QD, depending on filling	$In_xGa_{1-x}As$/GaAs self-assembled quantum dots	[83]
k_{34}	$\frac{10^{13}}{\text{eV}} \cdot \Delta E_{\text{CB}}$	Relaxation rate of electron in state 3 to recombination zone, state 4	Using mobility of electrons in GaBiAs The rates are limited to be no faster than 10^{12} (see ref. [106])	[53]
k_{43}	10^{11}	Diffusion of electrons from recombination zone to QD	Using Einstein approximation for Diffusion and mobility of electrons in GaBiAs	[53]
k_{15}	$\frac{10^{12}}{\text{eV}} \cdot \Delta E_{\text{VB}}$	Relaxation rate of hole in state 1 to recombination zone at state 5	Using mobility of holes in GaBiAs The rates are limited to be no faster than 10^{12} (see ref. [106])	[53]
k_{51}	10^{10}	Diffusion of holes from recombination zone to QD	Using Einstein approximation for Diffusion and mobility of holes in GaBiAs	[53]
k_{45}	10^8	Radiative recombination rate for an electron in state 4 and hole in state 5	Radiative lifetime of carriers in GaAs quantum well	[48, 43]
k_{54}	0	Absorption rate of a photon with energy equal to or higher than E3	We model a single nanostructure, assuming no photon reabsorption	–

Table 2.1: Values, descriptions, assumptions, and references for rate constants used in the kinetic rate model. All values are order of magnitude estimates. Note: ΔE_{CB} and ΔE_{VB} are in eV.[21]

detailed balance method to include the extra photons contributed by the upconversion layer:

$$J_T = eN_{photons} - J_0 \cdot exp(\frac{eV}{k_B \cdot T_{cell}}) \tag{2.16}$$

$$N_{photons} = N_{hostcell} + N_{upconverted} \tag{2.17}$$

where J_T is the total current density, $N_{photons}$ is the photon flux incident on the host solar cell, which consists of both the incident solar photons with energy above the host cell band gap and the high-energy photons emitted by the upconverter. $N_{hostcell}$ is the flux of incident solar photons with energy above the host cell band gap under one-sun conditions and $N_{upconverted}$ is the flux of upconverted high-energy photons returned to the host cell from the upconverter. We can determine the $N_{upconverted}$ by computing the flux of photons incident on both upconversion transitions from the solar spectrum (E_1 to E_g and E_2 to E_1), choosing the smaller of the two (e.g. red line in figure 2.6 (b)), and multiplying this number by the iUQE, assuming that there is sufficient number of layers of upconversion nanostructure to absorb all the solar photons.

2.3 Theoretical Performance of the Upconversion Nanostructure and Upconverter-backed Solar Cell

This section, we will discuss the results from the kinetic rate equation model. The iUQE and solar conversion efficiency are calculated for a wide PES range, and for host cell band gap ranging form 0.4 to 4.5 eV (corresponding to the energy range of the photons in the solar spectrum). Again, although some energy is not feasible with the proposed material, we applied the model to the full spectral range to examine how different host cell band gap response to the addition of an upconversion layer designed for that specific energy range. The result will serves as a guideline for future upconversion material development by pointing out the importance of some structural parameters on upconversion performance. In addition, the kinetic rate equation model can be generalized to any material platform that implements upconversion in a similar fashion.

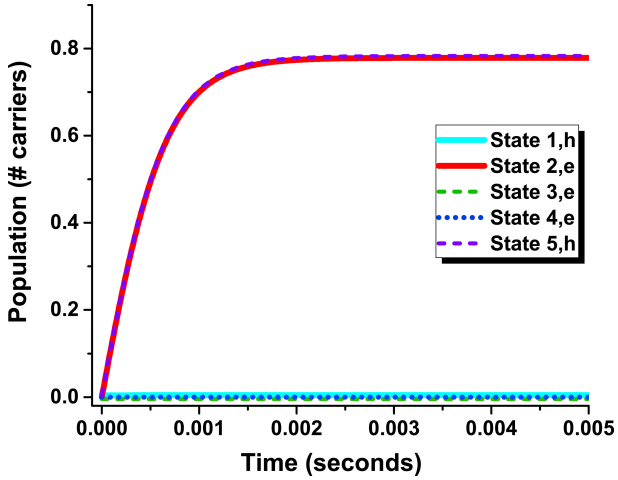

Figure 2.7: Equilibrium populations for increasing time (offset for clarity). At equilibrium the populations in states 2 and 5 reach ≈ 0.8 carriers per state while the other states have no carriers. Assuming GaAs host cell.[21]

2.3.1 Steady-State Population

At steady state, the populations in states 2 and 5 reach ≈ 0.8 carriers per structure while the other states have no carriers, as shown in figure 2.7. Since less than 1 carrier occupies each state at equilibrium, we therefore do not consider changes to the quasi-Fermi levels (QFLs) or band bending when using these rate equations to compute the performance of a single nanostructure.

2.3.2 Upconversion Nanostructure Performance and Impact on Solar Cell Efficiency

Figure 2.8 plots the iUQE of the proposed upconversion nanostructure layer as a function of both the band gap of the host cell and the PES value. iUQE strongly depends on the PES value. More than 200 meV of PES is required in the nanostructure to yield significant iUQE. An increase in the PES increases the rate of carrier drift into states 4 and 5 and decreases the rate of carrier drift out of these two states. In other words, adequate PES is required to increase the rate of carriers escaping to the state 4 and 5 for raidative recombination to compete with the loss pathways. As a result, iUQE is strongly dependent on PES. A PES of approximately 400 meV is necessary to

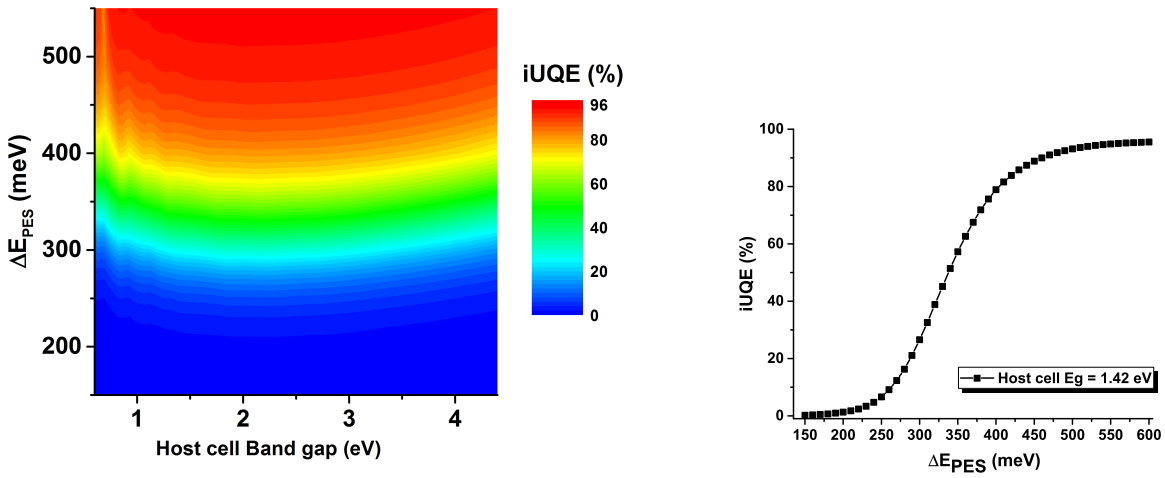

Figure 2.8: Left: iUQE for solar cell band gaps ranging from 0.4 to 4.75 eV with varying values of PES. Right: Assuming GaAs host cell($E_g = 1.42eV$), iUQE as a function of the PES[21].

reach high iUQE, but additional PES beyond this point does not significantly improve iUQE. The maximum iUQE is around 96%.

Net solar energy conversion efficiencies exceeding 39% could be realized with PES values larger than 400 meV by using host solar cells with band gaps between 1.3 and 1.75 eV (figure 2.9 (top)). Note that GaAs, with a band gap of 1.42 eV, lies within the window of host cell band gaps for which overall high efficiency improvements can be achieved. Figure 2.9 (right) shows the net solar conversion efficiency for several common solar cell materials. The wide band gap solar cells (e.g. GaAs, CdTe, CGS) yield the highest net solar conversion efficiency at moderate PES, and have the largest net improvement of efficiency from addition of the upconversion layer. Enhancement on the solar cell efficiency starts to drop when PES exceeds 550 meV, as a result of the trade-off between UQE and PES: higher UQE increases the number of high-energy photons emitted for a given number of incident low-energy photons, but increasing PES reduces the number of low-energy solar photons that can be harvested by the upconversion material. Taking PES value into consideration,

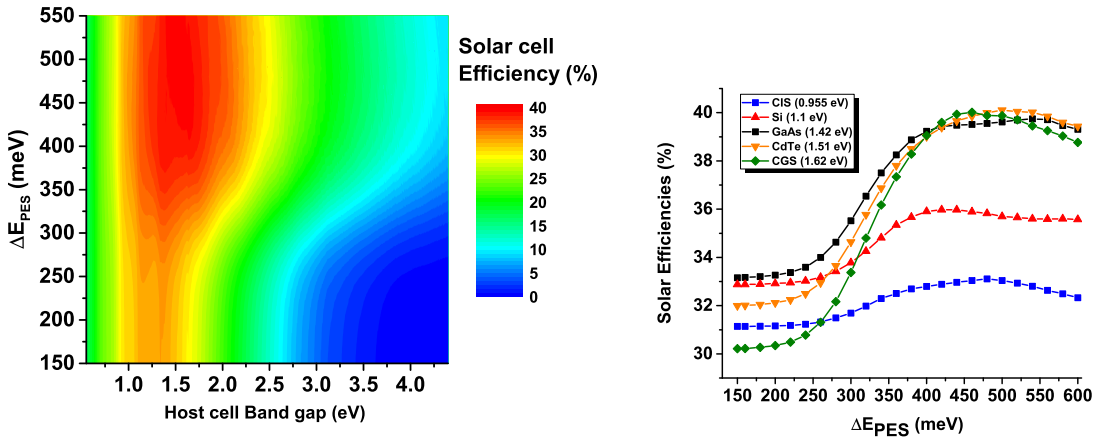

Figure 2.9: Left: Solar conversion efficiency of the upconverter-backed solar cell in color scale as a function host cell band gap and PES[93]. Right: Potential improvement on the solar conversion efficiency of the upconverter-backed solar cell for some typical solar cell materials as a function of PES[21].

2.4 Summary

I have described in detail the proposed solid state upconversion nanostructure and the kinetic rate equation model developed to predict the theoretical performance of the upconversion nanostructure with material paramters integrated. Theoretical analysis shows that the structure is very promising in improving the single-junction solar cell efficiency via broad band upconversion. The maximum upconversion quantum efficiency achievable with this naostructure is around 96%, and the solar energy conversion efficiency for a single-junction solar cell integrated with the upconversion layer could reach over 39% under 1-sun condition. From the kinetic rate equation model, we have learned that PES plays an important role in the upconversion efficiency. It is necessary to introduce adequate amount of PES in the upconversion system in order to achieve high iUQE. Sensitivity analysis performed on parameters spectrum splitting, photon absorption cross section, carrier relaxation and recombination rate provide guidance in terms of the material properties required to optimize the upconversion

nanostructure. Moreover, the upconversion nanostructure performance improves drastically with concentrated incident light. And the efficiency of a solar cell backed by the modeled upconverter could exceed 60% under concentrated sunlight. Use of concentrated sunlight relaxes constraints on the host solar cell band gap and the amount of PES required for high solar energy conversion efficiency. Analysis indicates that the upconversion nanostructure performance is most sensitive to intraband relaxation τ_{32}, i.e. the greatest change in net solar cell efficiency occurs when this rate is decreased by one order of magnitude. It is important to reduce this loss with material engineering.

Chapter 3

SENSITIVITY ANALYSIS OF THE UPCONVERSION NANOSTRUCTURE

I have introduced the new paradigm for photon upconversion using solid state nanostructures implemented with epitaxially-grown QDs embedded in semiconductor heterostructures and the kinetic rate equation model that shows outstanding theoretical performance in the last chapter. In this chapter I will discuss the sensitivity of the theoretical performance of the upconversion nanostructure to change of parameters like spectrum splitting, QD absorption cross section, incident sunlight concentration values, and electron lifetimes. This analysis provides important insights on how the upconversion nanostructure could be optimized for solar cell application and can focus experimental efforts on achieving the composition and structure most likely to have a significant impact on net solar energy harvesting. The work presented in this chapter was performed in collaboration with Dr. Eric Y. Chen and Dr. Matthew F. Doty.

3.1 Sensitivity Analysis of the Theoretical Performance under Varying Conditions

The upconverter and solar cell performance are determined by many factors. For example, the PES is intentionally introduced to assist the escape of carriers out of the QDs and reduce carrier loss due to fast relaxation rates. However, there is a trade off between improved carrier separation and decreasing energy of the emitted photons as PES is increased. In the previous section 2.3, the effect of PES on the upconverter and solar cell performance is discussed. In this section, we will explore the sensitivity of the models to the following conditions: changing spectrum splitting, smaller absorption cross-sections, changing radiative and nonradiative relaxation rates,

Parameter	Description	Original Value	Range explored
$\tau_{21}(1/k_{21})$	Radiative recombination rate for electron	100 ns [20, 75]	–
μ_e	Electron mobility	1500 $cm^2/(V\cdot s)$ [53]	–
μ_h	Hole mobility	100 $cm^2/(V\cdot s)$ [53]	–
k_{12}/k_{23}	Spectrum splitting	1	0.01 - 10
α_{12}	Interband absorption cross section	$1.1 \times 10^{-14} cm^2$ [78]	down to 1% of original value
α_{23}	Intraband absorption cross section	$2.3 \times 10^{-14} cm^2$ [89]	down to 1% of original value
$\tau_{32}(1/k_{32})$	Intraband relaxation time from state 3 to 2	10 ps [83]	5 ps, 1 ps
$\tau_{45}(1/k_{45})$	Radiative recombination lifetime from state 4 to 5	10 ns [48, 43]	100 ns, 1000 ns

Table 3.1: List of values of parameters used in the model and the range explored in the sensitivity analysis

changing hole mobilities, and incident light intensity. Table 3.1 summarize the original experimental values and the range explored in the sensitivity analysis.

3.1.1 Varying Spectrum Splitting: k_{12}/k_{23}

The initial approach taken was to split the solar spectrum between the two absorption steps that take place within InAs QD such that the photon flux absorbed results in k_{12}, the rate of interband excitation, being equal to k_{23}, the rate of intraband excitation. Since the two photon absorption processes are the rate-limiting steps in the upconversion process, and sequential photon absorption is necessary to generate a high-energy electron-hole pair, unequal k_{12} and k_{23} rates could have a significant effect on the upconverter performance. To evaluate the potential impact of unequal k_{12} and k_{23} rates, iUQE and solar cell efficiency for k_{12}/k_{23} values (based on equation 2.4) between 0.01 to 10 while keeping all other parameters the same are calculated. 1-sun illumination conditions is assumed for these calculations.

Figure 3.1a shows that the internal quantum efficiency of the upconverter decreases with increasing k_{12}/k_{23} ratio, i.e. when more of the solar spectrum is absorbed

in the first transition in the QD. This trend arises due to the order of magnitude difference in lifetimes between transitions state 2→1 and state 3→ 2 (100 ns and 10 ps, respectively). Choosing the splitting to allow for more photon absorption in the state 2→3 transition compensates for the faster relaxation of carriers through the 3→2 transition compared to the 2→1 transition. Thus, iUQE will maximize when the k_{12}/k_{23} is very low.

Although putting more photons in the 2→3 step increases the iUQE, it does not necessarily create the best solar cell efficiency, i.e. the overall best solar cell efficiency does not occur under highest iUQE. As shown in figure 3.1b, the maximum net solar energy conversion efficiency of the host cell backed by the upconverter (46.4%) occurs at a k_{12}/k_{23} ratio around 0.5 for all host cell band gaps. This is exactly the ratio of the absorption cross sections for the inter- and intraband transitions α_{12}/α_{23}. The same result is obtained when the power conversion efficiencies are computed for α_{12}/α_{23} ratios of 0.05 and 5 (by changing the α values when using equation 2.4), as shown in figure 3.1c. This result is related to the assumptions made in this model, namely: 1) perfect spectral selectivity, 2) the external upconversion quantum efficiency of the upconversion layer is assumed to be equal to the iUQE for an individual upconversion nanostructure, 3) the upconversion layer is assumed to be sufficiently thick that all incident photons are absorbed, and 4) the extra photon flux provided by upconversion is calculated based on the $N^{12}_{photons}$and$N^{23}_{photons}$. Under these assumptions, maximum energy conversion is obtained when the flux of photons incident on each transition is the same.

3.1.2 Varying QD Absorption Cross Section

How InAs QD inter- and intra-band absorption coefficients affect the upconverter and solar cell performance are also analyzed. The literature values used for the inter- and intra-band absorption cross section are 1.1 x 10^{-14}cm^2 per QD [78] and 2.3 x 10^{-14}cm^2 per QD [89] respectively. These are values experimentally measured on similar material systems. In the calculation presented in the previous chapter, the

(a)

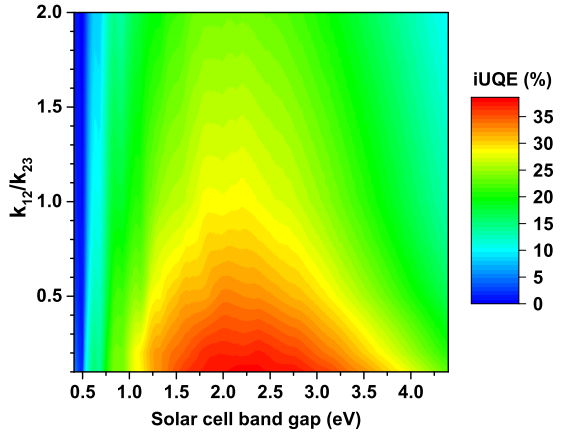

(b)

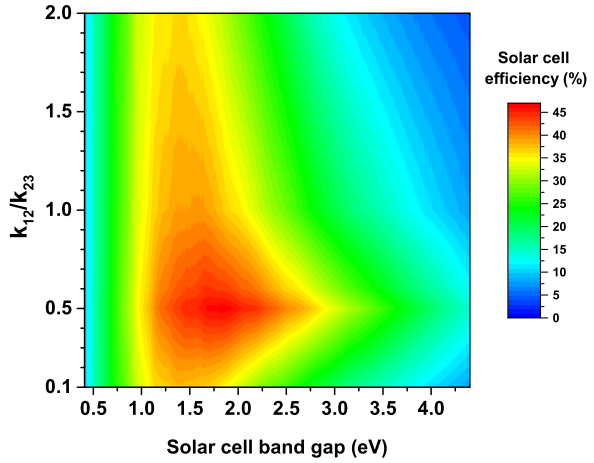

(c)

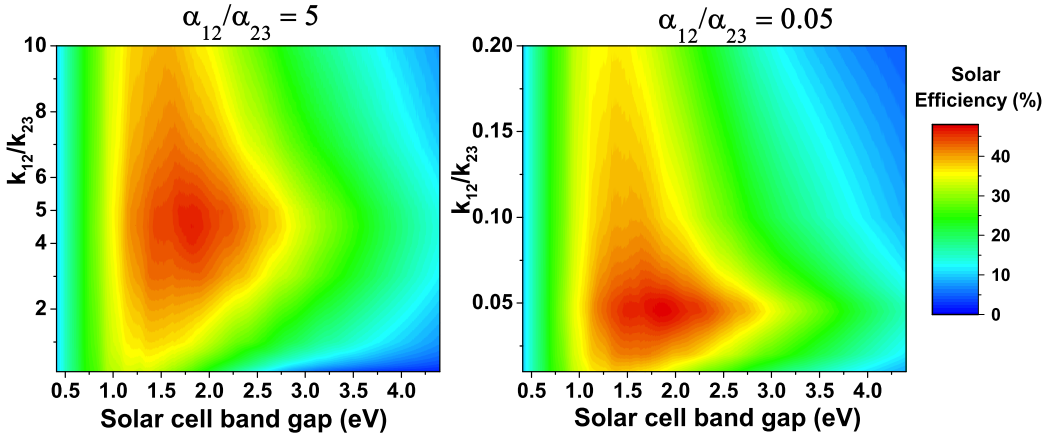

Figure 3.1: a): iUQE as a function of k_{12}/k_{23} and solar cell band gap,assuming PES of 300 meV; b): maximum solar cell efficiency as a function of solar cell band gap and k_{12}/k_{23} ; c): maximum solar cell efficiency as a function of solar cell band gap and k_{12}/k_{23} , assuming different α_{12}/α_{23}.

absorption cross section is approximated to be the same across the whole absorption wavelength range. However, in reality, the cited value is the maximum for a specific wavelength, and the absorption decreases as the wavelength changes. In order to understand how variation in the absorption cross section values could affect the performance of the upconverter, we modeled the theoretical upconverter performance by reducing the k_{12} and k_{23} values, which is equivalent to having a smaller net absorption cross section.

The absorption cross section ratio (AR) is defined as a percentage of the cited absorption cross section, i.e. a number less than 1. For example, an AR of 0.1 refers to an α_{12} and α_{23} that is 10% of the value used in reference [21]. This is equivalent to averaging the absorption cross section across the wavelength range, leading to a more conservative set of assumptions. 1-sun illumination conditions is assumed for these calculations. Relative variations in the absorption cross section, which might arise physically due to polarization or lateral propagation in thin-film upconversion layers, are captured by the k_{12}/k_{23} analysis described above.

Figure 3.2a shows the internal upconversion quantum efficiency as a function of PES, the energy sacrificed to efficiently funnel carriers to the recombination region, and AR, the reduced absorption cross section of the QD inter- and intra-band transitions. These calculations are performed for a fixed optimal k_{12}/k_{23} of 0.5 and, to provide a clear example, the spectral splitting appropriate for an upconverter backing a GaAs host cell. The figure shows that a decrease in AR from 1 to 0.01 (slower photon arrival rate) reduces the iUQE, from ∼80% to ∼20% at a PES of 400 meV. However, the upconverter can still achieve moderate iUQE (>30%) despite low AR as long as the PES is large, e.g. more than 400 meV.

To show how net solar energy harvesting is affected by varying absorption cross section, the highest solar cell efficiency achievable for each host cell band gap, from 0.4 to 4.5 eV, for a range of AR from 1 down to 0.01 is plot in figure 3.2b. In each case the figure is plotted with the PES that maximizes net solar energy harvesting efficiency

within the PES range of 200 meV to 480 meV. Figure 3.2b shows that net solar efficiencies in excess of 40% can be achieved even for AR values as low as 0.01, verifying that upconversion provides a promising route toward high-efficiency solar energy harvesting that is relatively insensitive to changes in the absorption cross section. Note that the kinetic rate equation model assumes that the upconversion material is sufficiently thick to absorb all low-energy photons, so additional cost considerations will come into play in engineering cost-competitive devices. There are a variety of photonic engineering techniques like gratings or waveguides that can be implemented to enhance the light absorption and minimize the amount of material required.

3.1.3 Varying Intraband Relaxation Time

The phonon bottleneck in the conduction band of the QD helps reduce the rate of electron relaxation from the continuous band to the ground state by inhibiting the coupling to phonon modes. In previous section, a conservative 10 ps intraband relaxation time (τ_{32}) based on literature values was assumed. Because no experimental data on the intraband relaxation time is available for the proposed system, the sensitivity of the predicted upconverter performance to this rate should be analyzed. Specifically, as shown in figure 3.3, the iUQE of an upconverter designed for a GaAs host cell, as a function of PES for three different values of τ_{32}: 10ps, 5ps and 1ps, is calculated.

The iUQE and net solar cell efficiency as a function of PES for three values of τ_{32} are plot in figure 3.3 To assess the importance of τ_{32}. Decreasing the τ_{32} by one order of magnitude from 10 ps (blue triangles) to 1 ps (black squares) decreases the iUQE from 90% to 60%, and the solar cell efficiency from 44% to 41% at 475 meV PES (or a 7% relative decrease), as shown in Fig. 3.3 (top). The reduction in iUQE is a result of increased loss from state 3 to state 2. When such loss is present, introducing a slightly larger PES still allows net solar cell efficiency of over 43%, as shown in figure 3.3(bottom). However, further decreasing τ_{32} below 5 ps severely impacts the iUQE and upconverter-backed solar cell efficiency improvement. This sets an important constrain on the τ_{32} that must be achieved for efficient upconverter performance.

(a)

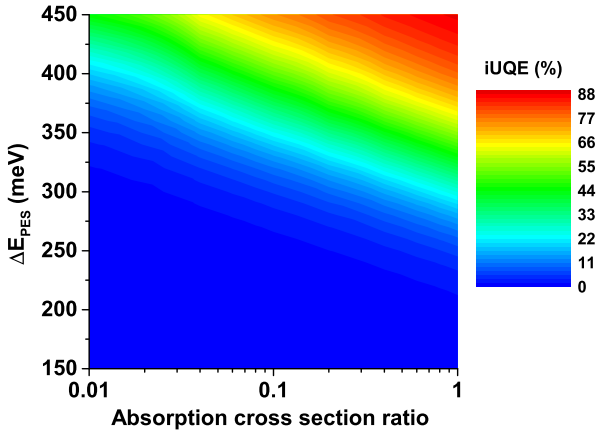

(b)

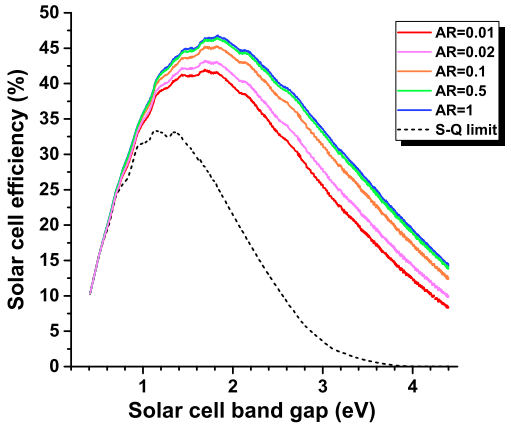

Figure 3.2: a): Upconverter iUQE in color scale as a function of AR and PES. b): Solar cell efficiency as a function of bandgap for varying AR. Solid lines: with upconverter; Dashed: without upconverter.

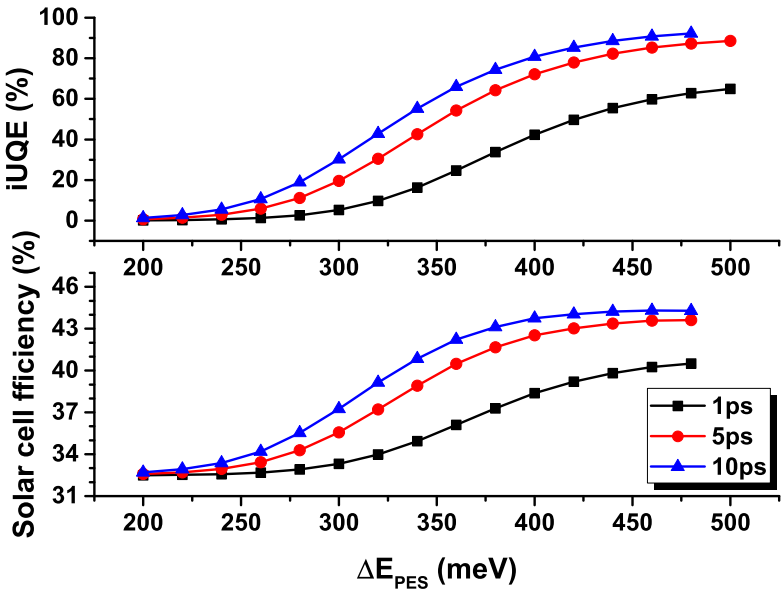

Figure 3.3: Top: iUQE as a function of PES, bottom: solar cell efficiency as a function of PES. Both calculations assume a GaAs host cell and compare the effects of different τ_{32} assumptions.

3.1.4 Varying Radiative Recombination rate

Radiative recombination from state 4 to state 5 emits a high energy photon. The rate of this radiative recombination is a very important parameter. Previous modeling assumed a conservative lifetime of 10 ns based on GaAs QW[48, 43]. Here we evaluate the importance of this rate by calculating the change in the upconverter and upconverter-backed solar cell performance for longer τ_{45} lifetime that represents a less efficient radiative recombination efficiency.

We changed the τ_{45} radiative recombination lifetime from 10 ns to 1000 ns, corresponding to recombination rate constant k_{45} from 10^8 to 10^6 s^{-1}. The results are shown in figure 3.4. When increasing the τ_{45} by one order of magnitude from 10 ns (black squares) to 100 ns (red squares), the iUQE decreases from 95% to 85%, and the net solar cell efficiency decreases from 44% to 43% (or a 2% relative decrease) at 470 meV PES. These results, combined with the previous results, show that the upconverter performance is less sensitive to the τ_{45} than it is to the intraband relaxation, τ_{32}. Only

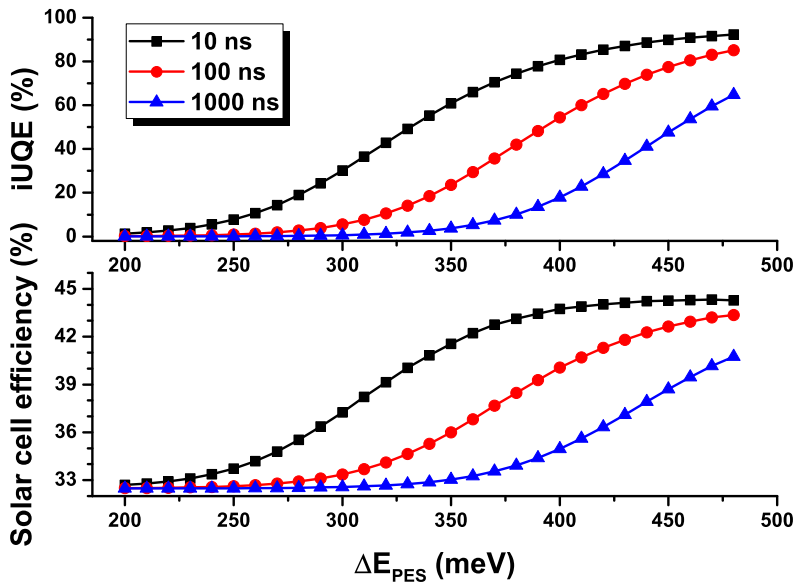

Figure 3.4: Top: iUQE as a function of PES, bottom: solar cell efficiency as a function of PES. Both calculations assume a GaAs host cell and compare the effects of different k_{45} assumptions.

by reducing the radiative recombination efficiency by increasing the τ_{45} by another order of magnitude from 100 ns to 1000 ns would lead to an iUQE and solar cell efficiency change comparable to that of the range of τ_{32} values tested. Although this degradation in performance could be compensated by introducing more PES, the calculations verify that it is important to achieve a high recombination efficiency.

3.1.5 Varying Solar Concentration

Analysis of the potential benefits of concentration for the performance of upconversion systems can inform the trade offs that must be made when designing cost-effective routes toward high efficiency. Changing the illumination incident on the system will affect the photon arrival rate in the inter- and intra-band absorption steps (k_{12} and k_{23}). The rate is proportional to the concentration ratio (CR), which is described in units of "number of suns". Under concentration, both the solar cell and upconverter experience higher incident photon intensity. The concentration ratio has

a theoretical maximum of 46165 [55], which is determined by the sun-earth geometry. We define two terms:

$$k_{12}^{CR} = CR \times k_{12}^{1}$$
$$k_{23}^{CR} = CR \times k_{23}^{1} \tag{3.1}$$

where k_{12}^{1} is the rate of incident photons for the transition from 1 to 2 under normal AM-1.5 one sun conditions in [21], i.e. the superscript indicates a CR of 1. The current in the solar cell from equation 2.16 is modified to be:

$$J_T = e\left[N_{photons}(CR) - J_0 \cdot exp(\frac{eV}{k_B \cdot T})\right] \tag{3.2}$$

$N_{photons}(CR)$ is the photon flux incident on the host solar cell, which consists of both the incident solar photons with energy above the host cell band gap and the high-energy photons emitted by the upconverter. In other words, equation 2.17 becomes:

$$N_{photons}(CR) = CR \cdot N_{hostcell} + N_{upconverted}(CR) \tag{3.3}$$

The solar photon flux that is directly absorbed by the host cell under concentration simply scales with the CR, as has been previously computed for single junction solar cells[46]. The dependence of $N_{upconverted}$ on CR is more complicated: the flux of low energy photons incident on the upconverter increases linearly with CR, but the efficiency of the upconversion process also changes due to the competition between excitation and relaxation rates. Kinetic rate equation model is used to numerically compute $N_{upconverted}(CR)$ for use in equation 3.3 and the subsequent calculation of net solar energy harvesting efficiency. The change in efficiency of the upconverter (iUQE) and the overall improvement in solar cell efficiency are analyzed separately.

The parameters used in the model for the rate of the transitions are experimental values from the same or similar material system from literature from lack of experimental measurements on the proposed upconversion nanostructure (Table 2.1). The

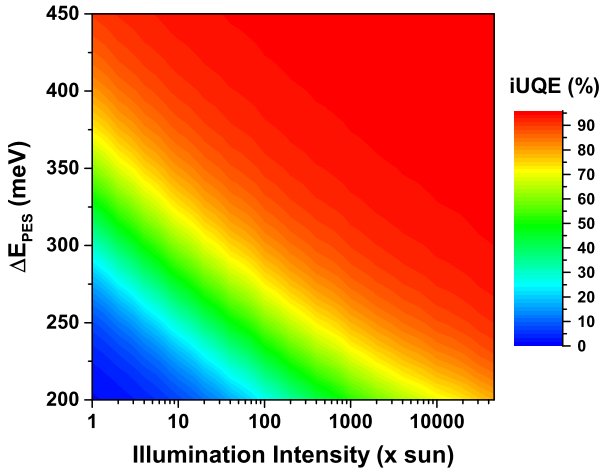

Figure 3.5: iUQE as a function of concentration and PES. An upconverter designed for a GaAs solar cell is assumed.

outcome of the modeling serves as a guideline for the ongoing growth and characterization of the nanostructure. Experimental verification of the resultant nanostructure can then further refine the model parameters.

To assess the impact of concentrated sunlight on the performance of an upconverter, we compute performance with a fixed k_{12}/k_{23} ratio of 0.5 and values for k_{12} and k_{23} increased by the concentration factor. As expected, a faster arrival rate for photons (higher k_{12} and k_{23}) improves iUQE because fewer electrons and holes are lost to recombination pathways that have fixed rates. In figure 3.5 we consider the iUQE of the upconverter as a function of both PES and concentration. iUQE increases with PES for any fixed solar concentration until it reaches the maximum theoretical iUQE of around 96%. However, the threshold PES required to reach the 96% maximum decreases with increasing concentration. This occurs because higher CR reduces the requirement for fast escape of carriers in order to overcome carrier loss processes.

Next, the maximum solar energy conversion of an upconverter-backed solar cell as a function of concentration is computed. Following the approach used in the preceding section, for each concentration considered, the net solar energy conversion

is computed using the PES that leads to best performance. The results are presented in figure 3.6a. For comparison, the performance of solar cells without an upconverter under the same concentration conditions is also plotted. Adding the upconverter leads to significant improvements in net solar energy conversion efficiency as CR increases. For example, with 100 times CR, the calculation reveals a solar cell efficiency as high as 52.4% for a host cell band gap of 1.9 eV, compared to an efficiency of 25.7% for a solar cell without an upconverter under the same concentration conditions. The theoretical maximum solar cell efficiency that can be achieved with an upconverter under concentration is 60.8% for a host cell band gap of 1.59 eV under theoretical maximum CR of 46165. This theoretical maximum is comparable to the maximum achievable with 3-junction devices [46].

Note that the addition of the upconverter broadens the range of host cell band gaps over which high efficiency under concentration is possible. This implies a great deal of flexibility in the choice of host solar cell materials that could be backed by the upconverter. Moreover, even for host cell band gaps as high as ≥ 3 eV, a significant increase in the efficiency of solar cells backed by an upconverter under moderate solar concentration is still achievable.

In figure 3.6b the minimum PES required to achieve the highest possible solar cell efficiency as a function of solar concentration for a GaAs host cell is plotted. The model computes 60% GaAs solar cell efficiency under maximum concentration with a PES of as little as 280 meV. The physical reason for this decrease in the PES necessary for high efficiency is the improved iUQE under concentration as discussed above with respect to figure 3.5. A secondary benefit is that reducing the PES required for high iUQE also increases the range of the solar spectrum that can be harvested by the upconverter, further increasing the overall efficiency of the solar cell-upconverter system.

Lastly, the performance of the upconverter-backed solar cell in terms of the additional short-circuit current, ΔJ_{sc}, is shown. This is the additional current gained

(a)

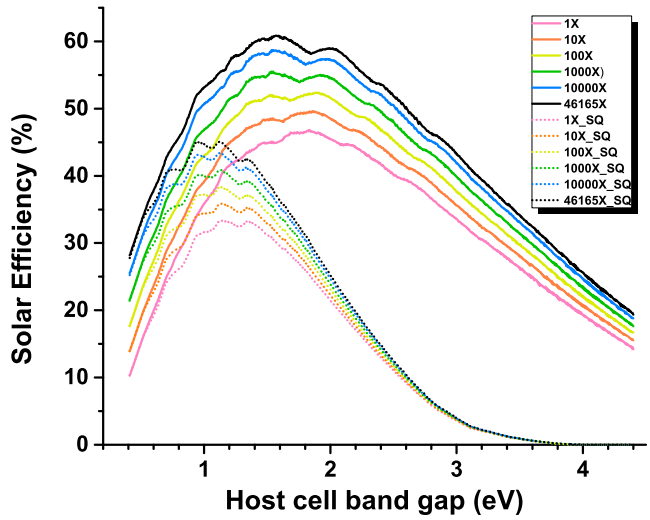

(b)

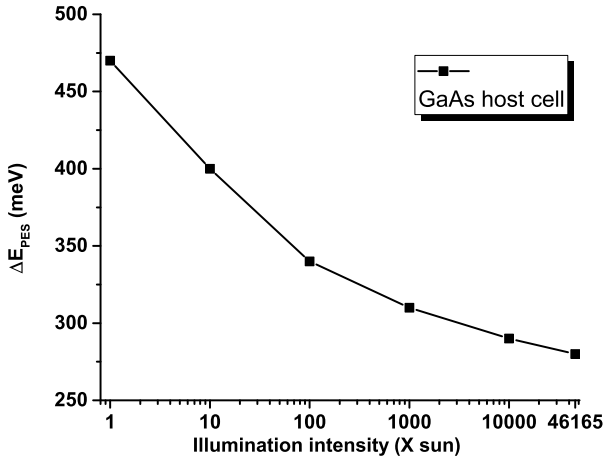

Figure 3.6: a): Highest solar cell efficiency as a function of host cell band gaps. Solid: upconverter-backed solar cell; Dashed: without upconverter. Each colour denotes a selected concentration ratio, marked in the legend. b): PES value that corresponds to the highest calculated solar cell efficiency in panel (a) for a GaAs host cell.

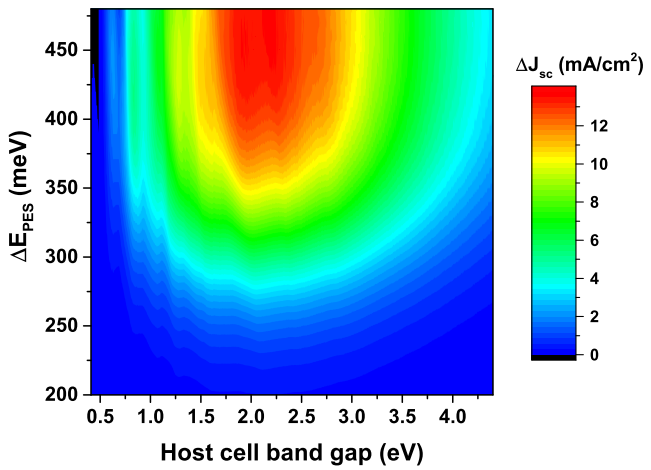

Figure 3.7: Additional short-circuit current in the host solar cell as a function of host cell bandgap and PES, computed for 1 sun excitation conditions.

due to the increased photon flux from upconverted photons, which is a useful figure-of-merit when comparing full photovoltaic devices. The performance of the upconverter under 1-sun excitation as a function of PES and host cell band gap in figure 3.7. We predict nearly 14mA/cm^2 additional ΔJ_{sc}, which approaches the best ΔJ_{sc} realized in an upconverter-backed crystalline Si solar cell, 17mA/cm^2 obtained under 94-sun concentration [41].

3.2 Summary

Sensitivity analysis performed on parameters spectrum splitting, photon absorption cross section, carrier relaxation and recombination rate provide guidance in terms of the material properties required to optimize the upconversion nanostruture. Moreover, the upconversion nanostructure performance improves drastically with concentrated incident light. And the efficiency of a solar cell backed by the modeled upconverter could exceed 60% under concentrated sunlight. Use of concentrated sunlight relaxes constraints on the host solar cell band gap and the amount of PES required for high solar energy conversion efficiency. Analysis indicates that the upconversion

nanostructure performance is most sensitive to intraband relaxation τ_{32}, i.e. the greatest change in net solar cell efficiency occurs when this rate is decreased by one order of magnitude. It is important to reduce this loss with material engineering.

Chapter 4

INTRODUCTION TO GROWTH AND CHARACTERIZATION TECHNIQUES

MBE is a powerful tool to obtain high quality epitaxial layers with very good control of composition and thickness down to monolayer precision, along with the capability of in-situ monitoring during the growth. All of the samples were grown via molecular beam epitaxy (MBE) which I will introduce in section 4.1, focusing on both the MBE machine and mechanisms in MBE growth. Sample characterization techniques are introduced in section 4.2. Specifically, I will introduce high-resolution X-ray diffraction, Rutherford backscattering spectrometry and spectroscopic ellipsometry.

4.1 Molecular Beam Epitaxy

Molecular beam epitaxy was developed during the 1960s and 1970s as a technique to grow high quality single crystal materials. A schematic of the MBE chamber is shown in figure 4.1. There are solid, gas, plasmonic type of MBE classified based on the type of source used. The MBE used here in University of Delaware is OSEMI Nextgen III-V solid source MBE. High purity elemental source materials are placed in the thermal evaporation cells on the bottom part of the chamber (there is also horizontal configuration). The evaporated source materials condense on the substrate, and form crystalline thin film.

4.1.1 MBE Chamber Components

MBE requires ultra high vacuum (UHV). UHV enables MBE to produce high quality materials with very low impurity concentration. Another benefit of the UHV is that the mean free path of the evaporated source materials exceeds the deposition

distance between the source cell and the substrate. This ensures the atoms/molecules travel to the substrate in a beam-like path, without interaction between different source materials before reaching the substrate. To achieve UHV condition, the stainless steel chamber is pumped by various pumps (ion pumps, cryo pump, liquid nitrogen cooled cryo-panel etc.) to background pressure in the range of 10^{-10} or even 10^{-11} torr level. The substrate wafer is attached to the substrate manipulator (or continuous azimuthal rotation, CAR assembly), which is capable of performing both substrate rotation and substrate temperature control during the growth. The beam equivalent pressure (BEP) of the source is measured with a hot cathode ionization gauge attached to the backside of the substrate manipulator. BEP is proportional to the amount of material incorporated. Calibrations of BEP vs growth rate or elemental composition are performed to obtain the correct growth parameters required. Typical growth rate is rather slow, around $1\mu m$/hr. Mechanical shutters above the source cell aperture are used to interrupt the beam. The temperature of the wafer is monitored with band edge thermometry (BET). The band gap of the semiconductor decreases with increasing temperature described by Varshni relation. BET measures the band gap of the wafer by detecting the light transmitted through the wafer from a broad band light source locating behind the wafer, and determines the band gap. Radiation from the substrate heater is also a major source of input light. However, low temperature monitoring with BET is difficult in our MBE system as the radiation from heater is very low. In-situ monitoring of the growth is achieved with the reflection high energy electron diffraction (RHEED) which will be further discussed in the following subsection.

4.1.2 MBE Growth Process

Examining the epitaxy from the thermodynamic consideration of surface energy, there are three main growth modes during epitaxial growth: 1) Frank–van der Merwe (FM) mode, also referring to the layer-by-layer. In the FM mode, growth proceeds in the layer by layer manner, with one layer completes before the second layer growth (see figure 4.2 (b)). The adatoms preferentially bound to the surface than to each other.

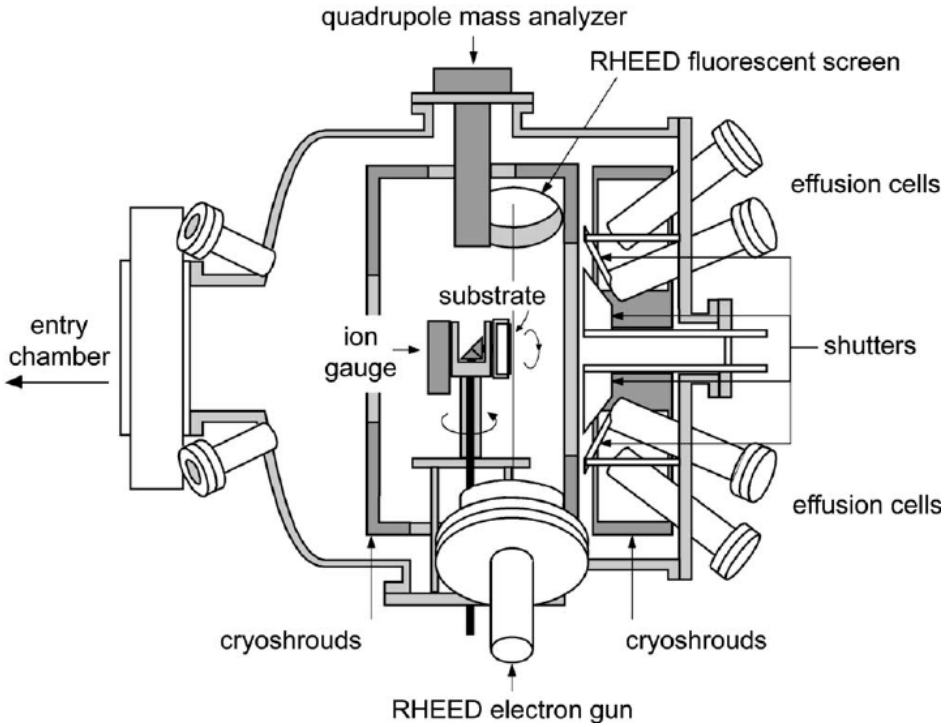

Figure 4.1: Schematic of MBE growth chamber [37]

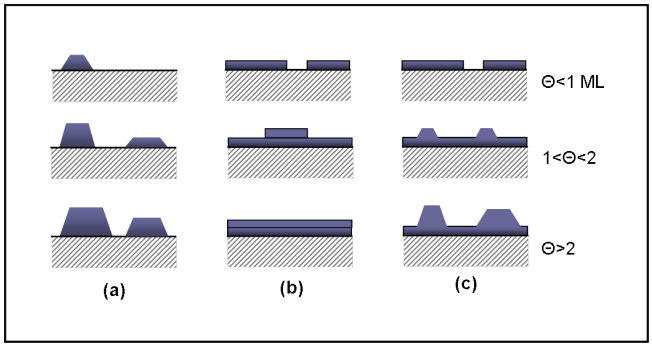

Figure 4.2: Thin-film growth mode: (a) Volmer–Weber , (b) Frank–van der Merwe , and (c) Stranski–Krastanov.[17]

2) Volmer–Weber (VW) mode, where adatoms bound to each other strongly rather than to the surface, forming 3D islands during the growth when he surface energy is minimized. (figure 4.2 (a)). 3) Stranski–Krastanov (SK) mode (figure 4.2 (c)). which is a mixture of layer plus island growth. The growth form 2D layer initially, then transit to island formation shortly. Transition from the 2D to 3D growth occurs at a critical thickness which dependents on the lattice parameters mismatch between the substrate and the layer material. The gradual accumulation of strain leads to island growth. A good example of the SK growth mode is the growth of InAs self-assemble quantum dots on GaAs substrate using MBE.

While the crystal growth is a competition between thermodynamics and kinetics, and that the surface thermodynamic analysis is useful in understanding the general direction that the growth tends to develop, the detailed mechanisms of MBE growth are better described with kinetics since the growth take place far from equilibrium. Processes like adatom adsorption, desorption, nucleation, growth and surface diffusion should be considered when describing the kinetics of the epitaxial growth. Adsorption and desorption of the atoms are quantified by sticking coefficient which depends strongly on the specific material and growth condition. Take GaAs growth which favors using As_2 for instance, compared to As_4, the sticking coefficient of As_2 can be maximize to unity on a Ga-rich surface. Adatom surface diffusion, which affects the

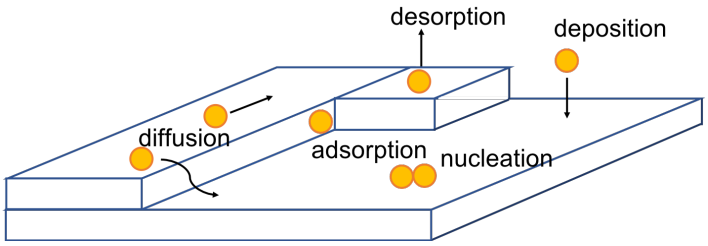

Figure 4.3: Schematic of growth processes occurs on the surface during MBE growth

surface morphology strongly, depends on the temperature and material. For example, at low growth temperature, adatoms have reduced surface mobility and will lead to island growth and rough surface. Atoms diffusing on the surface could either encounter another atom to nucleate, or get incorporated into a existing island. The kinetic processes are strongly dependent on growth parameters like growth rate (magnitude of the flux), growth temperature, group V species and group III/V flux ratio etc. The morphology of the layer can be optimized by carefully adjusting these growth parameters. More detailed discussion on how the growth parameters affects the crystalline quality will be discussed in next chapter.

The surface atoms with dangling bonds tend to rearrange to a different structure from the bulk crystal. This process is termed reconstruction. Surface reconstruction can be in-situ monitored during the growth by reflection high energy electron diffraction (RHEED). In the RHEED system, very high energy electron (usually 10-20 keV) is used to incident on the sample surface at grazing angle of less than 5 °. The diffraction pattern is observed on the phosphor screen and recorded by camera. The reconstructed surface structure have larger unit cell than the bulk, which is reflected on the RHEED pattern as dim fine spots between the bright fundamental spots. Wood's notation that is based on the ratio of unit cell parameters between the surface and bulk structure is used to describe the surface reconstruction. The RHEED pattern is very sensitive to surface morphology, and changes with growth condition. For example, under the normal growth condition, As-terminated GaAs (100) surface displays a (2x4) pattern while Ga-terminated GaAS (100) suface displays a (4x2) pattern. The shape of the

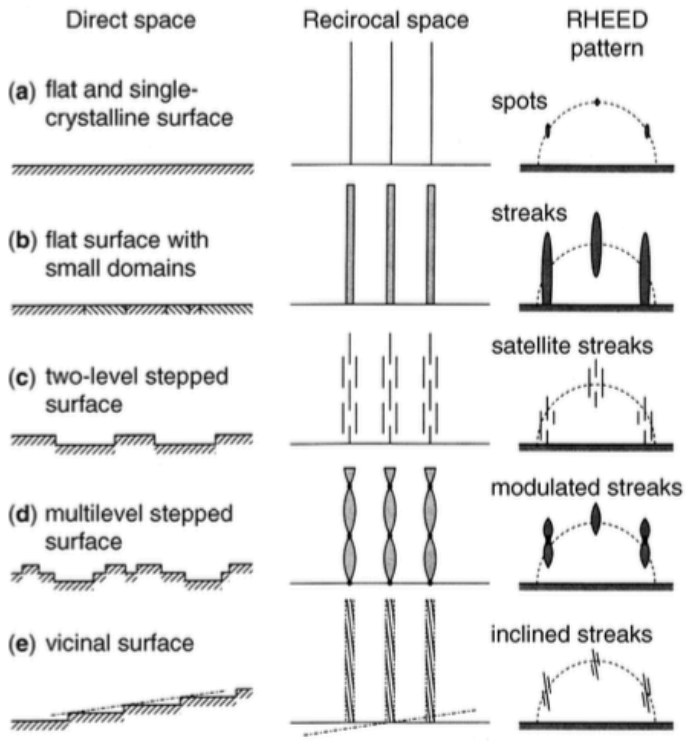

Figure 4.4: Schematics of different surface and their corresponding RHEED patterns[45].

RHEED spot also change with morphology. Examples of different types of surface morphology and the corresponding RHEED spot shapes are shown in figure 4.4. RHEED pattern provides feedback on the surface, as a streaky pattern indicates smooth surface, a spotty pattern indicates rough surface. Surface with oxides yield hazy pattern. Transition from hazy to clear RHEED pattern is useful when preparing the wafer before growth. RHEED is also capable of providing information regarding layer growth rate through monitoring the intensity oscillation which changes as the surface changes between flat and stepped.

4.2 Characterization Techniques

Samples are characterized by various characterization techniques. In this section, I will present brief introduction on some of the techniques used in characterizing

the samples, including high resolution X-ray diffraction, Rutherford backscattering spectrometry and spectroscopic ellipsometry.

4.2.1 High Resolution X-ray Diffraction on Epitaxial Film

High resolution X-ray diffraction (HRXRD) is a powerful tool in characterizing the epitaxial sample structural properties. High-resolution PANalytical X'Pert PRO materials research diffractometer at University of Delaware is used. Bragg's law states that the diffraction in a crystal occurs when the spacing of plane (hkl) d_{hkl}, scattering angle θ and x-ray wavelength λ satisfy the following equation:

$$2d_{hkl} \cdot sin\theta = n\lambda \tag{4.1}$$

The diffraction condition can also be expressed in reciprocal space as:

$$\vec{k_f} - \vec{k_i} = \Delta\vec{k} = \vec{G} \tag{4.2}$$

Equation 4.2 means that the difference between the incident and diffracted wavevector ($\vec{k_i}$ and $\vec{k_f}$ respectively) must equal to the reciprocal lattice vector ($\vec{G}$) for diffraction to occur. In the Ewald construction as shown in figure 4.5, drawing a Ewald sphere with diameter equals to $\frac{2\pi}{\lambda}$ when the origin of reciprocal space is placed at the tip, diffraction will occur only when the Ewald sphere cuts a reciprocal lattice point that represents planes in real space. In HRXRD, monochromatic X-ray Cu K_α with wavelength of 1.54056 Å is used.

4.2.1.1 $\omega - 2\theta$ Coupled Scan

A schematic of the measurement geometry is shown in figure 4.6. The data are collected in $\omega - 2\theta$ coupled scan geometry. ω is the incident angle between the X-ray source and the sample. 2θ is the diffracted angle between the detector and the incident ray. During the scan, the ω changes while the 2θ changes with the ω in a way that keeps $\omega = \frac{1}{2} \cdot (2\theta)$. The coupled scan plots the X-ray intensity vs. ω or θ, and can be used to study sample composition based on the peak position and Vagard's law

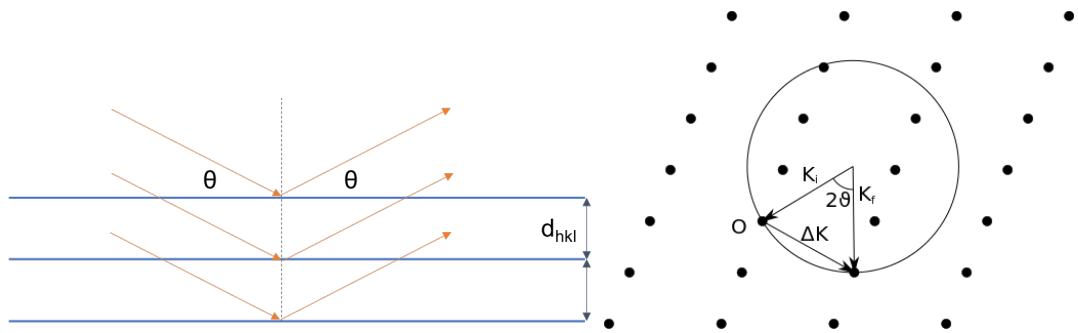

Figure 4.5: Left: Bragg's diffraction condition; Right: Ewald construction[18].

which describes the linear relation between the lattice constants of alloy $A_{1-x}B_x$ and the constituting components A and B as:

$$a_{A_{1-x}B_x} = (1-x)a_A + xa_B \tag{4.3}$$

$$a = \sqrt{h^2+k^2+l^2} \cdot d_{hkl} \tag{4.4}$$

Equation 4.4 is true for the cubic structure crystals studied in this dissertation. HRXRD is capable of examining fine structures that present near a diffraction peak in the epitaxy samples where the layers usually have very close lattice constants. Typically scan range is around 1° with step size as small as 0.0001°. The $\omega - 2\theta$ scan can also be used to calculate the thickness of the layers. To calibrate the MBE flux - growth rate relation, a set of film with total thickness around 1 μm are grown under different source flux. Thickness of the film were determined from HRXRD fringes. Fringes around the peak arise from the constructive and destructive interference of X-ray reflected from smooth interfaces and the period is related to the thickness of the layer (figure 4.7 and equation 4.5).

$$thickness = \frac{(n_1 - n_2)\lambda}{2(sin\omega_1 - sin\omega_2)} \tag{4.5}$$

4.2.1.2 Reciprocal Space Mapping

In a heteroepitaxy system where the epitaxial film is lattice mismatched to the substrate, the film could be either strained or relaxed (figure 4.8). For a strained film,

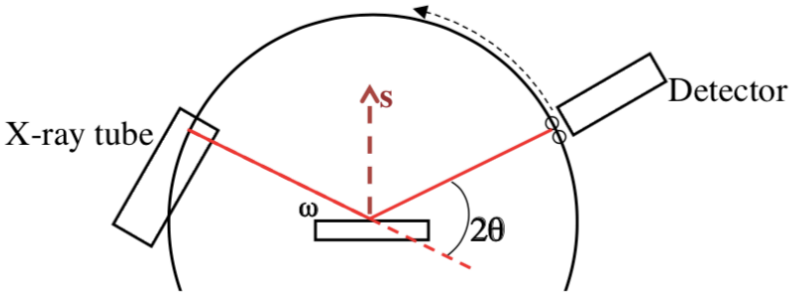

Figure 4.6: Geometry of X-ray diffraction setup[99].

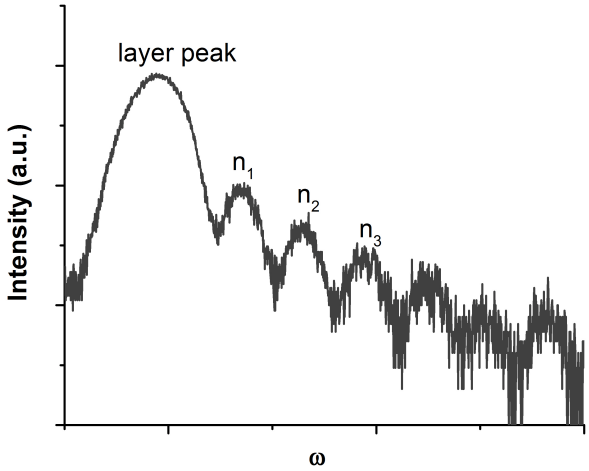

Figure 4.7: Interference fringes in the XRD.

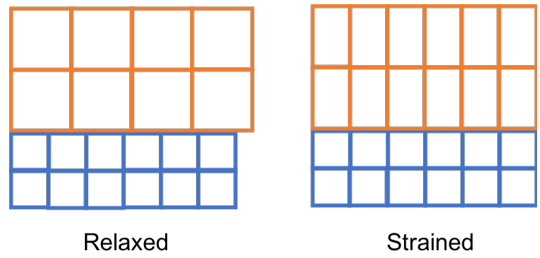

Figure 4.8: Schematic of relaxed and compressive strained epitaxy layer.

the lateral lattice constant is forced to be the same as the substrate, distorting the film unit cell. When the film is fully relaxed, the lattice parameters of the film are equal to those of the bulk material. Reciprocal space mapping (RSM) combines the ω scan with the $\omega - 2\theta$ scan and investigate a region around the reciprocal point of interest. The mapping allows for studying the strain and lattice relaxation in the sample. Figure 4.9 shows the schematic of the reciprocal space map of a relaxed heteroepitaxy system, where the red dots represent the substrate and the black dots represents the epitaxial overlayer reciprocal points. The black frame indicates the RSM scan range. Lattice mismatch could be determined from the RSM scan.

The reciprocal coordinates, (Qx, Qz), are expressed with reference to the angular positions as follows in the unit of rlu (reciprocal lattice unit):

$$Qx = R(cos\omega - cos(2\theta - \omega)) \tag{4.6}$$

$$Qy = R(sin\omega + sin(2\theta - \omega)) \tag{4.7}$$

$$R = 1/\lambda \tag{4.8}$$

4.2.2 Rutherford Backscattering Spectrometry

Rutherford backscattering spectrometry (RBS) is used to study the compositional and structural properties of the material. The samples are measured in the ion beam analysis facilities in Rugters University and University of Minnesota. In a RBS measurement, high energy ions (He^{2+}, 2 MeV) bombard the sample. The elemental

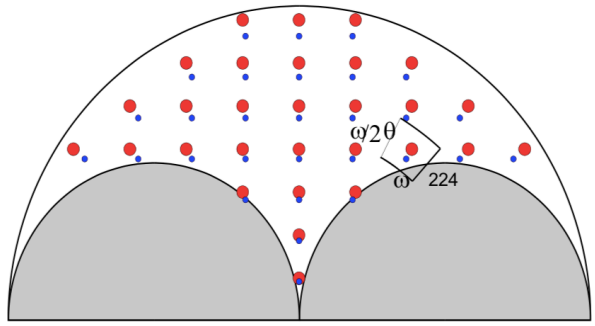

Figure 4.9: Schematic of a relaxed epitaxy layer (blue dots) on a substrate (red dots) in reciprocal space. The black frame is the RSM scan range in (224) plane. [74]

and depth information of the sample are obtained by measuring and analyzing the backscattered ions at a particular angle. The energy of the backscattered particle depends on the mass of the nuclei, elemental density and depth in the sample. A RBS spectrum plots the intensity of the detected backscattered ions as a function of signal intensity. SIMNRA software is used to analyze the experimental data. An example is given in figure 4.10. The position of the peak depends on the mass of the element and its depth in the sample. The width and height of the spectrum peak depends on the elemental concentration and depth in the sample. Elemental contribution to the full spectrum can be resolved. Ion channeling on single crystal samples is another powerful technique provided by RBS. It can be used to determine the crystal defects. When the ion beam is aligned with the crystal direction, the number of backscattered ions is greatly reduced unless interstitial defects exist in the sample.

4.2.3 Spectroscopic Ellipsometry

Ellipsometry measures the change in polarization state of light reflected from the surface of a sample (figure 4.11). It can be used to characterize sample thickness, optical constants, surface and interfacial roughness, etc.. VASE variable angle spectroscopic ellipsometer(J.A.Woollam) in Institute of Energy Conversion at University of Delaware

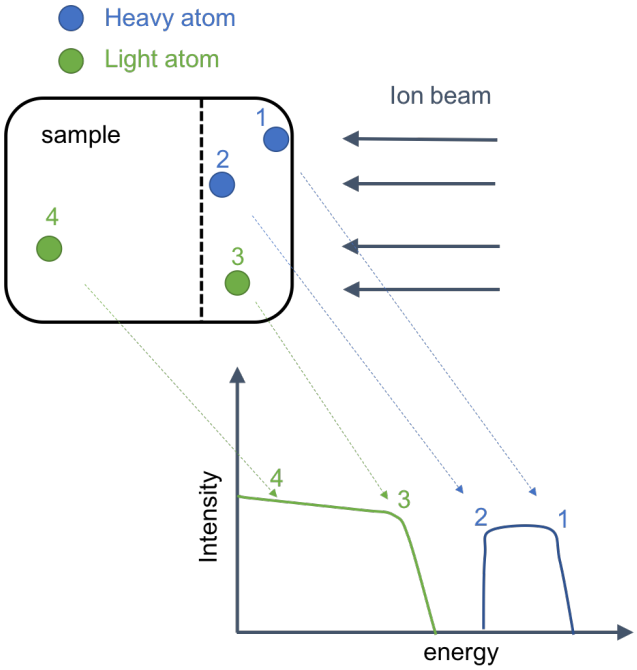

Figure 4.10: Illustration of RBS spectrum from a sample with heavy surface atoms in black solid dots (m_3, Z_3)and light substrate atoms in empty dots (m_2, Z_2). Modified based on reference [6].

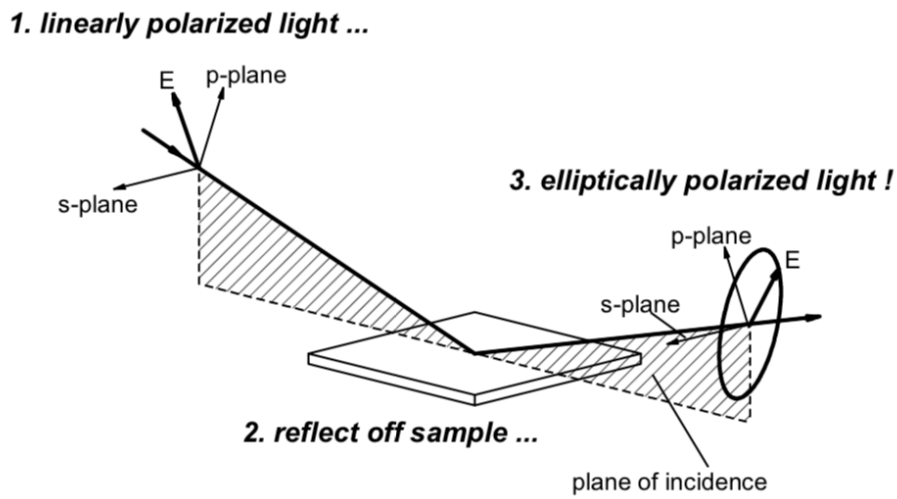

Figure 4.11: Geometry of the spectroscopic ellipsometry experiment[52].

was used to conduct measurements.

The linearly polarized light reflected off the sample surface is measured by the combination of rotating analyzer and detector which transform light signal to electric signal. General procedures involves measuring sample, developing model and fitting the model to experimental data. Regression analysis is implemented for the fitting process. The measured values are expressed in Ψ and Δ that relate to the Fresnel reflection coefficients R_s and R_p by equation 4.9. The polarization of the light is defined in the direction and phase of the electric field component of the light. The subscript p represents the p-direction which is in plane with the plane of incident. Subscript s represents the direction that lies perpendicular to the p-direction. The Fresnel coefficient describes the change in electric field of light, and is a function of optical constants of the materials and angles of light propagation.

$$\rho = \frac{R_p}{R_s} = \tan(\Psi)e^{i\Delta} \tag{4.9}$$

4.2.3.1 Optical Constants

The optical constants can be expressed in the form of complex dielectric function (equation 4.10) or complex refractive index (equation 4.11). The dielectric function describes how the material responds to the applied electric field, while the refractive index can describes how the materials affect the light propagating through the material. The optical constants is a function of wavelength, and the real and imaginary parts obeys Kramers-Kronig relationship. Thus the optical constants can be modeled using functional forms.

$$\tilde{\varepsilon} = \varepsilon_1 - i\varepsilon_2 \tag{4.10}$$

$$\tilde{n} = n - ik = \sqrt{\tilde{\varepsilon}} \tag{4.11}$$

Critical points that occur at energy band extrema or saddle points, usually with high symmetry, has large joint density of states and large transition probability which contribute to prominent features in the imaginary part of dielectric function ε_2. Therefore, we could extract information of interband transition energies from spectroscopic ellipsometry measurement. An example of the energy band diagram and ε_2 of InAs from theory calculation is shown in figure 4.12. The transitions are labeled on each figure.

4.2.3.2 Parametric Model

Parametric model, developed at the J. A. Woollam Co., Inc. by Craig Herzinger and Blaine Johs[47], is very useful for analyzing dielectric and semiconducting materials that have complicated critical point structures. The model uses parameterized functions to describe the critical point structures. Each critical point structure is composed of 4 polynomial with total of 12 parameters. sets of functions, each associated with one critical point feature. The complex dielectric function $\tilde{\varepsilon}$ can be written into a function of photon energy that contains broadening function and unbroaden absorption spectrum.

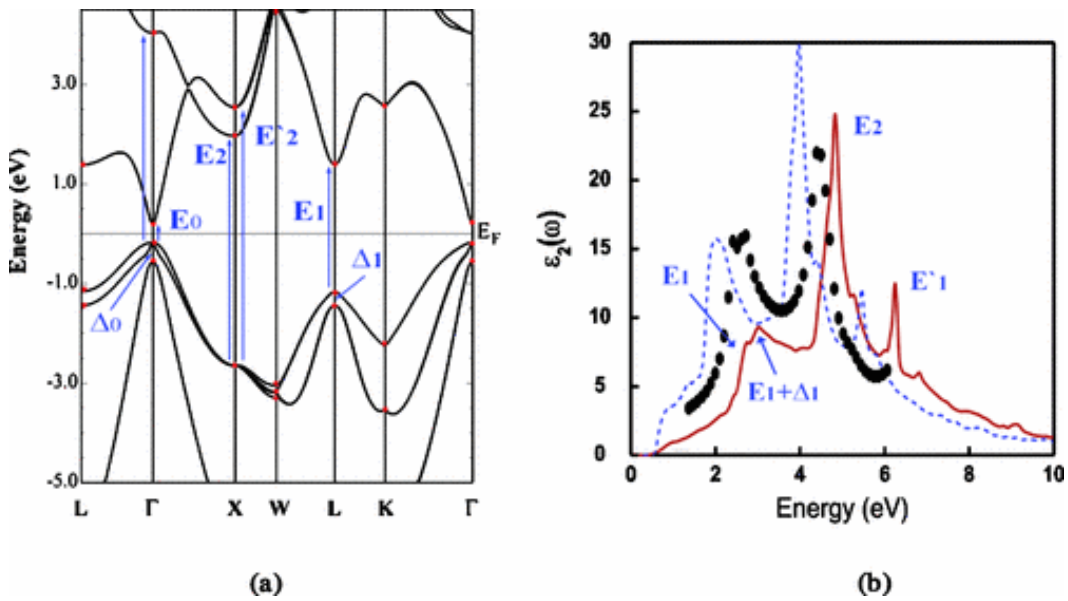

Figure 4.12: (a)Band structure of InAs. High symmetry points are shown in circles and important interband transitions are labeled; (b) Imaginary dielectric constant from theory calculation (solid and dashed lines) and experiment (filled circles).[84]

For example, figure 4.13 shows the dielectric function of GaAs with both tabulated spectra from literature and parametric model fit with seven critical point structures. As shown in the figure, parametric model is capable of reproducing the data accurately even with fine details. Some III-V or II-VI semiconductors have established parametric model. And some of the parameters are global values determined for several materials. Therefore the number of parameters that need to be fit is greatly reduced when working on a new material basing on a known, well-studied material.

The figure of merit used in the fitting process is mean square error (MSE) that presents the quality of the match between the data calculated from the model and the experimental data:

$$\begin{aligned} MSE &= \sqrt{\frac{1}{2N-M}\sum_{i=1}^{N}\left[\left(\frac{\psi_i^{mod}-\psi_i^{exp}}{\sigma_{\psi,i}^{exp}}\right)^2+\left(\frac{\Delta_i^{mod}-\Delta_i^{exp}}{\sigma_{\Delta,i}^{exp}}\right)^2\right]} \\ &= \sqrt{\frac{1}{2N-M}\chi^2} \end{aligned} \tag{4.12}$$

where N is the number of experimental data pairs of ψ and Δ, M is number of variable

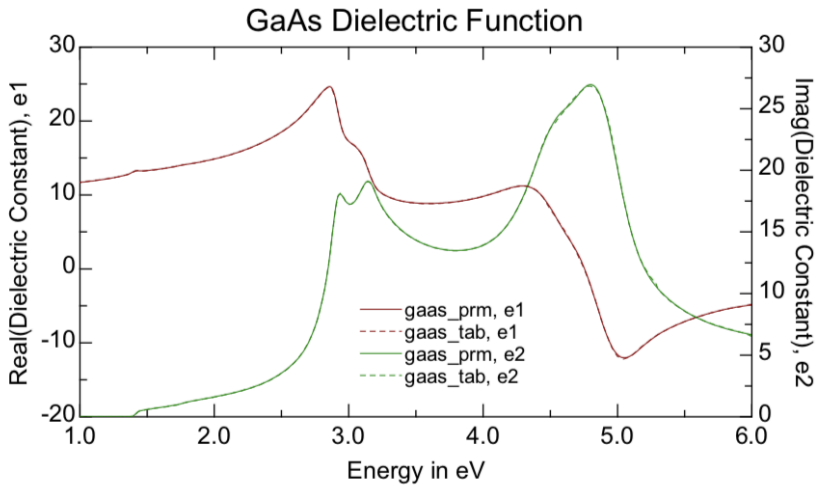

Figure 4.13: GaAs dielectric function. The legend $gaas_tab$ denotes the tabulated spectra from the literature, while $gaas_prm$ denotes the spectra calculated from the best-fit parametric semiconductor model for GaAs.[52]

parameters in the model, and σ is the standard deviation of the experimental data. Small MSE is desired.

Chapter 5

GROWTH AND CHARACTERIZATION OF DILUTE BISMUTHIDES

We proposed to use InAlBiAs in the funnel region of the upconversion nanostructure. The graded band structure of this region requires the material band could be flexibly engineered. The advantage of using dilute bismuthides is that it provides an extra degree of freedom in band engineering which will be discussed in details later. In this chapter, I will focus on the growth and characterization on the Al-containing dilute bismuthides: AlBiAs and InAlBiAs. First I will introduce background information of dilute bismuthide in section 5.1. The growth and characterization of InAlBiAs and AlBiAs are discussed in section 5.2 and section 5.3 respectively.

5.1 Introduction to Dilute Bismuthides

Dilute bismuthides are type of highly mismatched alloy (HMA), which contain an element that is significantly different from the matrix elements in terms of size and electronegativity. The covalent raidus of Bi is 1.46, which is much larger than As. Another example of HMA is the dilute nitrides, where N is much smaller than Ga, As etc.. HMA are difficult to synthesize due to the high miscibility gap. Therefore they are mostly studied in the dilute range, and requires specific growth conditions. MBE growth, being kinetically driven, is a great tool to overcome the miscibility gap issue. Other examples of HMA are II-VI oxides, and IV materials such as GeSn. Examples of dilute bismuthides are GaBiAs, InAsBi, InGaBiAs, InPBi, InSbBi, etc.[34, 38, 22, 87, 82].

By adding a small amount of Bi into the conventional III-V semiconductor, the host band gap is reduced significantly. In addition to the large band gap reduction from Bi incorporation, spin-orbit splitting increase with Bi content, and can become

larger than the band gap. This is a property that is strongly desired in optoelectronic applications. Another intriguing property of the dilute dismuthides is the hypothesized temperature-insensitive band gap which could stabilize the laser emission wavelength with temperature without thermoelectric cooling system. It was observed in GaBiAs that adding Bi could significantly reduce the temperature sensitivity of the band gap [116, 117]. However, temperature-dependent band gap measurements do not suggest the same effect occurring in InGaBiAs[64, 19]. The dilute bismuthides have been shown to have great potential in applications like infrared lasers[15] , photodetectors[42], solar energy conversion[92, 104].

5.1.1 MBE Growth of Dilute Bismuthides

MBE is capable of synthesizing the materials with good crystalline quality. However, the growth window for dilute bismuthide is narrow. Generally, the growth requires low growth temperature, low group V overpressure. Bismuth incorporation depends strongly on the growth temperature (figure 5.1(a)). Works by Zhong et al. on $In_yGa_{(1-y)}Bi_xAs_{(1-x)}$ (InGaBiAs)[119] showed that it is necessary to grow at low temperature less than 330°C. This range of growth temperature is much lower than the normal GaAs or InGaAs growth temperature around 500°C. The Bi concentration increases as growth temperature decreases. At higher growth temperature over 330 °C, almost no Bi get incorporated into the film[119, 34]. Moreover, growth surface becomes rough and droplets starts to emerges[120, 12] at higher growth temperature, indicating the difficulty of Bi incorporation into the film. Zhong et al.'s work showed that the Bi droplets are separated into two phases, with one side of much higher Bi concentration[119]. At normal InGaAs growth temperature above 450°C, no detectable Bi incorporation could be observed as a result of enhanced Bi desorption rate. Instead, bismuth acts as surfactant, yielding a smoother surface compared to film grown without Bi[34].

Increasing Bi/III flux ratio also increase the amount of Bi incorporation, as indicated in the figure5.1. The Bi% increases as increasing the Bi flux, although growing

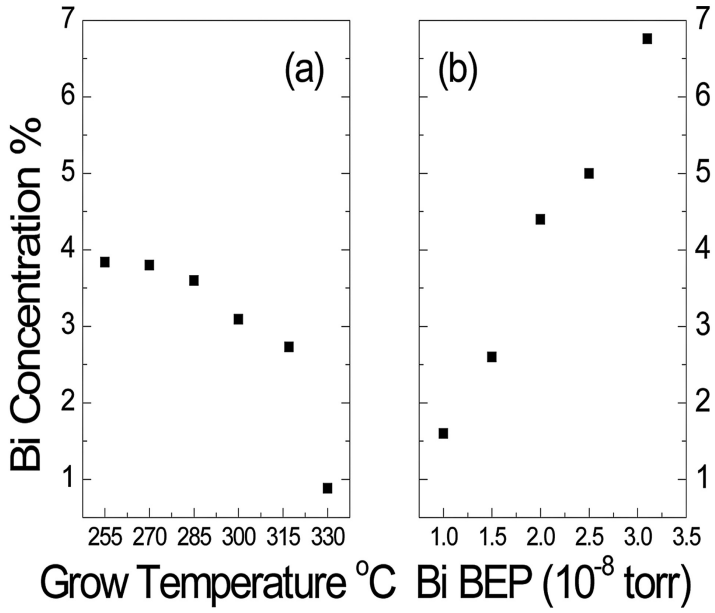

Figure 5.1: Effects of growth conditions on Bi incorporation in InGaBiAs. (a) Bi% dependence on growth temperature. (b) Bi% dependence on Bi BEP[119]

with high Bi flux can lead to problems such as the formation of Bi droplets and Bi concentration gradient within the film[119]. Another way to adjust the ratio is to lower the growth rate by lowering the group III flux. For InGaBiAs, decreasing the In/Ga flux ratio improves the amount of Bi incorporated somewhat[121], similar to the GaPBiAs study on the strain effect[72]. I have been able to incorporate up to 6% with less In%. without gradient

Bi% is very sensitive to arsenic flux. Bi% decrease with increasing As_2 flux. Group III atoms prefer to bond with As rather than Bi, therefore excess As atoms arriving during growth hinders the Bi incorporation[119]. When As flux is too high, no detectable Bi% is incorporated[56]. Dilute bismutihde is grown with As:III flux near stoichimetric, instead of the traditional large As overpressure[38]. However, low As flux could result in group III, like Ga, droplets. Careful control of III:Bi:As_2 flux ratio is necessary to incorporate Bi without Bi or III droplets. It was reported that when growing with As_4 instead of As_2, the As flux does not show significant impact on the amount of Bi incorporated [86, 11], and the growth temperature lower than 330°C

does not affect the amount of Bi incorporate into the film[12].

The incorporated Bi atoms locate on substitutional sites in InGaAs lattice, as confirmed by channeling RBS[35, 119]. Both RBS and HRXRD confirms good crystalline quality even grown at low temperature. Although adding Bi into InGaAs (with In/Ga ratio close to lattice matching to InP) introduces compressive strain to the film, Zhong et al. have reported the growth of InGaBiAs film of several hundred nanometers thick, which remains fully strained to the InP substrate and far exceeding theoretical critical thickness[119]. While MBE is capable of producing good quality Bi-containing thin film, the low solubility of Bi can lead to alloy disorders like Bi clusters, phase separation and atomic ordering exit in the alloy[76].

5.1.2 Valence Band Anti-crossing

For ternary alloy, the band gap is a quadratic function of the composition:

$$E_g(A_{1-x}B_x) = (1-x)E_g(A) + xE_g(B) - cx(1-x) \tag{5.1}$$

where c is the bowing parameter. A and B are constituting binary compound. For example, InGaAs is the alloy of InAs and GaAs. However, the large band gap bowing in the HMA cannot be explained with the virtual crystal approximation (VCA). Shan et al. first proposed a band anti-crossing (BAC) model in explaining the strong bowing behaviour in the dilute nitrides[95]. Alberi et al. successfully applied the BAC theory to the GaSbAs and GaBiAs[5]. As shown in the figure 5.2 (a), where experimental determined band gap of GaBiAs deviate significantly from the dashed line representing VCA calculation while the BAC solid line is able to fit the experimental data fairly well. Unlike the dilute nitrides where the N primarily perturbs the conduction band, Bi mostly interact with the matrix in the valence band. The localized Bi impurity level locates in the host matrix valence band (GaAs or InGaAs, for example), causing the split of the valence band and upwards shift of VB, leading to large band gap reduction (see figure 5.2 (b)). Hence valence band anti-crossing (VBAC). The interaction between

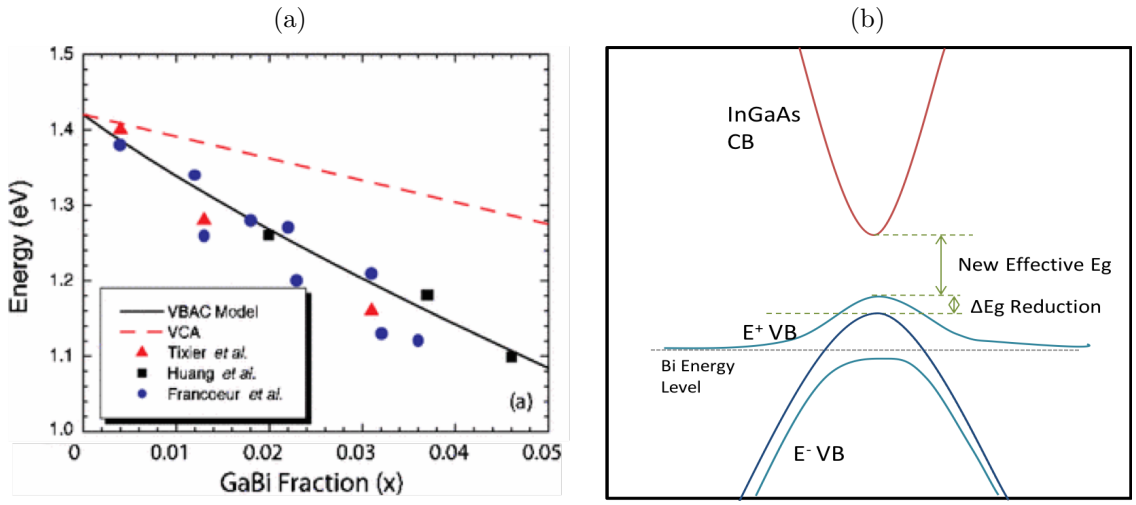

Figure 5.2: a): Band gap of $GaBi_xAs_{1-x}$ over the full composition range.[5]; b): VBAC of InGaBiAs [120]

the extended states of the matrix and the localized Bi states is treated as perturbation which leads to the following eigenvalue problem:

$$\begin{vmatrix} E - E_M & \sqrt{\beta}x \\ \sqrt{\beta}x & E - E_{Bi} \end{vmatrix} = 0 \tag{5.2}$$

This predict the splitting of VB into two subbands $E+$ and$E-$. The new VB energy of the (III)$Bi_xAs_{(1-x)}$ could be expressed as:

$$E_M^+ = \frac{(E_M + E_{Bi}) + \sqrt{(E_M - E_{Bi})^2 + 4\beta x^2}}{2} \tag{5.3}$$

where E_M is the energy of the matrix valence band edge, E_{Bi} is the energy of the Bi impurity state, and β describes the interaction strength between the matrix VB and the Bi impurity state that depends on both group III composition and Bi% [80]. More sophisticated model such as tight-binding and 12 band k·p model have also been studied[19, 109]. Band gap reduction around 88 meV/%Bi was observed in GaBiAs [38] and around 56 meV/%Bi in InGaBiAs [80]. The experimental data agree fairly well with the theory in the low Bi content InGaBiAs, while the higher Bi content (> 5%)

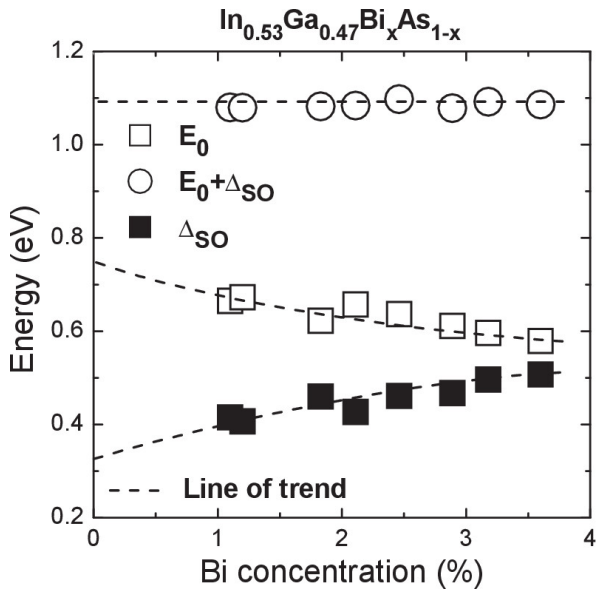

Figure 5.3: E_0 (open squares) and $E_0 + \Delta_{SO}$ (open circles) energies of $In_{0.53}Ga_{0.47}Bi_xAs_{1-x}$ of various Bi% obtained from CER measurements[54]

experimental band gap deviate from the theory prediction. This is possibly due to the Bi disorder strongly affecting the band structure[19]. As shown by works done using photoreflectance and contactless electron reflectance measurements (figure 5.3), while the spin-orbit splitting Δ_{SO} increase with Bi content, $E_0+\Delta_{SO}$ stays relatively constant [54, 64], indicating that the band gap reduction occurs largely from the upwards shifting of the valence band edge.

As the Δ_{SO} increase with Bi content, it was predicted that the $E_g = \Delta_{SO}$ crossover point for GaBiAs should occur when Bi% of 10.5%. And for InGaBiAs, the crossover point should occur when $E_g < 0.55eV$, around 3.2% Bi at RT (another study suggests 3.8% [19]). Experimentally, it has been observed $\Delta_{SO} > E_g$ for $InGaBi_{0.058}As_{0.942}$, with $E_g = 550meV$, and $\Delta_{SO} = 620$ meV, respectively[19]. With the Δ_{SO} larger than the band gap, Auger recombination and inter-valence band absorption (IVBA) are largely suppressed, which is ideal for improving the performance of devices like mid-IR lasers.

I will discuss the MBE growth and characterization in the order of InAlBiAs in

section 5.2 first, and then AlBiAs in section 5.3.

5.2 InAlBiAs

Prior to growing InAlBiAs we first explored the effect of arsenic species on the Bi incorporation on InGaBiAs. The requirement of As_2:III flux being close to the stoichimetric ratio could be less stringent when switching the As species to As_4. The affect of As_4 BEP on Bi incorporation in quaternary alloy was explored on $In_{0.54}Ga_{0.46}BiAs$. The result is shown in figure 5.4. Limited amount of Bi could be incorporated into the film under high As overpressure. There seems to exist a sharp increase of Bi% once the As_4 BEP is in the correct range. And the Bi% does not change with As_4 BEP fallen within that range, similar to what was observed in GaBiAs[11]. InGaBiAs grown with high Bi flux and As_2 of 2×10^{-6} torr yields Bi gradient, which means the Bi% along the growth direction is not uniform and that Bi% is higher closer to surface. Small droplets could also be observed under optical microscope. Reducing the As_2 flux some or slowering the growth rate did not improve the quality. However, the gradient and droplets on the surface were not observed when substituting As_2 with As_4 while keeping the other growth conditions the same. If the Bi gradient exists, the RBS Bi signal shape would become a slope (figure 5.5) instead of a flat platform. As_4 was used for all the (In)AlBiAs growth in the following sections. To incorporate more Bi, In% could be reduced some to reduce the strain. This is also studied in GaPBiAs[72]. Uniform Bi distribution on the growth direction InGaBiAs with Bi% up to 6.2% was obtained with a composition of $In_{0.42}Ga_{0.58}Bi_{0.062}As_{0.938}$.

$In_xAl_{1-x}Bi_yAs_{1-y}$ thin film was grown on 500μm (001) InP Fe-doped substrate. Surface oxides on InP wafer was removed by heating the substrate temperature to 565°C (cooled down immediately after reaching 565°C to avoid melting the wafer) and repeated for several times until clear RHEED pattern could be observed. InAlBiAs was grown directly on InP substrate at 300°C. As mentioned in the last chapter, low temperature monitoring with BET is difficult at 300°C. Therefore the actual temperature fluctuate about 5°C. In/Al BEP ratio was chosen to be close to $In_{0.52}Al_{0.48}As$ latticed

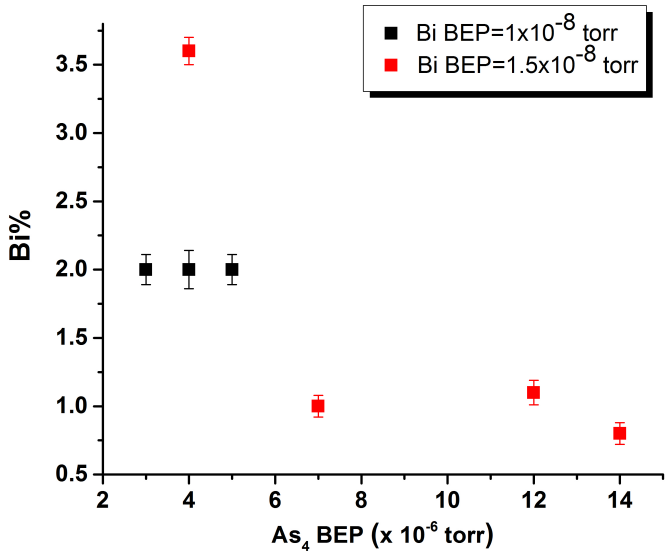

Figure 5.4: Bi% changes with As_4 BEP in $In_{0.54}Ga_{0.46}Bi_yAs_{1-y}$.

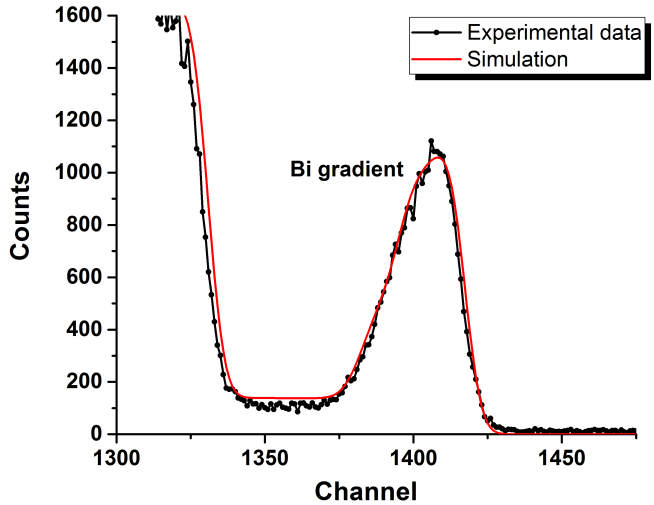

Figure 5.5: Bi signal in RBS as a result of the presense of Bi% gradient along the growth direction.

matched to InP. In and Al BEP chosen based on calibration done on InAlAs grown at 490°C that would achieve InAlAs growth rate of 0.6 μm/hr. As_4 overpressure of 4×10^{-6} torr is used. Streaky RHEED was observed throughout the growth. However, the RHEED pattern could not be clearly identified due to the limited resolution as the phosphor screen was coated by As and Sb.

5.2.1 Characterization of MBE Grown InAlBiAs Film

RBS was used to identify both the group III and group V composition in the $In_xAl_{1-x}Bi_yAs_{1-y}$ samples. An example of the RBS spectrum with elemental contribution resolved is shown in figure 5.6. The step on the left side at channel number ≤ 325 is the signal from the InP substrate. Layers closer to surface and heavier atoms yield signals at higher channel number. The InAlBiAs layer contributes to the signal in the channel number from $\sim$ 450 to $\sim$570. Bi contribution is indicated by the green line that rise up at the right-most side of the spectrum around channel 550. The flat platform from Bi contribution indicates that there is no Bi concentration gradient along the growth direction. And no Bi droplets were observed under optical microscope on all the samples. In composition determined from RBS has an error range of ± 0.005. The relation between the Bi% and Bi BEP used for the growth is shown in figure 5.7. More Bi are incorporated in the film with higher Bi flux, until around BEP of 2×10^{-8} torr where Bi% seems to saturate around 3% under the given growth condition.

HRXRD $\omega - 2\theta$ scan on (004) plane was performed for all the samples. Figure 5.8 shows $\omega - 2\theta$ scan for InAlBiAs samples with Bi% from 2% to 3.2%. The sharp and intense peak at 63.3382° correspond to the InP substrate. The less intense peak to the left of the substrate peak correspond to the InAlBiAs layer. The layer peak locates at a lower angle than the substrate peak due to larger Bi atom incorporation. Very clear fringes could be observed for all the composition range, even for highest Bi% of 3.2%, indicating smooth interface could still be achieved under the growth condition and it is also supported by the observed streaky RHEED pattern throughout the growth. While the position of the XRD peak is a way of determining the composition using Vagard's

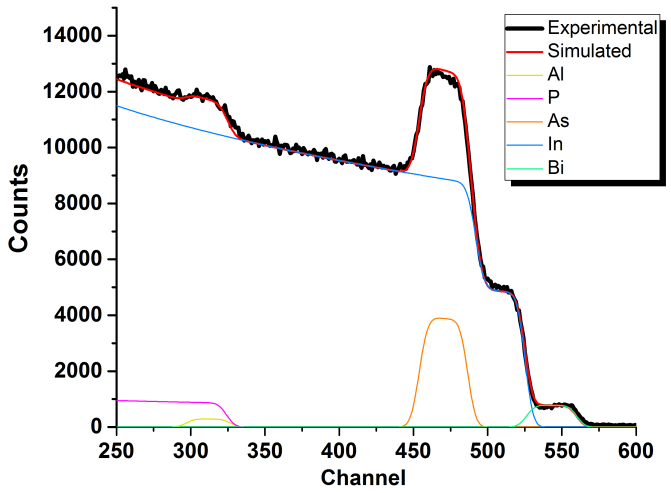

Figure 5.6: RBS spectrum of 200 nm $In_{0.56}Al_{0.44}Bi_{0.032}As_{0.968}$ thin film grown on InP substrate, with the black line corresponding to the experimental data and the red line corresponding to the simulation. Elemental contribution are indicated in colored lines other than the red line.

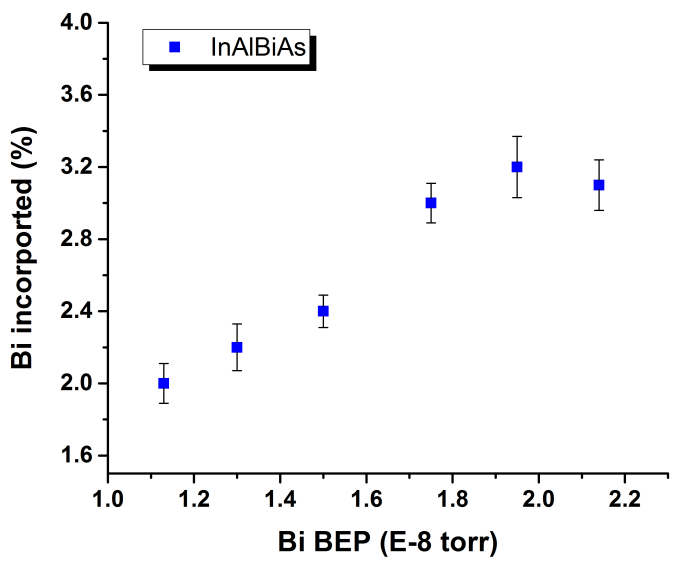

Figure 5.7: Bi% in InAlBiAs determined by RBS as a function of Bi BEP used in MBE growth, with error bars of Bi% shown.

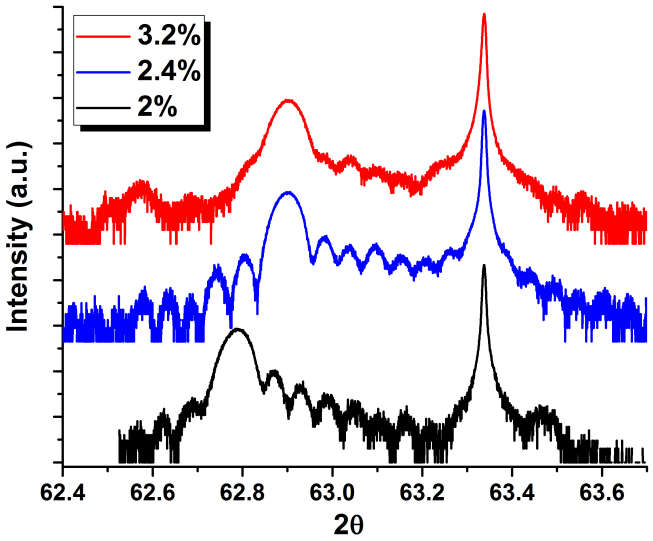

Figure 5.8: HRXRD $\omega-2\theta$ scans of InAlBiAs thin films with different Bi composition.

law. It is not applicable to quaternary InAlBiAs, because both group III and group V composition are unknown, and that XRD peak is affected by inhomogeneity and lattice super-dilation from Bi incorporation[120]. RBS is more suitable in determining the composition. InAlBiAs layer thickness is smaller than expected, around 90% of the expected thickness. The reduced growth rate at lower growth temperature was also observed in GaAs [68]. Reciprocal space mapping on (224) plane was performed on the sample with highest amount of Bi, which is more likely to relax. The result is shown in figure 5.9 with the fully strain line drawn. The strongest signal is from the InP substrate. The less intense peak is the signal from InAlBiAs. The InAlBiAs peak falls at vertical extension of the substrate peak, i.e. on fully strained line, indicating that the 200 nm film is fully strained to the substrate.

InP's band gap is 1.34 eV at room temperature, and $In_{0.52}Al_{0.48}As$'s band gap is 1.47 eV. Therefore absorption based method like spectrophotometry is not able to provide band gap information of InAlBiAs since the thick substrate will absorb at lower wavelength than the layer. And small amount of Bi will reduce band gap to be

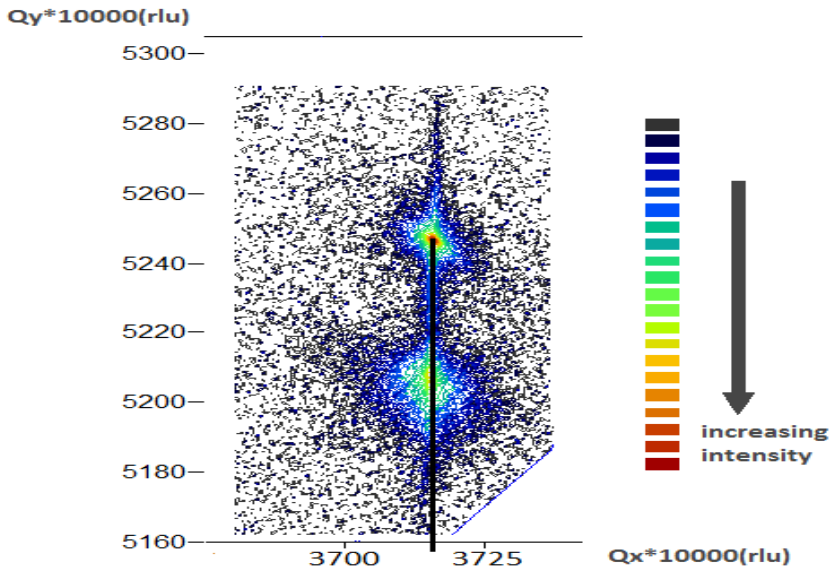

Figure 5.9: Reciprocal space mapping of $In_{0.55}Al_{0.45}Bi_{0.032}As_{0.968}$ on (224) plane with vertical black line showing the fully strained line.

close to the InP band gap. Therefore, photoluminescence signal will be cover by the substrate peak. We chose to use spectroscopic ellipsometry to characterize the band gap of InAlBiAs.

The substrate wafers used were double-side polished. So sand paper was used to create rough back-surface to prevent abnormal signal at the long wavelength due to the light reflecting from smooth back-surface being received by the detector. The measurements were taken with incident light wavelength from 265 to 1400 nm with step size of 5 nm, at incident angles of 68, 73 and 78 degree. Tabulated optical constants was used for InP substrate layer. The parametric model was used for InAlBiAs layer. Parameters from established InAlAs parametric model were used as initial values for InAlBiAs. The $In_{0.52}Al_{0.48}As$ parametric model was tested on $In_{0.52}Al_{0.48}As$ grown on InP, and was able to fit the reference sample very well. The Bruggeman effective medium approximation (EMA) was used to describe the surface roughness. EMA calculate the optical constants of mixture of materials of known optical constants and

is very useful for describing surface and interfacial roughness.

Four InAlBiAs samples with same composition ($In_{0.54}Al_{0.46}Bi_{0.024}As_{0.976}$) but different layer thickness of 50, 100, 200 and 300 nm were grown to perform multi-sample analysis to obtain the InAlBiAs parametric model values. Examples of the InAlBiAs raw ellipsometry spectrum are shown in figure 5.10. Most of the samples has MSE less than 2, which indicates a good fit between the model and the experimental data.

Band gaps of InAlBiAs were extracted from the model and plot as a function of Bi concentration in figure 5.11. Bi reduces the band gap strongly by $\sim$ 113 meV/% Bi, which is very large compared to 57 meV/% Bi reduction in InGaBiAs[80] and 88 meV/% Bi in GaBiAs[38]. VBAC was applied to fit the interaction parameter β in equation 5.3.

β was fit as a linear function of In%: $ax + b$, based on the InAlBiAs with Bi% less than 3%. The VBAC model reults are presented in figure 5.11 as colored solid lines with the coloring indicating different In%, corresponding to the scattered experimental points. The experimental values agree with the VBAC calculation well in the low Bi% range, while the measured band gap for InAlBiAs with $\sim$3% Bi deviate from the VBAC prediction. It is possible that Bi-related alloy disorder like Bi clusters within the sample affect the band structure strongly, which is not captured by the VBAC model. Further investigation on the theoretical model is needed to understand the effect. As mentioned in the previous section, this deviation from the VBAC theory was also observed in InGaBiAs with Bi% $\geq$ 5%. If we only consider Bi% $<$ 3%, band gap reduction is around 47 meV/%Bi.

From the ellipsometry, other critical points energies are also obtained. In figure 5.12, I show how critical points E_0 (E_g)and $E_0 + \Delta_0$ change with Bi%. The critical point energies of $In_xAl_{1-x}As$ are calculated using the reported composition-dependent expression [29]. The result suggest that $E_0 + \Delta_0$ energy is less affected by the incorporation of Bi compared to E_0, which is consistent with studies on GaBiAs and InGaBiAs.

(a)

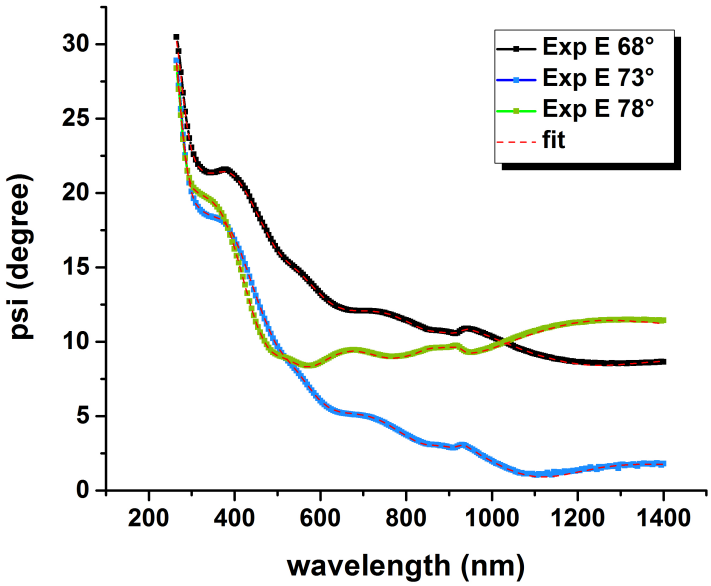

(b)

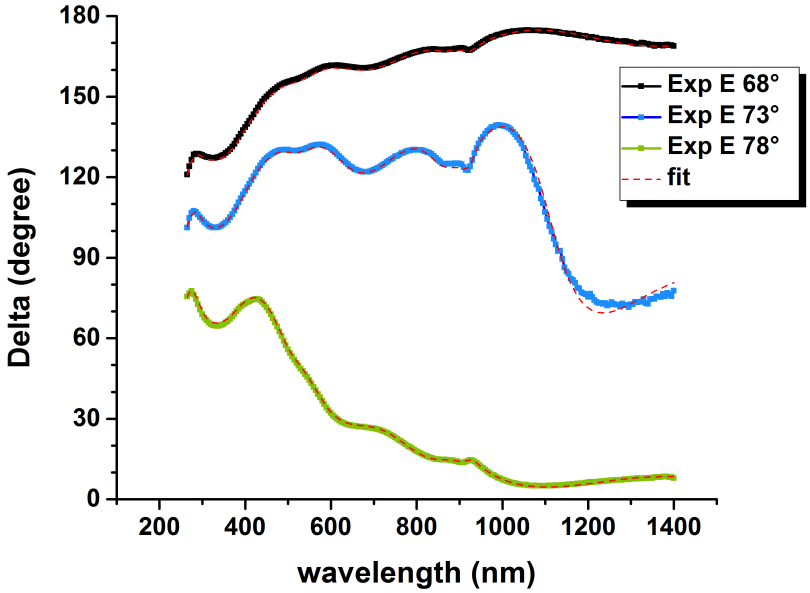

Figure 5.10: Example of InAlBiAs spectroscopic ellipsometry spectrum: a)Psi, b)Delta. Black, blue and green line are experimental data taken with incident angle of 68°, 73° and 78°. Dashed red line is the model fit.

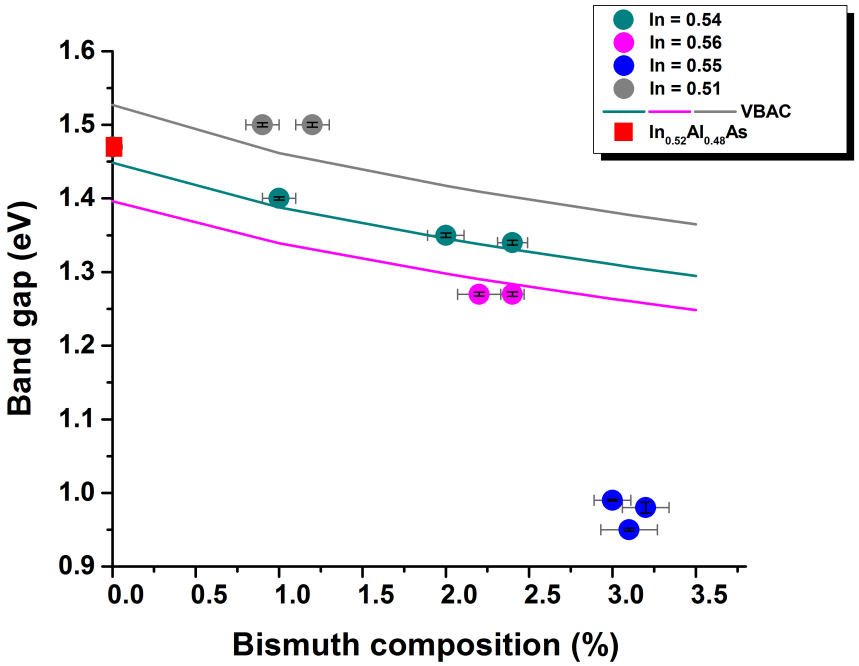

Figure 5.11: InAlBiAs band gap as a function of Bi composition. $In_{0.52}Al_{0.48}As$ lattice-matched to InP is also shown in red square as a reference. Sample groups with different group III composition are distinguished by color.

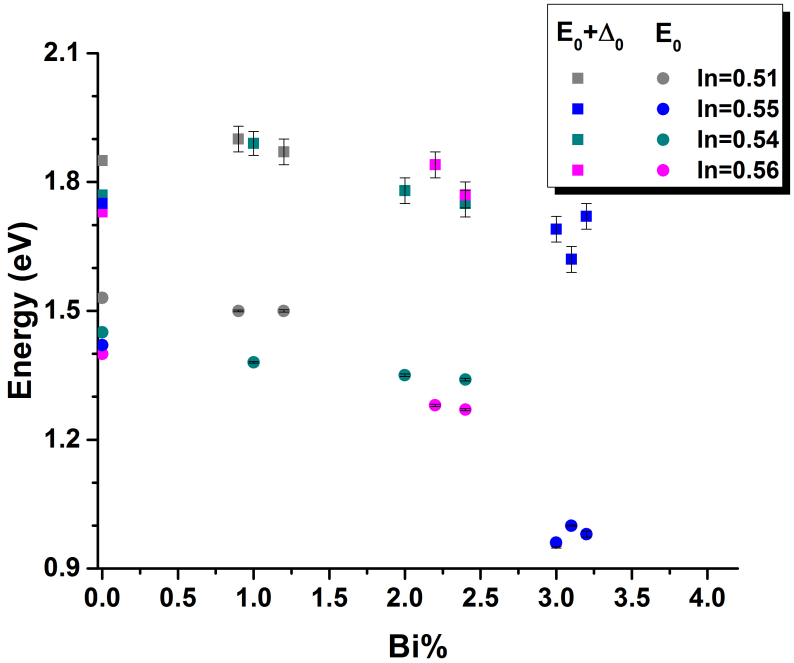

Figure 5.12: E_0 and $E_0+\Delta_0$ of $In_xAl_{1-x}Bi_yAs_{1-y}$, with the squares representing $E_0+\Delta_0$ and the circles representing E_0. Sample groups with different group III composition are distinguished by color.

Based on the VBAC, we could produce a contour map that provides InAlBiAs band gap in a wide range of composition, which is useful in determining the composition needed for growing a full upconversion structure. We applied the parameters obtained based on the samples discussed above, and created a contour map in figure 5.13. Although the assumption that the simple VBAC model is adequate to describe the band gap as a function of Bi% is only valid in the low Bi% range, the map could still act as a guideline for initial study and will be optimized should more experimental data and more sophisticated modeling are available. The preliminary calculation result in figure 5.13 plots the band gap of InAlBiAs in color scale as a function of In and Bi composition. InAlBiAs band gap could be direct or indirect based on the In composition. The horizontal dashed line at In= 0.37 indicates the crossover from indirect to direct band gap based on the InAlAs. To show how this map could be applied to upconversion nanostructure growth, I presents two examples drawn in the solid black lines with the end points composition marked on figure 5.13. One of the assumptions in upconversion nanostructure is that the valence band offset between the InAs and left side of the InAlBiAs barrier is zero, allowing for fast carrier escape. Any composition along the line on the lower left corner would satisfy this zero-valence-band-offset assumption. The band gap varies between $AlBi_{0.073}As_{0.937}$, 1.79 eV and $In_{0.37}Al_{0.63}Bi_{0.083}As_{0.927}$, 1.56 eV. Assuming that 150 meV photon energy sacrifice is introduced in the valence band and that the right side of the barrier to have direct band gap which is beneficial for photon emission, the available composition that meet the requirements fall on the solid black line on the upper right corner. The band gap varies between $In_{0.6}Al_{0.4}Bi_{0.15}As_{0.85}$, 0.94 eV and $In_{0.37}Al_{0.63}Bi_{0.16}As_{0.84}$, 1.41 eV.

5.3 AlBiAs

AlBiAs thin film with thickness of 200 nm were grown on 500μm (001) GaAs unintentionally doped substrate. The wafer was kept at 620°C for 10 minutes to remove the surface oxides under As overpressure of 1×10^{-5} torr. 50 nm GaAs buffer layer was grown at 530°C. After the buffer layer growth, substrate temperature was lowered and

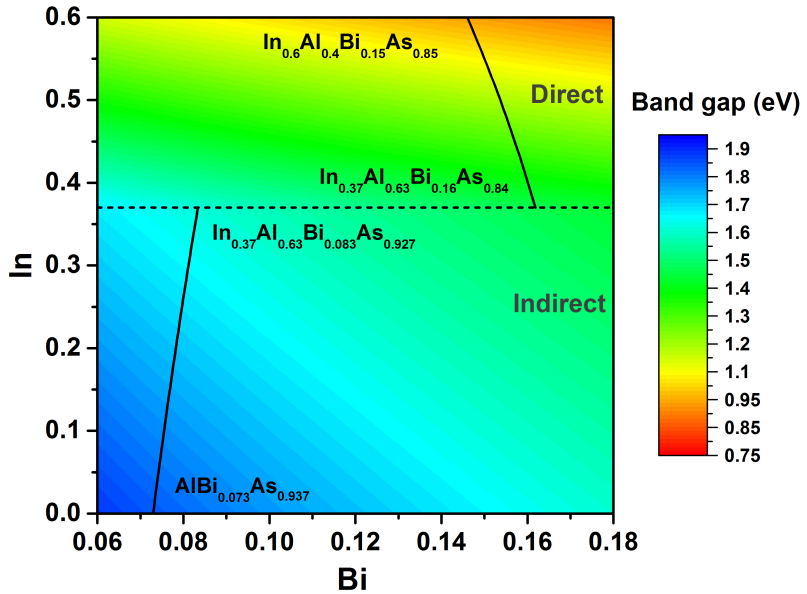

Figure 5.13: InAlBiAs band gap as a function of In and Bi composition calculated from the VBAC model.

As_4 BEP reduced to 4×10^{-6} or 2×10^{-6} torr for AlBiAs layer growth. Al BEP chosen based on the growth rate calibration grown at 530°C that would achieve AlAs growth rate of 0.6 μm/hr. As in the InAlBiAs growth, the actual growth rate is lower than expected at low growth temperature. 50 nm of GaAs cap layer was grown to protect AlBiAs from oxidation in the atmosphere.

Due to the malfunction of BET temperature monitor, AlBiAs were grown by setting the thermocouple (TC) steady at 400°C. Because the TC is located behind the substrate heater instead of directly contacting the wafer, the temperature read by the TC is much higher than the actual sample temperature. The actual temperature varies with factors like substrate type and substrate holder. Moreover, a steady TC temperature is not a good indicator of a steady substrate temperature.

Low temperature grown AlBiAs quality is poor. Al adatom on the surface has high chemical reactivity and slow migration mobility. Therefore high MBE growth

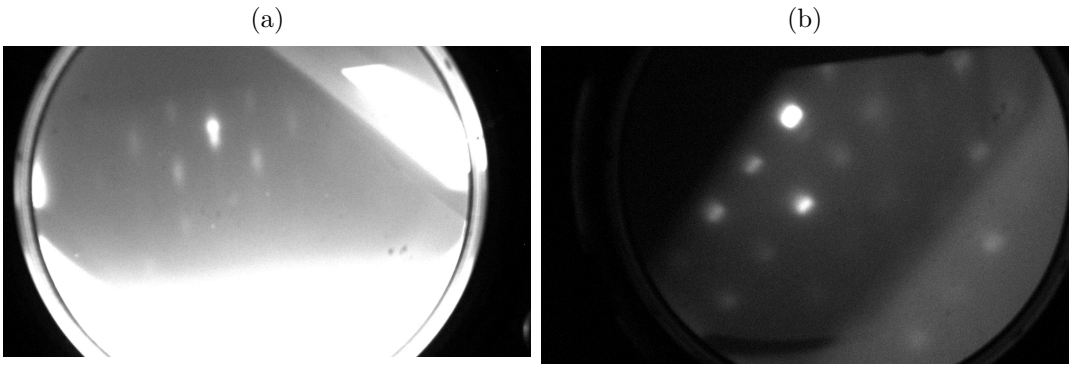

Figure 5.14: a) Streaky RHEED pattern observed during the first few tens of nanometer of AlBiAs growth. b) RHEED transitions into spotty pattern as growth proceeds.

temperature is neccessary to achieve high quality film. For example, AlGaAs is usually grown at temperature over 640°C[68]. Generally, the RHEED during the first tens of nanometers of AlBiAs layer growth was clear and streaky (see figure 5.14 (a)) similar to what was observed in the buffer layer, indicating that the surface was still relatively smooth. However, the RHEED transit into a spotty pattern (figure 5.14 (b)), indicating that the growth proceed as 3D island mode with rough surface. Two different RHEED patterns were also observed addition to the spotty RHEED pattern. Figure 5.15 shows one example where the RHEED spots is more diffused with satellite spots in one direction than the other. The RHEED turned into clear spotty pattern in both direction at the GaAs cap growth. Figure 5.16 shows another example where the diffraction pattern is arc-shape in one direction and a mixture of arc and spots in the other direction. The pattern suggest some degree of disorder with misorientation. This type of pattern was also observed in growth like GaN on GaAs[63]. Note that only two samples exhibit strange RHEED pattern in figure 5.15 and 5.16. The actual growth temperature being too low was probably the cause. All the other AlBiAs exhibit clear spotty pattern in both direction as shown in figure 5.14.

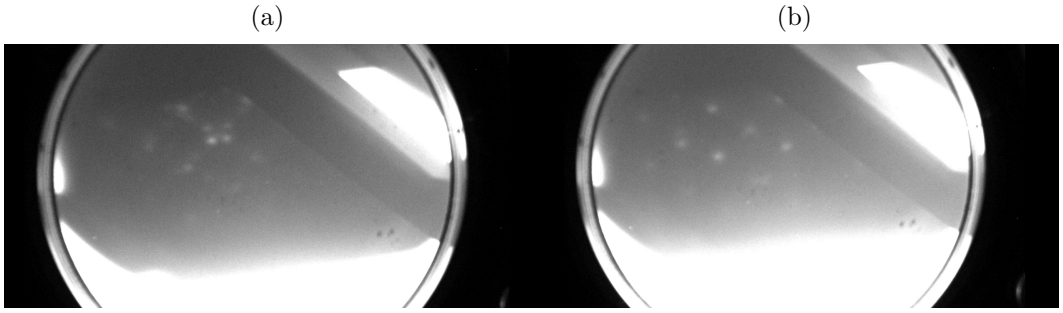

Figure 5.15: Another RHEED pattern observed during AlBiAs growth showing a) satellite spots in one direction and b) clear spots in the other.

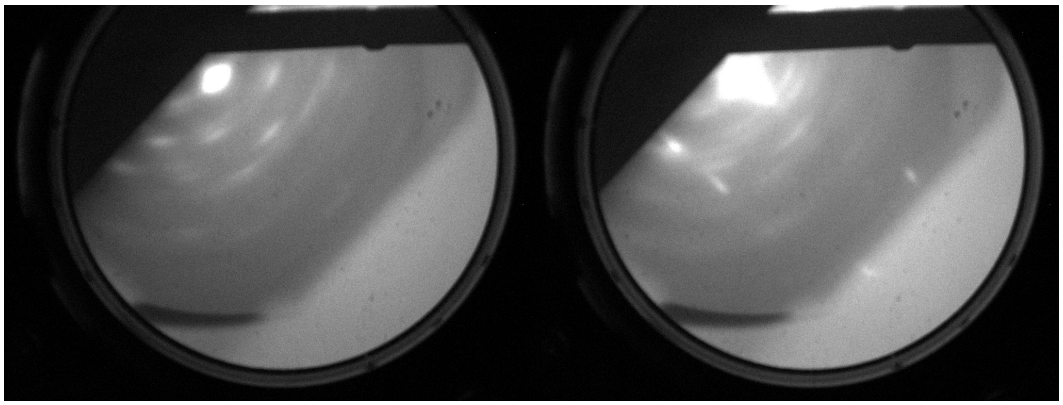

Figure 5.16: RHEED pattern during AlBiAs growth showing a) arc-shape pattern in one direction and b) arc plus spots in the other direction.

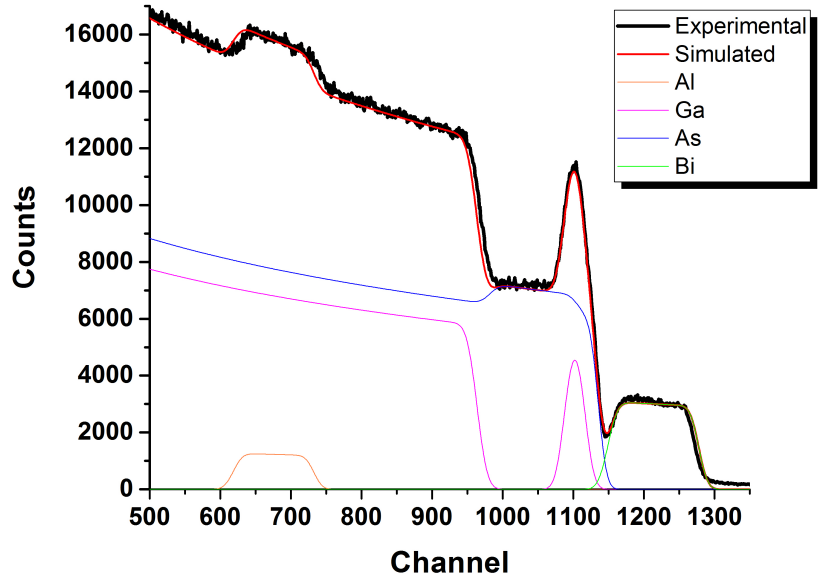

Figure 5.17: RBS spectrum of $AlBi_{0.066}As_{0.934}$.

5.3.1 Characterization of MBE Grown AlBiAs Film

An example of the AlBiAs RBS spectrum is in figure 5.17. The light Al atom in the AlBiAs layer contributes to the step from channel ∼650 to ∼750. GaAs cap layer with thickness of around 50nm contributes to the sharp peak around channel 1100. And the platform in the far right centering around channel 1200 originates from the Bi in the AlBiAs layer. Up to 6.6% Bi was incorporated without observable concentration gradient along the growth direction.

Figure 5.18 shows the HRXRD $\omega - 2\theta$ scan on (004) plane from several samples. No clear thickness fringes was observed on any AlBiAs sample. AlBiAs peak is generally broad and have low intensity. For Bi% $\geq$ 6%, there is no AlBiAs peak distinguishable from the background noise. RSM was performed on sample with composition of $AlBi_{0.06}As_{0.94}$, as shown in figure 5.18 with fully strained line(vertical solid black line) drawn. The AlBiAs peak could be vaguely distinguished. However, it seems that the layer is still fully strained to the substrate.

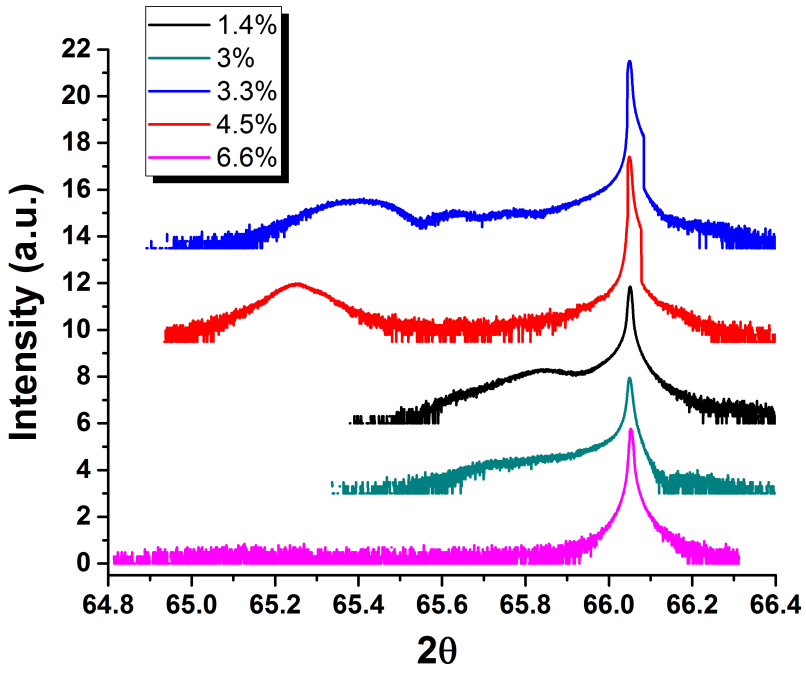

Figure 5.18: HRXRD $\omega - 2\theta$ scans of AlBiAs with different Bi%.

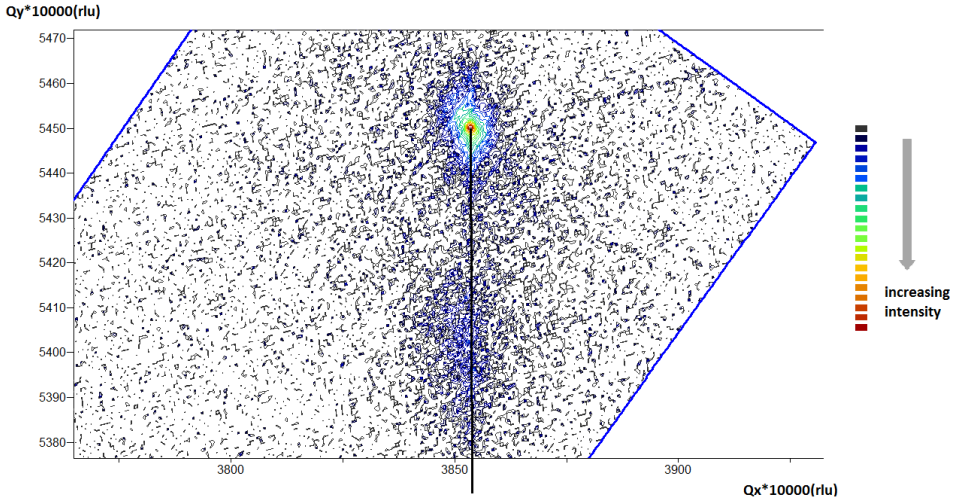

Figure 5.19: Reciprocal space mapping of $AlBi_{0.06}As_{0.94}$in (224) direction, with the vertical black line representing the strained line.

AlBiAs band gap is extracted from spectroscopic ellipsometry measurements. The sample is modeled as 4 layer structure: GaAs substrate + AlBiAs layer + GaAs cap + GaAs oxide. Tabulated optical constants were used for both GaAs and GaAs surface oxide. AlBiAs layer modeled with parametric model based on the AlAs, which is able to describe the AlAs reference sample very well.

The quality of the ellipsometry result seems to depend on the crystalline quality of the sample. The ellipsometry data of the AlAs reference sample grown at 530°C agrees fairly well the the model. However, not all the low temperature grown AlBiAs samples were able to yield sensible ellipsometry result that fit well with the model. Only two samples containing 4.5% and 3.3% Bi% have "good" ellipsometry quality, meaning that the model agrees with the experimental data (The ellipsometry spectrum of the 4.5% sample are shown in figure 5.20). Both samples has clear XRD layer peak as shown in figure 5.18. Whereas the other AlBiAs samples that has a relatively indistinguishable XRD layer peak as shown in the three lower scans in figure 5.18 do not have good ellipsometry scan quality. An example of the "bad" ellipsometry scan is shown in figure 5.21. Growth condition needs to be improved to obtain good quality materials.

The ellipsometry result suggest the $\Gamma - \Gamma$ energy gap of the 4.5% and 3.3% AlBiAs to be 2.70 and 2.77 eV. The band gap reduction is estimated to be around 63 meV/%Bi. Alaya et al.[4] reported theoretical calculation on AlBiAs and predicted $\Gamma - \Gamma$ band gap to be 2.76 and 2.82 eV for 4.5% and 3.3% AlBiAs respectively.

The optical constants of the InAlBiAs, AlBiAs and InGaBiAs are shown in figure 5.23, 5.24 and 5.22.

5.4 Summary

The growth and characterization of Al-containing dilute bismuthides InAlBiAs and AlBiAs were demonstrated in this chapter. Samples were grown by MBE at low temperature and low As_4 overpressure. InAlBiAs thin film on InP substrate contains up to 3.2% Bi%. Valence band anti-crossing theory was applied to describe the band

(a)

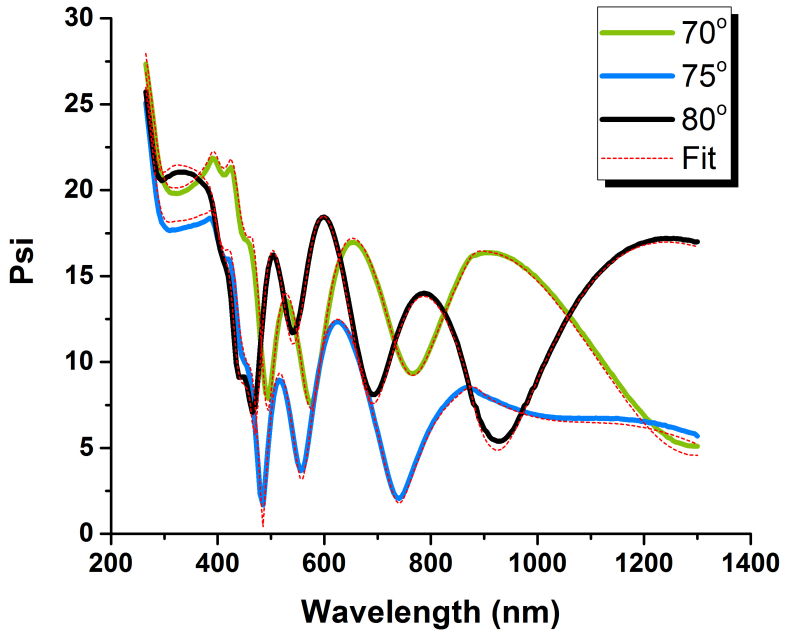

(b)

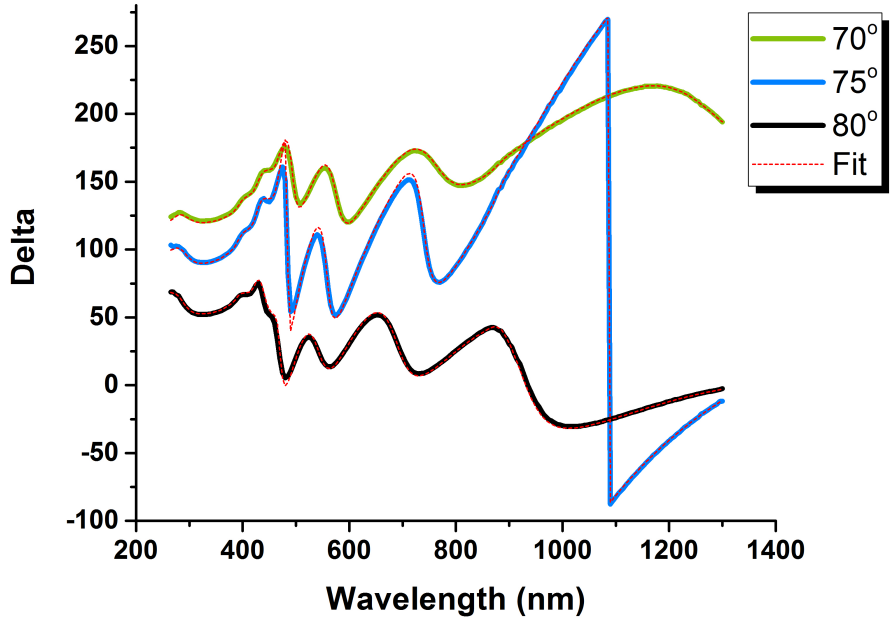

Figure 5.20: $AlBi_{0.045}As_{0.955}$ spectroscopic ellipsometry spectrum: a)Psi, b)Delta. Black, blue and green line are experimental data taken with incident angle of 70°, 75° and 80°. Dashed red line is the model fit.

(a)

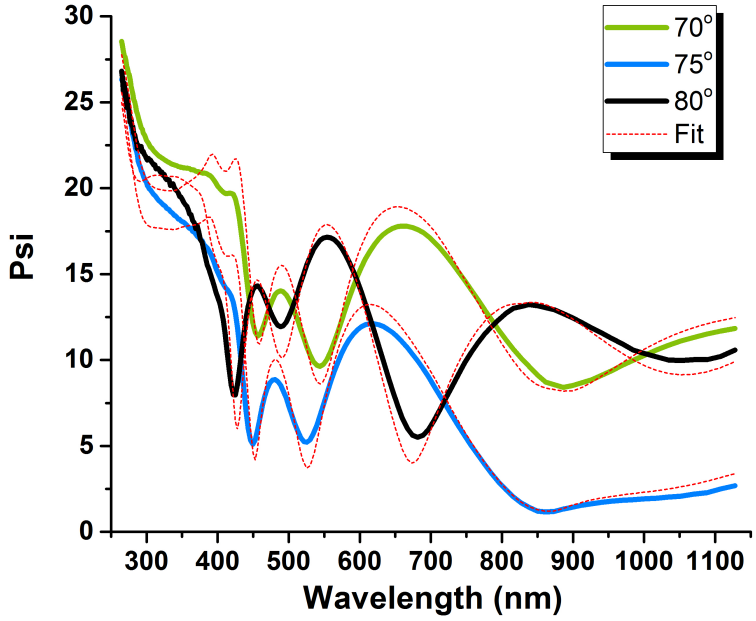

(b)

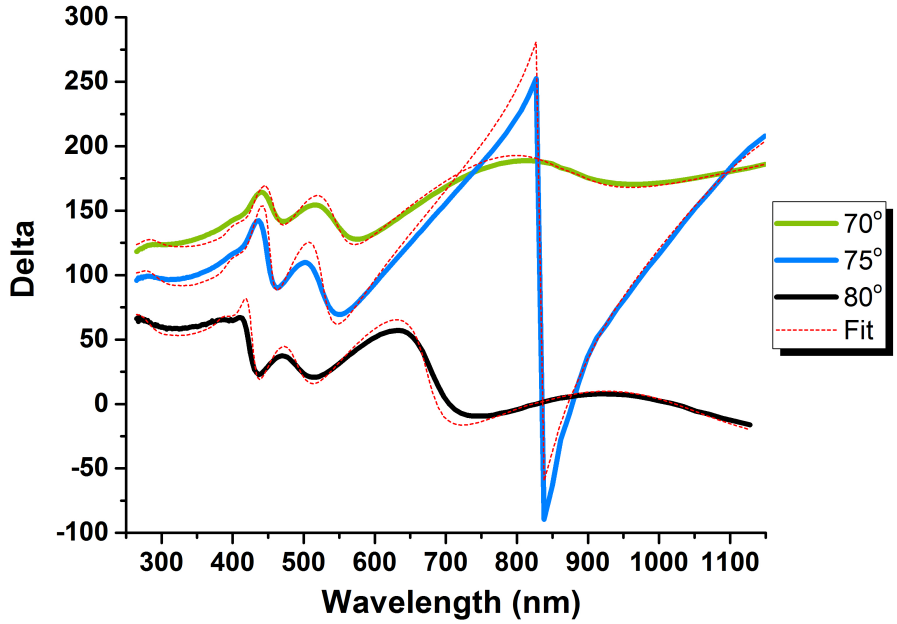

Figure 5.21: Example of spectroscopic ellipsometry spectrum: a)Psi, b)Delta from a AlBiAs sample with poor crystalline quality. Black, blue and green line are experimental data taken with incident angle of 70°, 75° and 80°. Dashed red line is the model fit. The model deviate from the experimental data.

(a)

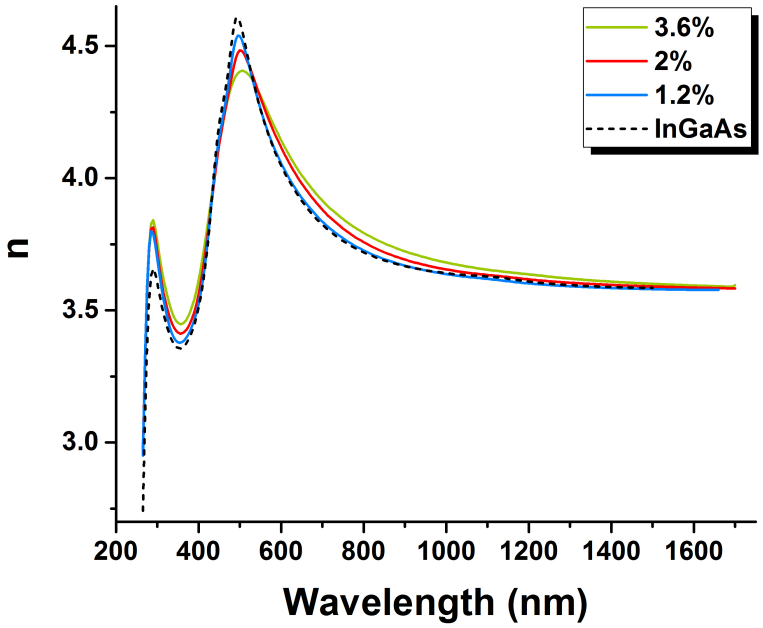

(b)

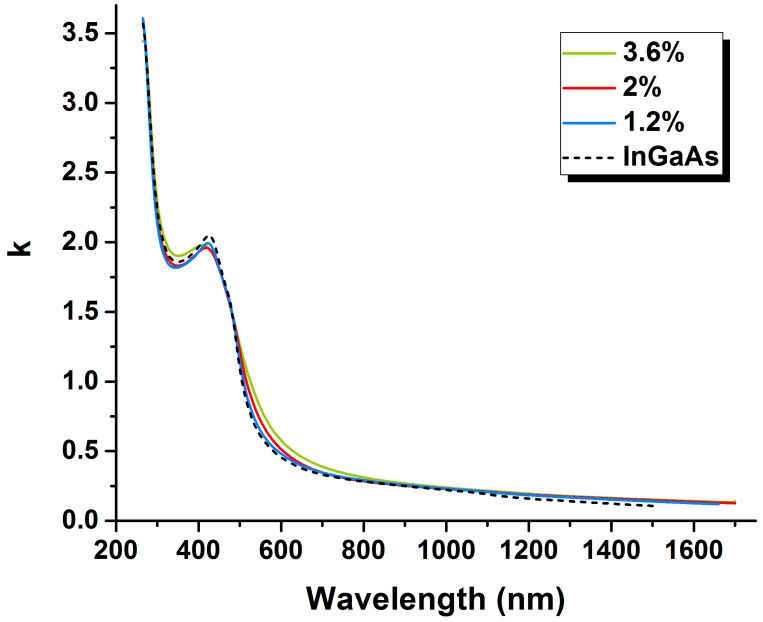

Figure 5.22: Optical constants of InGaBiAs: a) refractive index n; b) extinction coefficient k.

(a)

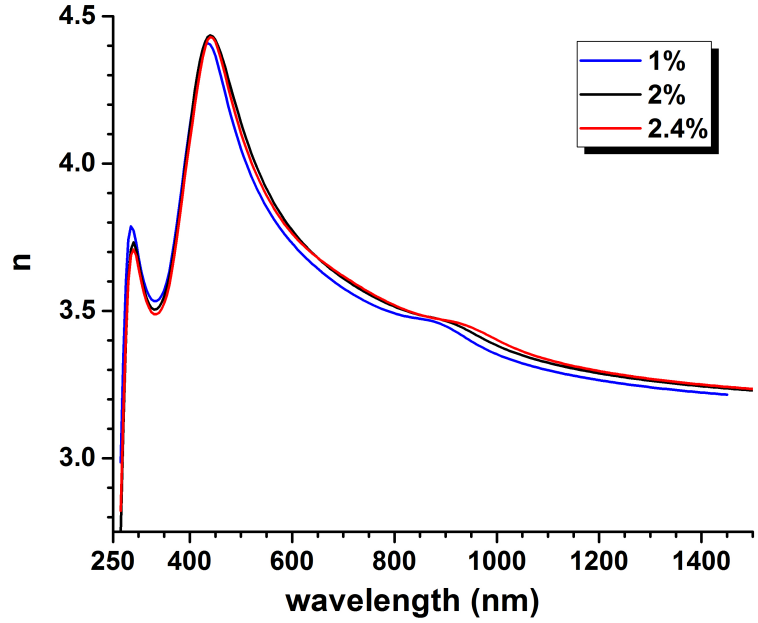

(b)

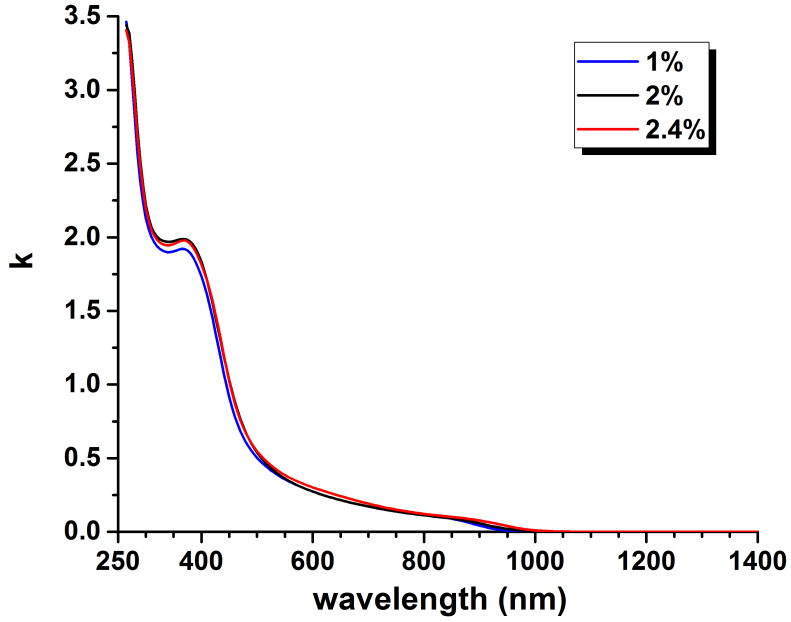

Figure 5.23: Optical constants of $In_{0.54}Al_{0.46}Bi_yAs_{1-y}$: a) refractive index n; b) extinction coefficient k.

(a)

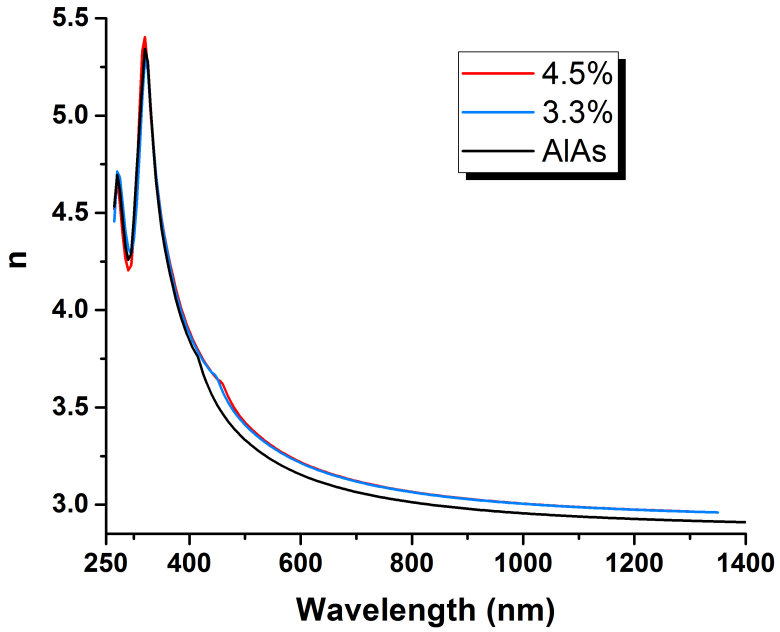

(b)

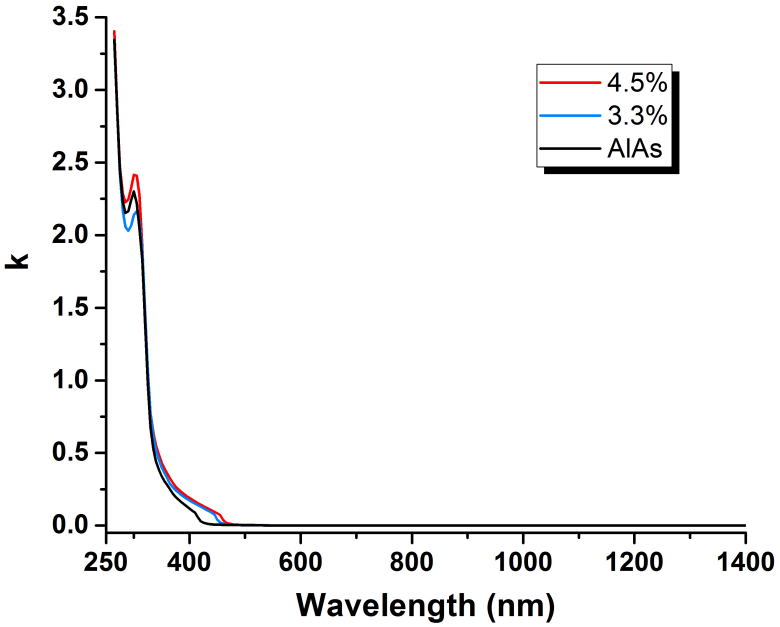

Figure 5.24: Optical constants of $AlBi_yAs_{1-y}$: a) refractive index n; b) extinction coefficient k.

gap change with Bi%. The band gaps determined by spectroscopic ellipsometry agree with the VBAC fairly well up to 2.4% Bi composition in InAlBiAs. Band gap reduction was shown to be around 47 meV/%Bi in this low Bi% range. For the samples with $\geq$ 3% Bi%, the experimentally determined band gaps deviate significantly from the VBAC. This is possibly caused by alloy disorder in the sample containing high Bi% like Bi clusters impacting the valence band strongly which is not captured by the VBAC model used here. Further investigation of the model and optimization of the InAlBiAs quality are needed. AlBiAs with up to 6% Bi% were grown by MBE. We observed around 63 meV/% Bi of band gap reduction. We still need to explore the growth condition at low temperature to obtain good quality thin film for ellipsometry analysis.

Chapter 6

CONCLUSION AND FUTURE WORK

I have discussed the potential performance of the proposed upconversion nanostructure using a kinetic rate equation model and the growth and characterization of Al-containing dilute bismuthides which could be applied to the upconversion nanostructure. The calculation with kinetic rate equation model have shown that the upconversion nanostructure is very promising in converting low energy photons into high energy photons with high upconversion quantum efficiency. The expected solar cell efficiency is also greatly increased with the addition of such upconversion layer.

MBE growth of (In)AlBiAs at low temperature was demonstrated. Good quality InAlBiAs thin films with thickness of several hundred nanometers were achieved. However, AlBiAs growth condition needs to be further explored to improve the material quality. We estimate band gap reduction from Bi incorporation of 47 meV/%Bi and 63 meV%Bi for InAlBiAs and AlBiAs, respectively.

In the next section, I will discuss some of the future directions for dilute bismuthides and upconversion nanostructure.

6.1 Future Work in Dilute Bismuthides and Upconvesion Nanostructure

MBE growth temperature, growth rate and III:V flux ratio's effect on Bi incorporation and crystalline quality of the Al-containing dilute bismuthides need more study for the purpose of achieving better quality films with higher Bi composition.

Temperature plays a very important role in both sample quality and Bi incorporation. Al surface migration is very slow at low temperature, leading to island growth and rough surface. For AlBiAs, low temperature growth under the aforementioned growth condition yield poor crystalline quality film mostly. However, low temperature

growth is essential for Bi incorporation. Finding the balance between crystal quality and growth temperature is even more important for AlBiAs growth. Since the actual growth temperature are unknown for the samples due to the lack of BET temperature control, temperature stability may be another factor that contributes to poor crystalline quality. Previous study on AlGaAs have shown that growing with III: V flux at stoichimetric condition was able to improve the low temperature grown AlGaAs quality[68]. The two samples with 4.5% and 3.3% Bi% that possess best quality of all AlBiAs samples, were grown under As_4 BEP of 4×10^{-6} and 2×10^{-6} respectively. Further lowering the As flux may help improve both the thin film quality and Bi incorporation. However, low As flux would increase the risk of Bi or group III droplets formation on the surface. Modulation techniques like migration enhanced epitaxy is an alternative to improving low temperature growth quality and increase Bi incorporation. By alternating supply of group III (Ga or Al, for example) and group V atoms, the migration of group III atoms is enhanced on group III stabled surface[49, 16]. Alternatively, by periodically interrupting the Bi supply to allow for deplete the surface Bi could potentially prevent Bi droplet formation[87]. Digital alloy of intermixing constituting binaries could be another viable approach. It was reported on GaNSb that alloy produced by this method could maintain high crystallinity at high Sb composition while the alloy still behaves like the bulk crystal in terms of band gap determined by optical absorption [88].

Post-growth rapid thermal annealing is an effective way to improve material quality. It has been demonstrated on GaBiAs that rapid thermal annealing can improve the PL intensity without affecting the peak energy [69]. By performing thermal annealing at various temperature up to 750°C, for 180s, Stanionytė et al., investigated the post growth rapid thermal annealing effect on the $Ga_{0.485}In_{0.515}As_{1-x}Bi_x$ properties and found enhancement in room temperature PL intensity, carrier lifetime, and electron mobility. However, decreased out-of-plane lattice constant has been observed and the InGaBiAs band gap increases tens of meV after annealing. The optimal annealing temperature window is quite narrow. Only annealing over 600°C shows improvement

of the optical and electrical characteristics, while too high a temperature, for example 750°C, strongly degrades the surface[100].

Alloy clustering and phase segregation could occur in the low temperature growth, affecting the electrical and optical properties of the dilute Bismuthides, as evidenced by the ellipsometry results of InAlBiAs and AlBiAs. $CuPt_B$-type of As and Bi atomic ordering and phase segregation was observed in GaBiAs via electron microscopy [76, 13]. S-shape temperature dependence PL peak energy is attributed to Bi-related clustering[66]. Future work on (In)AlBiAs using techniques like high resolution transmission electron microscopy could provide structural information of the alloy and possibly help understanding the results observed in the last chapter.

The first generation epitaxy upconversion nanostructure could use the composition proposed in the figure 5.13 in the low Bi% as high Bi% incorporation is still difficult. We could use this first generation structure to study the energy level offsets and upconversion quantum efficiency with photoluminescence spectroscopy, and dynamics of carrier generation and relaxation with time-resolved PL and transient absorption spectroscopy. The results can be applied to validating the kinetic rate equation model and optimizing the subsequent generations of upconversion nanostructure design.

REFERENCES

[1] *Solar spectral irradiance: Air mass 1.5" in American Society for Testing and Materials (ASTM) Terrestrial Reference Spectra for Photovoltaic Performance Evaluation, 2004, NREL.*

[2] International Energy Agency. Renewables 2017, analysis and forecasts to 2022.

[3] International Energy Agency. World energy outlook 2017.

[4] R. Alaya, M. Mbarki, A. Rebey, and A.V. Postnikov. Ab initio predictions of structure preferences and band gap character in ordered $AlAs_{1-x}Bi_x$ alloys. *Current Applied Physics*, 16(3):288 – 293, 2016.

[5] K. Alberi, J. Wu, W. Walukiewicz, K. M. Yu, O. D. Dubon, S. P. Watkins, C. X. Wang, X. Liu, Y.-J. Cho, and J. Furdyna. Valence-band anticrossing in mismatched III-V semiconductor alloys. *Phys. Rev. B*, 75:045203, Jan 2007.

[6] Zotov Andrey V. and Saranin Alexander A. www.rusnano.com.

[7] Shigeo Asahi, Kazuki Kusaki, Yukihiro Harada, and Takashi Kita. Increasing conversion efficiency of two-step photon up-conversion solar cell with a voltage booster hetero-interface. *Scientific Reports*, 8(1):872, 2018.

[8] Shigeo Asahi, Haruyuki Teranishi, Kazuki Kusaki, Toshiyuki Kaizu, and Takashi Kita. Two-step photon up-conversion solar cells. *Nature Communications*, 8:14962, Apr 2017.

[9] Ashwin C. Atre and Jennifer A. Dionne. Realistic upconverter-enhanced solar cells with non-ideal absorption and recombination efficiencies. *Journal of Applied Physics*, 110(3):034505, 2011.

[10] Stanislav Baluschev, Vladimir Yakutkin, Tzenka Miteva, Yuri Avlasevich, Sergei Chernov, Sergei Aleshchenkov, Gabriele Nelles, Andrei Cheprakov, Akio Yasuda, Klaus Müllen, and Gerhard Wegner. Blue-Green Up-Conversion: Noncoherent Excitation by NIR Light. *Angewandte Chemie International Edition*, 46(40):7693–7696, 2007.

[11] F. Bastiman, A.R.B. Mohmad, J.S. Ng, J.P.R David, and S.J. Sweeney. Non-stoichiometric GaAsBi/GaAs (100) molecular beam epitaxy growth. *Journal of Crystal Growth*, 338(1):57 – 61, 2012.

[12] Wolfgang Bennarndt, Gerhard Boehm, and Markus-Christian Amann. Domains of molecular beam epitaxial growth of Ga(In)AsBi on GaAs and InP substrates. *Journal of Crystal Growth*, 436:56 – 61, 2016.

[13] Andreas Beyer, Nikolai Knaub, Phil Rosenow, Kakhaber Jandieri, Peter Ludewig, Lars Bannow, Stephan W. Koch, Ralf Tonner, and Kerstin Volz. Local Bi ordering in MOVPE grown Ga(As,Bi) investigated by high resolution scanning transmission electron microscopy. *Applied Materials Today*, 6:22 – 28, 2017.

[14] Justin A. Briggs, Ashwin C. Atre, and Jennifer A. Dionne. Narrow-bandwidth solar upconversion: Case studies of existing systems and generalized fundamental limits. *Journal of Applied Physics*, 113(12):124509, 2013.

[15] C. A. Broderick, W. Xiong, S. J. Sweeney, E. P. O'Reilly, and J. M. Rorison. Dilute bismide alloys grown on gaas and inp substrates for improved near- and mid-infrared semiconductor lasers. In *2016 18th International Conference on Transparent Optical Networks (ICTON)*, pages 1–4, July 2016.

[16] Renata Butkutė, Karolis Stašys, Vaidas Pačebutas, Bronislovas Čechavičius, Rokas Kondrotas, Andrejus Geižutis, and Arūnas Krotkus. Bismuth quantum dots and strong infrared photoluminescence in migration-enhanced epitaxy grown GaAsBi-based structures. *Optical and Quantum Electronics*, 47(4):873–882, Apr 2015.

[17] Public Domain By Acarlso3 at English Wikipedia Transferred from en.wikipedia to Commons.

[18] from Wikimedia Commons By Wiso [CC BY-SA 3.0 (https://creativecommons.org/licenses/by sa/3.0)].

[19] Grace M T Chai, C A Broderick, E P O'Reilly, Z Othaman, S R Jin, J P Petropoulos, Y Zhong, P B Dongmo, J M O Zide, S J Sweeney, and T J C Hosea. Experimental and modelling study of InGaBiAs/InP alloys with up to 5.8% Bi, and with $\Delta_{SO} > E_g$. *Semiconductor Science and Technology*, 30(9):094015, 2015.

[20] Wen-Hao Chang, Yu-An Liao, Wei-Ting Hsu, Ming-Chih Lee, Pei-Chin Chiu, and Jen-Inn Chyi. Carrier dynamics of type-II InAs⁄GaAs quantum dots covered by a thin GaAs1−xSbx layer. *Applied Physics Letters*, 93(3), 2008.

[21] Eric Y Chen, Jing Zhang, Diane G Sellers, Yujun Zhong, Joshua M O Zide, and Matthew F Doty. A Kinetic Rate Model of Novel Upconversion Nanostructures for High- Efficiency Photovoltaics. *IEEE Journal of Photovoltaics*, 6(5):1–3, 2016.

[22] Xiren Chen, Xiaoyan Wu, Li Yue, Liangqing Zhu, Wenwu Pan, Zhen Qi, Shumin Wang, and Jun Shao. Negative thermal quenching of below-bandgap photoluminescence in InPBi. *Applied Physics Letters*, 110(5):051903, 2017.

[23] Yuen Yap Cheng, Burkhard Fuckel, Rowan W. MacQueen, Tony Khoury, Raphael G. C. R. Clady, Tim F. Schulze, N. J. Ekins-Daukes, Maxwell J. Crossley, Bernd Stannowski, Klaus Lips, and Timothy W. Schmidt. Improving the light-harvesting of amorphous silicon solar cells with photochemical upconversion. *Energy Environ. Sci.*, 5:6953–6959, 2012.

[24] Yuen Yap Cheng, Tony Khoury, Raphaël G. C. R. Clady, Murad J. Y. Tayebjee, N. J. Ekins-Daukes, Maxwell J. Crossley, and Timothy W. Schmidt. On the efficiency limit of triplet–triplet annihilation for photochemical upconversion. *Phys. Chem. Chem. Phys.*, 12:66–71, 2010.

[25] Hyeonsik M. Cheong, Brian Fluegel, Mark C. Hanna, and Angelo Mascarenhas. Photoluminescence up-conversion in GaAs/$Al_xGa_{1-x}As$ heterostructures. *Phys. Rev. B*, 58:R4254–R4257, Aug 1998.

[26] Gavin Conibeer. Third-generation photovoltaics. *Materials Today*, 10(11):42 – 50, 2007.

[27] O. J. Curtin, M. Yoshida, A. Pusch, N. P. Hylton, N. J. Ekins-Daukes, C. C. Phillips, and O. Hess. Quantum cascade photon ratchets for intermediate-band solar cells. *IEEE Journal of Photovoltaics*, 6(3):673–678, May 2016.

[28] Zhang X. D., Jin X., Wang D. F., Xiong S. Z., Geng X. H., and Zhao Y. Synthesis of NaYF4: Yb, Er nanocrystals and its application in silicon thin film solar cells. *physica status solidi c*, 7(3-4):1128–1131, 2010.

[29] E. C. F. da Silva. InxAl1-xAs: critical point energies: Datasheet from Landolt-Börnstein - Group III Condensed Matter · Volume 44E: "New Data and Updates for several III-V (including mixed crystals) and II-VI Compounds" in SpringerMaterials Copyright 2012 Springer-Verlag Berlin Heidelberg.

[30] Matthew V. DaCosta, Samer Doughan, Yi Han, and Ulrich J. Krull. Lanthanide upconversion nanoparticles and applications in bioassays and bioimaging: A review. *Analytica Chimica Acta*, 832:1 – 33, 2014.

[31] J. de Wild, J.K. Rath, A. Meijerink, W.G.J.H.M. van Sark, and R.E.I. Schropp. Enhanced near-infrared response of a-Si:H solar cells with β-$NaYF_4$:Yb^{3+} (18%), Er3+ (2%) upconversion phosphors. *Solar Energy Materials and Solar Cells*, 94(12):2395 – 2398, 2010.

[32] Zvicka Deutsch, Lior Neeman, and Dan Oron. Luminescence upconversion in colloidal double quantum dots. *Nature Nanotechnology*, 8:649 EP –, Aug 2013.

[33] Zvicka Deutsch, Osip Schwartz, Ron Tenne, Ronit Popovitz-Biro, and Dan Oron. Two-color antibunching from band-gap engineered colloidal semiconductor nanocrystals. *Nano Letters*, 12(6):2948–2952, 2012. PMID: 22533783.

[34] Gan Feng, Kunishige Oe, and Masahiro Yoshimoto. Temperature dependence of Bi behavior in MBE growth of InGaAs/InP. *Journal of Crystal Growth*, 301-302:121 – 124, 2007. 14th International Conference on Molecular Beam Epitaxy.

[35] Gan Feng, Masahiro Yoshimoto, Kunishige Oe, Akiyoshi Chayahara, and Yuji Horino. New III–V Semiconductor InGaAsBi Alloy Grown by Molecular Beam Epitaxy. *Japanese Journal of Applied Physics*, 44(9L):L1161, 2005.

[36] Stefan Fischer, Rosa Martín-Rodríguez, Benjamin Fröhlich, Karl W. Krämer, Andries Meijerink, and Jan Christoph Goldschmidt. Upconversion quantum yield of Er^{3+}-doped β-$NaYF_4$ and Gd_2O_2S: The effects of host lattice, Er^{3+} doping, and excitation spectrum bandwidth. *Journal of Luminescence*, 153(Supplement C):281 – 287, 2014.

[37] S. Franchi, G. Trevisi, L. Seravalli, and P. Frigeri. Quantum dot nanostructures and molecular beam epitaxy. *Progress in Crystal Growth and Characterization of Materials*, 47(2):166 – 195, 2003. Vapour Growth of Bulk Crystals and Epitaxy: Part I.

[38] S. Francoeur, M.-J. Seong, A. Mascarenhas, S. Tixier, M. Adamcyk, and T. Tiedje. Band gap of GaAs1−xBix, 0<x<3.6%. *Applied Physics Letters*, 82(22):3874–3876, 2003.

[39] Pierre Gibart, François Auzel, Jean-Claude Guillaume, and Khaled Zahraman. Below Band-Gap IR Response of Substrate-Free GaAs Solar Cells Using Two-Photon Up-Conversion. *Japanese Journal of Applied Physics*, 35(8R):4401, 1996.

[40] National Renewable Energy Laboratory Golden Co. Best research cell efficiency.

[41] Jan Christoph Goldschmidt and Stefan Fischer. Upconversion for photovoltaics – a review of materials, devices and concepts for performance enhancement. *Advanced Optical Materials*, 3(4):510–535, 2015.

[42] Y. Gu, Y. G. Zhang, X. Y. Chen, Y. J. Ma, S. P. Xi, B. Du, and Hsby. Li. Nearly lattice-matched short-wave infrared InGaAsBi detectors on InP. *Applied Physics Letters*, 108(3):032102, 2016.

[43] S. Gupta, P. K. Bhattacharya, J. Pamulapati, and G. Mourou. Optical properties of high-quality InGaAs/InAlAs multiple quantum wells. *Journal of Applied Physics*, 69(5):3219, 1991.

[44] Anna L. Hagstrom, Fan Deng, and Jae-Hong Kim. Enhanced triplet–triplet annihilation upconversion in dual-sensitizer systems: Translating broadband light absorption to practical solid-state materials. *ACS Photonics*, 4(1):127–137, 2017.

[45] Shuji Hasegawa. *Reflection High-Energy Electron Diffraction*, pages 1–14. American Cancer Society, 2012.

[46] C. H. Henry. Limiting efficiencies of ideal single and multiple energy gap terrestrial solar cells. *Journal of Applied Physics*, 51(8):4494–4500, 1980.

[47] Craig M. Herzinger and Blaine D. Johs. Dielectric function parametric model, and method of use, us patent us5796983a, 08 1995.

[48] Ch Heyn, Ch Strelow, and W Hansen. Excitonic lifetimes in single GaAs quantum dots fabricated by local droplet etching. *New Journal of Physics*, 14(5):053004, May 2012.

[49] Yoshiji Horikoshi, Minoru Kawashima, and Hiroshi Yamaguchi. Migration-Enhanced Epitaxy of GaAs and AlGaAs. *Japanese Journal of Applied Physics*, 27(2R):169, 1988.

[50] N. P. Hylton, T. F. Hinrichsen, A. R. Vaquero-Stainer, M. Yoshida, A. Pusch, M. Hopkinson, O. Hess, C. C. Phillips, and N. J. Ekins-Daukes. Photoluminescence upconversion at GaAs/$InGaP_2$ interfaces driven by a sequential two-photon absorption mechanism. *Phys. Rev. B*, 93:235303, Jun 2016.

[51] Angelo Monguzzi Jacopo Pedrini. Recent advances in the application triplet–triplet annihilation-based photon upconversion systems to solar technologies. *Journal of Photonics for Energy*, 8:8 – 8 – 16, 2017.

[52] Inc J.A.Woollam Co. Guide to using WVASE32 ®.

[53] Rajeev N Kini and Angelo Mascarenhas. Effect of Bismuth Alloying on the Transport Properties of the Dilute Bismide Alloy, $GaAs_{1-x}Bi_x$. In *Bismuth-Containing Compounds*, pages 181–200. Springer, 2013.

[54] R. Kudrawiec, J. Kopaczek, J. Misiewicz, J. P. Petropoulos, Y. Zhong, and J. M. O. Zide. Contactless electroreflectance study of E_0 and $E_0 + \Delta_{SO}$ transitions in $In_{0.53}Ga_{0.47}Bi_xAs_{1-x}$ alloys. *Applied Physics Letters*, 99(25):251906, 2011.

[55] P T Landsberg and P Baruch. The thermodynamics of the conversion of radiation energy for photovoltaics. *Journal of Physics A: Mathematical and General*, 22:1911–1926, 1999.

[56] R. B. Lewis, M. Masnadi-Shirazi, and T. Tiedje. Growth of high Bi concentration $GaAs_{1-x}Bi_x$ by molecular beam epitaxy. *Applied Physics Letters*, 101(8):082112, 2012.

[57] Chuanhao Li, Christopher Koenigsmann, Fan Deng, Anna Hagstrom, Charles A. Schmuttenmaer, and Jae-Hong Kim. Photocurrent enhancement from solid-state triplet–triplet annihilation upconversion of low-intensity, low-energy photons. *ACS Photonics*, 3(5):784–790, 2016.

[58] Liangliang Liang, Yumin Liu, and Xing-Zhong Zhao. Double-shell β-$NaYF_4$:Yb^{3+}, Er^{3+}/SiO_2/TiO_2 submicroplates as a scattering and upconverting layer for efficient dye-sensitized solar cells. *Chem. Commun.*, 49:3958–3960, 2013.

[59] Antonio Luque and Antonio Martí. Increasing the efficiency of ideal solar cells by photon induced transitions at intermediate levels. *Phys. Rev. Lett.*, 78:5014–5017, Jun 1997.

[60] Antonio Luque, Antonio Martí, and Colin Stanley. Understanding intermediate-band solar cells. *Nature Photonics*, 6:146 EP –, Feb 2012.

[61] Melika Mahboub, Zhiyuan Huang, and Ming Lee Tang. Efficient infrared-to-visible upconversion with subsolar irradiance. *Nano Letters*, 16(11):7169–7175, 2016. PMID: 27788577.

[62] Melika Mahboub, Pan Xia, Jeremiah Van Baren, Xin Li, Chun Hung Lui, and Ming Lee Tang. Midgap States in PbS Quantum Dots Induced by Cd and Zn Enhance Photon Upconversion. *ACS Energy Letters*, 3(4):767–772, 2018.

[63] O. Maksimov, Y. Gong, H. Du, P. Fisher, M. Skowronski, I.L. Kuskovsky, and V.D. Heydemann. Structural and optical properties of GaN films grown on GaAs substrates by molecular beam epitaxy. *Vacuum*, 80(9):1042 – 1045, 2006.

[64] I. P. Marko, Z. Batool, K. Hild, S. R. Jin, N. Hossain, T. J. C. Hosea, J. P. Petropoulos, Y. Zhong, P. B. Dongmo, J. M. O. Zide, and S. J. Sweeney. Temperature and Bi-concentration dependence of the bandgap and spin-orbit splitting in InGaBiAs/InP semiconductors for mid-infrared applications. *Applied Physics Letters*, 101(22):221108, 2012.

[65] A. Markus, A. Fiore, J. D. Ganière, U. Oesterle, J. X. Chen, B. Deveaud, M. Ilegems, and H. Riechert. Comparison of radiative properties of InAs quantum dots and GaInNAs quantum wells emitting around 1.3 μm. *Applied Physics Letters*, 80(6):911, 2002.

[66] Simone Mazzucato, Henri Lehec, Helene Carrère, Hajer Makhloufi, Alexandre Arnoult, Chantal Fontaine, Thierry Amand, and Xavier Marie. Low-temperature photoluminescence study of exciton recombination in bulk GaAsBi. *Nanoscale Research Letters*, 9(1):19, Jan 2014.

[67] V A Milichko, A S Shalin, I S Mukhin, A E Kovrov, A A Krasilin, A V Vinogradov, P A Belov, and C R Simovski. Solar photovoltaics: current state and trends. *Physics-Uspekhi*, 59(8):727, 2016.

[68] M. Missous. Stoichiometric low-temperature GaAs and AlGaAs: A reflection high-energy electron-diffraction study. *Journal of Applied Physics*, 78(7):4467–4471, 1995.

[69] A. R. Mohmad, F. Bastiman, C. J. Hunter, R. Richards, S. J. Sweeney, J. S. Ng, and J. P. R. David. Effects of rapid thermal annealing on $GaAs_{1-x}Bi_x$ alloys. *Applied Physics Letters*, 101(1):012106, 2012.

[70] Cédric Mongin, Sofia Garakyaraghi, Natalia Razgoniaeva, Mikhail Zamkov, and Felix N. Castellano. Direct observation of triplet energy transfer from semiconductor nanocrystals. *Science*, 351(6271):369–372, 2016.

[71] Angelo Monguzzi, Sergey M. Borisov, Jacopo Pedrini, Ingo Klimant, Mario Salvalaggio, Paolo Biagini, Fabio Melchiorre, Camilla Lelii, and Francesco Meinardi. Efficient broadband triplet–triplet annihilation-assisted photon upconversion at subsolar irradiance in fully organic systems. *Advanced Functional Materials*, 25(35):5617–5624.

[72] L. Nattermann, P. Ludewig, E. Sterzer, and K. Volz. Exploiting strain to enhance the Bi incorporation in GaAs-based III/V semiconductors using MOVPE. *Journal of Crystal Growth*, 470:15 – 19, 2017.

[73] Ncouniot. By Ncouniot (Fraunhofer Institute for Solar Energy Systems) [CC BY-SA 3.0 (https://creativecommons.org/licenses/by-sa/3.0) or GFDL (http://www.gnu.org/copyleft/fdl.html)], via Wikimedia Commons, https://commons.wikimedia.org/wiki/File:StructureMJetspectre.png.

[74] Antonia Neels. High Resolution X-ray Diffraction, CSEM XRD Application LAB.

[75] Kazutaka Nishikawa, Yasuhiko Takeda, Ken-ichi Yamanaka, Tomoyoshi Motohiro, Daisuke Sato, Junya Ota, Naoya Miyashita, and Yoshitaka Okada. Over 100 ns intrinsic radiative recombination lifetime in type II $InAs/GaAs_{1-x}Sb_x$ quantum dots. *Journal of Applied Physics*, 111(4), 2012.

[76] Andrew G. Norman, Ryan France, and Aaron J. Ptak. Atomic ordering and phase separation in MBE $GaAs_{1-x}Bi_x$. *Journal of Vacuum Science & Technology B*, 29(3):03C121, 2011.

[77] Taku Ogawa, Nobuhiro Yanai, Angelo Monguzzi, and Nobuo Kimizuka. Highly efficient photon upconversion in self-assembled light-harvesting molecular systems. *Scientific Reports*, 5:10882 EP –, Jun 2015. Article.

[78] S W Osborne, P Blood, P M Smowton, Y C Xin, a Stintz, D Huffaker, and L F Lester. Optical absorption cross section of quantum dots. *Journal of Physics: Condensed Matter*, 16(35):S3749–S3756, September 2004.

[79] Plamen P. Paskov, Per-Olof Holtz, Bo Monemar, Jorge M. Garcia, Winston V. Schoenfeld, and Pierre M. Petroff. Optical Up-Conversion Processes in InAs Quantum Dots. *Japanese Journal of Applied Physics*, 40(3S):2080, 2001.

[80] J. P. Petropoulos, Y. Zhong, and J. M. O. Zide. Optical and electrical characterization of InGaBiAs for use as a mid-infrared optoelectronic material. *Applied Physics Letters*, 99(3):031110, 2011.

[81] PVEducation. https://pveducation.org/pvcdrom/solar-cell-structure.

[82] M. K. Rajpalke, W. M. Linhart, K. M. Yu, M. Birkett, J. Alaria, J. J. Bomphrey, S. Sallis, L. F. J. Piper, T. S. Jones, M. J. Ashwin, and T. D. Veal. Bi-induced band gap reduction in epitaxial InSbBi alloys. *Applied Physics Letters*, 105(21):212101, 2014.

[83] S Raymond, S Fafard, P. J. Poole, A. Wojs, P Hawrylak, S Charbonneau, D Leonard, R Leon, Pm Petroff, and Jl Merz. State filling and time-resolved photoluminescence of excited states in $In_xGa_{1-x}As$/GaAs self-assembled quantum dots. *Physical Review. B: Condensed Matter*, 54(16):11548–11554, October 1996.

[84] S. H. Rhim, Miyoung Kim, A. J. Freeman, and Ryoji Asahi. Fully first-principles screened-exchange LDA calculations of excited states and optical properties of III-V semiconductors. *Phys. Rev. B*, 71:045202, Jan 2005.

[85] B. S. Richards and A. Shalav. Enhancing the near-infrared spectral response of silicon optoelectronic devices via up-conversion. *IEEE Transactions on Electron Devices*, 54(10):2679–2684, Oct 2007.

[86] Robert D. Richards, Faebian Bastiman, Christopher J. Hunter, Danuta F. Mendes, Abdul R. Mohmad, John S. Roberts, and John P.R. David. Molecular beam epitaxy growth of GaAsBi using As_2 and As_4. *Journal of Crystal Growth*, 390:120 – 124, 2014.

[87] I. C. Sandall, F. Bastiman, B. White, R. Richards, D. Mendes, J. P. R. David, and C. H. Tan. Demonstration of InAsBi photoresponse beyond 3.5 μm. *Applied Physics Letters*, 104(17):171109, 2014.

[88] Wendy L. Sarney, Stefan P. Svensson, Min Ting, Natalie Segercrantz, Wladek Walukiewicz, Kin Man Yu, Robert W. Martin, Sergei V. Novikov, and C. T. Foxon. Intermixing studies in $GaN_{1-x}Sb_x$ highly mismatched alloys. *Appl. Opt.*, 56(3):B64–B69, Jan 2017.

[89] S Sauvage, P Boucaud, T Brunhes, V Immer, E Finkman, and J-M Gerard. Mid-infrared absorption and photocurrent spectroscopy of InAs/GaAs self-assembled quantum dots. *Applied Physics Letters*, 78(16):2327–2329, 2001.

[90] Richard Scheps. Upconversion laser processes. *Progress in Quantum Electronics*, 20(4):271 – 358, 1996.

[91] Tim F. Schulze, Jens Czolk, Yuen-Yap Cheng, Burkhard Fückel, Rowan W. MacQueen, Tony Khoury, Maxwell J. Crossley, Bernd Stannowski, Klaus Lips, Uli Lemmer, Alexander Colsmann, and Timothy W. Schmidt. Efficiency enhancement of organic and thin-film silicon solar cells with photochemical upconversion. *The Journal of Physical Chemistry C*, 116(43):22794–22801, 2012.

[92] D. G. Sellers, S. J. Polly, Y. Zhong, S. M. Hubbard, J. M. O. Zide, and M. F. Doty. New nanostructured materials for efficient photon upconversion. *IEEE Journal of Photovoltaics*, 5(1):224–228, Jan 2015.

[93] Diane G. Sellers, Jing Zhang, Eric Y. Chen, Yujun Zhong, Matthew F. Doty, and Joshua M O Zide. Novel nanostructures for efficient photon upconversion and high-efficiency photovoltaics. *Solar Energy Materials and Solar Cells*, 155:446–453, 2016.

[94] T. S. Shamirzaev, A. M. Gilinsky, A. I. Toropov, A. K. Bakarov, D. A. Tenne, K.S Zhuravlev, C von Borczyskowski, and D.R.T Zahn. Millisecond fluorescence in InAs quantum dots embedded in AlAs. *Physica E: Low-dimensional Systems and Nanostructures*, 20(3-4):282–285, January 2004.

[95] W. Shan, W. Walukiewicz, J. W. Ager, E. E. Haller, J. F. Geisz, D. J. Friedman, J. M. Olson, and S. R. Kurtz. Band Anticrossing in GaInNAs Alloys. *Phys. Rev. Lett.*, 82:1221–1224, Feb 1999.

[96] Yunfei Shang, Shuwei Hao, Chunhui Yang, and Guanying Chen. Enhancing solar cell efficiency using photon upconversion materials. *Nanomaterials*, 5(4):1782–1809, 2015.

[97] William Shockley and Hans J. Queisser. Detailed balance limit of efficiency of p-n junction solar cells. *Journal of Applied Physics*, 32(3):510–519, 1961.

[98] Yoan C. Simon and Christoph Weder. Low-power photon upconversion through triplet–triplet annihilation in polymers. *Journal of Materials Chemistry*, 22(39):20817–20830, 2012.

[99] Scott A Speakman, MIT Center for Materials Science, and Engineering. Introduction to High Resolution X-Ray Diffraction of Epitaxial Thin Films, Lecture slides.

[100] S. Stanionytė, V. Pačebutas, B. Čechavičius, A. Bičiūnas, A. Geižutis, V. Bukauskas, R. Butkutė, and A. Krotkus. Impact of thermal treatments on epitaxial $Ga_yIn_{1-y}As_{1-x}Bi_x$ layers luminescent properties. *Journal of Materials Science*, 53(11):8339–8346, Jun 2018.

[101] Kitamura T., Ohtsubo R., Murayama M., Kuroda T., Yamaguchi K., and Tackeuchi A. Direct observation of phonon relaxation bottleneck in InAs quantum dots of high-uniformity. *physica status solidi (c)*, 0(4):1165–1168, 2003.

[102] Ayelet Teitelboim and Dan Oron. Broadband near-infrared to visible upconversion in quantum dot–quantum well heterostructures. *ACS Nano*, 10(1):446–452, 2016.

[103] David M. Tex and Itaru Kamiya. Upconversion of infrared photons to visible luminescence using InAs-based quantum structures. *Phys. Rev. B*, 83:081309, Feb 2011.

[104] T Thomas, A Mellor, N P Hylton, M Führer, D Alonso-Álvarez, A Braun, N J Ekins-Daukes, J P R David, and S J Sweeney. Requirements for a GaAsBi 1 eV sub-cell in a GaAs-based multi-junction solar cell. *Semiconductor Science and Technology*, 30(9):094010, 2015.

[105] T.N.D. Tibbits, P. Beutel, M. Grave, C. Karcher, E. Oliva, G. Siefer, A. Wekkeli, M. Schachtner, F. Dimroth, A.W. Bett, R. Krause, M. Piccin, N. Blanc, M. Muñoz-Rico, C. Arena, E. Guiot, C. Charles-Alfred, C. Drazek, F. Janin, L. Farrugia, B. Hoarau, J. Wasselin, A. Tauzin, T. Signamarcheix, T. Hannappel, K. Schwarzburg, and A. Dobrich. New efficiency frontiers with wafer-bonded multi-junction solar cells. *29th European Photovoltaic Solar Energy Conference and Exhibition, Amsterdam, Netherlands*, September 2014.

[106] L. Töben, L. Gundlach, R. Ernstorfer, R. Eichberger, T. Hannappel, F. Willig, A. Zeiser, J. Förstner, A. Knorr, P. H. Hahn, and W. G. Schmidt. Femtosecond Transfer Dynamics of Photogenerated Electrons at a Surface Resonance of Reconstructed InP(100). *Phys. Rev. Lett.*, 94:067601, Feb 2005.

[107] T. Trupke, M. A. Green, and P. Würfel. Improving solar cell efficiencies by upconversion of sub-band-gap light. *Journal of Applied Physics*, 92(7):4117–4122, 2002.

[108] J. Urayama, T. B. Norris, J. Singh, and P. Bhattacharya. Observation of phonon bottleneck in quantum dot electronic relaxation. *Phys. Rev. Lett.*, 86:4930–4933, May 2001.

[109] Muhammad Usman, Christopher A. Broderick, Andrew Lindsay, and Eoin P. O'Reilly. Tight-binding analysis of the electronic structure of dilute bismide alloys of GaP and GaAs. *Phys. Rev. B*, 84:245202, Dec 2011.

[110] A De Vos. Detailed balance limit of the efficiency of tandem solar cells. *Journal of Physics D: Applied Physics*, 13(5):839, 1980.

[111] Chao Wang, Liang Cheng, and Zhuang Liu. Upconversion nanoparticles for photodynamic therapy and other cancer therapeutics. *Theranostics*, 3(5):317–330, Mar 2013. thnov03p0317[PII].

[112] Feng Wang and Xiaogang Liu. Recent advances in the chemistry of lanthanide-doped upconversion nanocrystals. *Chemical Society Reviews*, 38(4):976, 2009.

[113] Weiming Wang, Albert S. Lin, and Jamie D. Phillips. Intermediate-band photovoltaic solar cell based on ZnTe:O. *Applied Physics Letters*, 95(1):011103, 2009.

[114] Xindong Wang, Rashid R. Valiev, Tymish Y. Ohulchanskyy, Hans Agren, Chunhui Yang, and Guanying Chen. Dye-sensitized lanthanide-doped upconversion nanoparticles. *Chem. Soc. Rev.*, 46:4150–4167, 2017.

[115] Shao Wei, Chen Guanying, Ohulchanskyy Tymish Y., Kuzmin Andrey, Damasco Jossana, Qiu Hailong, Yang Chunhui, Ågren Hans, and Prasad Paras N. Lanthanide-doped fluoride core/multishell nanoparticles for broadband upconversion of infrared light. *Advanced Optical Materials*, 3(4):575–582, 2015.

[116] Junichi Yoshida, Takashi Kita, Osamu Wada, and Kunishige Oe. Temperature dependence of $GaAs_{1-x}Bi_x$ band gap studied by photoreflectance spectroscopy. *Japanese journal of applied physics*, 42(2R):371, 2003.

[117] Junichi Yoshida, Takashi Kita, Osamu Wada, and Kunishige Oe. Temperature dependence of $GaAs_{1-x}Bi_x$ band gap studied by photoreflectance spectroscopy. *Japanese Journal of Applied Physics*, 42(2R):371, 2003.

[118] M. Yoshida, N. J. Ekins-Daukes, D. J. Farrell, and C. C. Phillips. Photon ratchet intermediate band solar cells. *Applied Physics Letters*, 100(26):263902, 2012.

[119] Y. Zhong, P. B. Dongmo, J. P. Petropoulos, and J. M. O. Zide. Effects of molecular beam epitaxy growth conditions on composition and optical properties of $In_xGa_{1-x}Bi_yAs_{1-y}$. *Applied Physics Letters*, 100(11):112110, 2012.

[120] Yujun Zhong, Pernell Dongmo, and Joshua Zide. *Dilute Bismuthides on an InP Platform*, pages 89–116. Springer New York, New York, NY, 2013.

[121] Shuxing Zhou, Ming Qi, Likun Ai, Shumin Wang, Anhuai Xu, and Qi Guo. Growth and electrical properties of high-quality InGaAsBi thin films using gas source molecular beam epitaxy. *Japanese Journal of Applied Physics*, 56(3):035505, 2017.

Appendix

COPYRIGHT PERMISSION

For contents in chapter 2 that were published in reference [21, 93], including text, figure 1.7, 2.3, 2.4, 2.5, 2.6, 2.7, 2.8, 2.9, and table 2.1.

Title: A Kinetic Rate Model of Novel Upconversion Nanostructures for High-Efficiency Photovoltaics
Author: Eric Y. Chen
Publication: Photovoltaics, IEEE Journal of
Publisher: IEEE
Date: Sept. 2016

Thesis / Dissertation Reuse

The IEEE does not require individuals working on a thesis to obtain a formal reuse license, however, you may print out this statement to be used as a permission grant:

Requirements to be followed when using any portion (e.g., figure, graph, table, or textual material) of an IEEE copyrighted paper in a thesis:

1) In the case of textual material (e.g., using short quotes or referring to the work within these papers) users must give full credit to the original source (author, paper, publication) followed by the IEEE copyright line © 2011 IEEE.
2) In the case of illustrations or tabular material, we require that the copyright line © [Year of original publication] IEEE appear prominently with each reprinted figure and/or table.
3) If a substantial portion of the original paper is to be used, and if you are not the senior author, also obtain the senior author's approval.

Requirements to be followed when using an entire IEEE copyrighted paper in a thesis:

1) The following IEEE copyright/ credit notice should be placed prominently in the references: © [year of original publication] IEEE. Reprinted, with permission, from [author names, paper title, IEEE publication title, and month/year of publication]
2) Only the accepted version of an IEEE copyrighted paper can be used when posting the paper or your thesis on-line.
3) In placing the thesis on the author's university website, please display the following message in a prominent place on the website: In reference to IEEE copyrighted material which is used with permission in this thesis, the IEEE does not endorse any of [university/educational entity's name goes here]'s products or services. Internal or personal use of this material is permitted. If interested in reprinting/republishing IEEE copyrighted material for advertising or promotional purposes or for creating new collective works for resale or redistribution, please go to http://www.ieee.org/publications_standards/publications/rights/rights_link.html to learn how to obtain a License from RightsLink.

If applicable, University Microfilms and/or ProQuest Library, or the Archives of Canada may supply single copies of the dissertation.

BACK | CLOSE WINDOW

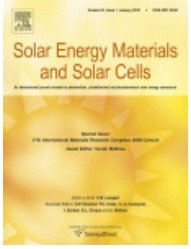

Title: Novel nanostructures for efficient photon upconversion and high-efficiency photovoltaics

Author: Diane G. Sellers,Jing Zhang,Eric Y. Chen,Yujun Zhong,Matthew F. Doty,Joshua M.O. Zide

Publication: Solar Energy Materials and Solar Cells

Publisher: Elsevier

Date: October 2016

From: **Angelo Monguzzi** angelo.monguzzi@unimib.it
Subject: Re: Permission to use a figure
Date: October 17, 2018 at 1:58 PM
To: Jing Zhang zjing@udel.edu

AM

Dear Jing,

Thanks you for your kind email. Of corse, you can use the figure.

Best regards,
Angelo

Il mer 17 ott 2018, 19:36 Jing Zhang <zjing@udel.edu> ha scritto:

> Hi Dr. Monguzzi,
>
> I'm a graduate student from University of Delaware. Can I have the permission to use the figure in the following article in my dissertation?
>
> Figure 1 (a) in " Recent advances in the application triplet–triplet annihilation-based photon upconversion systems to solar technologies" ,
> by *Jacopo Pedrini* and *Angelo Monguzzi*; J. of Photonics for Energy, volume 8, issue 2, 022005 (2017).
>
> The figure will be used in my PhD dissertation and I will credit the SPIE publication.
>
> Thanks,
> Jing

Figure A.1: Permission for figure 1.2

From: **Alla Barancheeva** admin@turpion.ru
Subject: Re: Permission to reuse a figure - Physics-Uspekhi, 2016, 59(8), 727
Date: October 18, 2018 at 9:58 AM
To: Jing Zhang zjing@udel.edu
Cc: Permissions permissions@iop.org

AB

Dear Jing Zhang,

Thank you for providing the details.

On behalf of the Journal's publishers, we are happy to grant a royalty free and non-exclusive permission to you to reproduce Figure 12b published in the article below with a condition that the original article will be credited in your publication:

DOI: https://doi.org/10.3367/UFNe.2016.02.037703
Citation: V A Milichko, A S Shalin, I S Mukhin, A E Kovrov, A A Krasilin, A V Vinogradov, P A Belov, C R. Simovski, "Solar photovoltaics: current state and trends", PHYS-USP, 2016, 59 (8), 727–772

We suppose that the above figure will be reproduced in your PhD dissertation 'Novel Upconversion Nanostructure for High Efficiency Photovoltaics: Theoretical Model and Material Study', to be published at the end of 2018/early 2019, by the University of Delaware.

We grant this permission to reproduce the figure in both print and electronic editions of the dissertation and in all subsequent future editions of the dissertation, any derivative products and in publisher authorised distribution by third party distributors, aggregators and other licensees such as abstracting and indexing services.

Sincerely,

Alla Barancheeva
Office Manager
Turpion-Moscow Ltd
MIAN, 8 Gubkina Street, Room 915
Moscow 119991, Russia

Tel: +7 499 941 0102
Fax: +7 499 941 0103
E-mail: admin@turpion.ru
URL: http://www.turpion.org
****

Thursday, October 18, 2018, 4:29:41 PM, you wrote:

JZ> Hi Alla,

JZ> The title is "Novel Upconversion Nanostructure for High
JZ> Efficiency Photovoltaics: Theoretical Model and Material Study".
JZ> It will be completed before November 2018. I'm not sure when it
JZ> will be made available online. Maybe early next year.

JZ> Thanks,
JZ> Jing

>> On Oct 18, 2018, at 6:30 AM, Alla Barancheeva <admin@turpion.ru> wrote:

>> Dear Jing,

Figure A.2: Permission for figure 1.4.

SPRINGER NATURE LICENSE
TERMS AND CONDITIONS

Oct 30, 2018

This Agreement between University of Delaware -- Jing Zhang ("You") and Springer Nature ("Springer Nature") consists of your license details and the terms and conditions provided by Springer Nature and Copyright Clearance Center.

License Number	4451480994173
License date	Oct 17, 2018
Licensed Content Publisher	Springer Nature
Licensed Content Publication	Nature Photonics
Licensed Content Title	Understanding intermediate-band solar cells
Licensed Content Author	Antonio Luque, Antonio Martí, Colin Stanley
Licensed Content Date	Feb 5, 2012
Licensed Content Volume	6
Licensed Content Issue	3
Type of Use	Thesis/Dissertation
Requestor type	non-commercial (non-profit)
Format	electronic
Portion	figures/tables/illustrations
Number of figures/tables/illustrations	1
High-res required	no
Will you be translating?	no
Circulation/distribution	>50,000
Author of this Springer Nature content	no
Title	Novel Upconversion Nanostructure for High Efficiency Photovoltaics:Theoretical Model and Material Study
Institution name	University of Delaware
Expected presentation date	Nov 2018
Portions	figure 1a
Requestor Location	University of Delaware 201 Du Pont Hall University of Delaware Material science and engineering NEWARK, DE 19716 United States Attn: Jing
Billing Type	Invoice
Billing Address	University of Delaware

Figure A.3: Permission for figure 1.5.

JOHN WILEY AND SONS LICENSE
TERMS AND CONDITIONS

Oct 30, 2018

This Agreement between University of Delaware -- Jing Zhang ("You") and John Wiley and Sons ("John Wiley and Sons") consists of your license details and the terms and conditions provided by John Wiley and Sons and Copyright Clearance Center.

License Number	4451491362815
License date	Oct 17, 2018
Licensed Content Publisher	John Wiley and Sons
Licensed Content Publication	Advanced Optical Materials
Licensed Content Title	Upconversion for Photovoltaics – a Review of Materials, Devices and Concepts for Performance Enhancement
Licensed Content Author	Jan Christoph Goldschmidt, Stefan Fischer
Licensed Content Date	Apr 21, 2015
Licensed Content Volume	3
Licensed Content Issue	4
Licensed Content Pages	26
Type of use	Dissertation/Thesis
Requestor type	University/Academic
Format	Electronic
Portion	Figure/table
Number of figures/tables	1
Original Wiley figure/table number(s)	figure 5
Will you be translating?	No
Title of your thesis / dissertation	Novel Upconversion Nanostructure for High Efficiency Photovoltaics:Theoretical Model and Material Study
Expected completion date	Nov 2018
Expected size (number of pages)	1
Requestor Location	University of Delaware 201 Du Pont Hall University of Delaware Material science and engineering NEWARK, DE 19716 United States Attn: Jing
Publisher Tax ID	EU826007151
Total	0.00 USD
Terms and Conditions	

Figure A.4: Permission for figure 1.8.

From: **Jing Zhang** zjing@udel.edu
Subject: Rightslink® by Copyright Clearance Center
Date: October 17, 2018 at 2:59 PM
To: Udel zjing@udel.edu

JZ

https://s100.copyright.com/AppDispatchServlet#formTop

Copyright Clearance Center RightsLink®

Home | Account Info | Help

ACS Publications
Most Trusted. Most Cited. Most Read.

Title: Broadband Near-Infrared to Visible Upconversion in Quantum Dot–Quantum Well Heterostructures
Author: Ayelet Teitelboim, Dan Oron
Publication: ACS Nano
Publisher: American Chemical Society
Date: Jan 1, 2016
Copyright © 2016, American Chemical Society

Logged in as:
Jing Zhang
University of Delaware
Account #:
3001335449
LOGOUT

PERMISSION/LICENSE IS GRANTED FOR YOUR ORDER AT NO CHARGE

This type of permission/license, instead of the standard Terms & Conditions, is sent to you because no fee is being charged for your order. Please note the following:

- Permission is granted for your request in both print and electronic formats, and translations.
- If figures and/or tables were requested, they may be adapted or used in part.
- Please print this page for your records and send a copy of it to your publisher/graduate school.
- Appropriate credit for the requested material should be given as follows: "Reprinted (adapted) with permission from (COMPLETE REFERENCE CITATION). Copyright (YEAR) American Chemical Society." Insert appropriate information in place of the capitalized words.
- One-time permission is granted only for the use specified in your request. No additional uses are granted (such as derivative works or other editions). For any other uses, please submit a new request.

If credit is given to another source for the material you requested, permission must be obtained from that source.

BACK | CLOSE WINDOW

Figure A.5: Permission for figure 1.9.

ELSEVIER LICENSE
TERMS AND CONDITIONS

Oct 30, 2018

This Agreement between University of Delaware -- Jing Zhang ("You") and Elsevier ("Elsevier") consists of your license details and the terms and conditions provided by Elsevier and Copyright Clearance Center.

License Number	4451500521929
License date	Oct 17, 2018
Licensed Content Publisher	Elsevier
Licensed Content Publication	Progress in Crystal Growth and Characterization of Materials
Licensed Content Title	Quantum dot nanostructures and molecular beam epitaxy
Licensed Content Author	S. Franchi,G. Trevisi,L. Seravalli,P. Frigeri
Licensed Content Date	Jan 1, 2003
Licensed Content Volume	47
Licensed Content Issue	2-3
Licensed Content Pages	30
Start Page	166
End Page	195
Type of Use	reuse in a thesis/dissertation
Intended publisher of new work	other
Portion	figures/tables/illustrations
Number of figures/tables/illustrations	1
Format	electronic
Are you the author of this Elsevier article?	No
Will you be translating?	No
Original figure numbers	figure 1
Title of your thesis/dissertation	Novel Upconversion Nanostructure for High Efficiency Photovoltaics:Theoretical Model and Material Study
Publisher of new work	University of Delaware
Expected completion date	Nov 2018
Estimated size (number of pages)	1
Requestor Location	University of Delaware 201 Du Pont Hall University of Delaware Material science and engineering NEWARK, DE 19716

Figure A.6: Permission for figure 4.1.

JOHN WILEY AND SONS LICENSE
TERMS AND CONDITIONS

Oct 30, 2018

This Agreement between University of Delaware -- Jing Zhang ("You") and John Wiley and Sons ("John Wiley and Sons") consists of your license details and the terms and conditions provided by John Wiley and Sons and Copyright Clearance Center.

License Number	4451500712201
License date	Oct 17, 2018
Licensed Content Publisher	John Wiley and Sons
Licensed Content Publication	Wiley Books
Licensed Content Title	Reflection High-Energy Electron Diffraction
Licensed Content Author	Shuji Hasegawa
Licensed Content Date	Oct 12, 2012
Licensed Content Pages	14
Type of use	Dissertation/Thesis
Requestor type	University/Academic
Format	Electronic
Portion	Figure/table
Number of figures/tables	1
Original Wiley figure/table number(s)	figure 3
Will you be translating?	No
Title of your thesis / dissertation	Novel Upconversion Nanostructure for High Efficiency Photovoltaics:Theoretical Model and Material Study
Expected completion date	Nov 2018
Expected size (number of pages)	1
Requestor Location	University of Delaware 201 Du Pont Hall University of Delaware Material science and engineering NEWARK, DE 19716 United States Attn: Jing
Publisher Tax ID	EU826007151
Total	0.00 USD
Terms and Conditions	

TERMS AND CONDITIONS

This copyrighted material is owned by or exclusively licensed to John Wiley & Sons, Inc. or one of its group companies (each a"Wiley Company") or handled on behalf of a society with which a Wiley Company has exclusive publishing rights in relation to a particular work

Figure A.7: Permission for figure 4.4.

Jing,

Yes, I am very happy for you to reuse the figure. I am glad that you found the slides helpful! Good luck with your dissertation.

Kind Regards,

Scott A Speakman, Ph.D.
Principal Scientist- XRD

Malvern Panalytical
a spectris company

Tel +1 800 279 7297
Mob +1 508 361 8121

Malvern Panalytical Inc.
117 Flanders Road
Westborough MA 01581
United States

scott.speakman@panalytical.com
www.malvernpanalytical.com

Figure A.8: Permission for figure 4.6.

From: **Neels, Antonia** Antonia.Neels@empa.ch
Subject: AW: Permission to reuse a figure
Date: October 18, 2018 at 4:52 AM
To: Jing Zhang zjing@udel.edu

AN

Good Morning,
Yes you can. Best wishes and lots of success, Antonia Neels

Prof. Dr. Antonia Neels, Titular Professor
Head Center for X-ray Analytics
Empa - Swiss Federal Laboratories for Materials Science and Technology
Überlandstrasse 129, 8600 Dübendorf, Switzerland
Tel +41 58 765 45 07 / Mobile +41 79 369 2899
Fax +41 58 765 11 22
antonia.neels@empa.ch
http://www.empa.ch/x-ray
www.empa.ch

Von: Jing Zhang <zjing@udel.edu>
Gesendet: Mittwoch, 17. Oktober 2018 21:37
An: Neels, Antonia <Antonia.Neels@empa.ch>
Betreff: Permission to reuse a figure

Hi Dr. Neels,

I'm a graduate student from University of Delaware. Can I have the permission to use a figure in the following slide in my dissertation?

The figure on page 26 of the lecture slide "High Resolution X-Ray Diffraction" used in the CSEM.

I have attached the slides for your reference. The figure will be used in my PhD dissertation and I will credit the source.

Thanks,
Jing

Figure A.9: Permission for figure 4.9.

From: **Neha Singh** nsingh@jawoollam.com
Subject: RE: Permission to reuse figure
Date: October 17, 2018 at 3:58 PM
To: Jing Zhang zjing@udel.edu

NS

Dear Jing,

Thank you for reaching out to us for the permission. Yes, you are welcome to use the image with credit to J.A. Woollam Company. Please let me know if you have any further questions. Good luck with your dissertation!

Regards,
Neha

Neha Singh
Applications Engineer

J.A. Woollam Co., Inc.
645 M Street, Suite 102
Lincoln, NE 68508 USA
Ph:
Fx:
402.477.7501 x327
402.477.8214

-----Original Message-----
From: Jing Zhang <zjing@udel.edu>
Sent: Wednesday, October 17, 2018 2:55 PM
To: Support <support@jawoollam.com>
Subject: Permission to reuse figure

Hi,

I'm a graduate student from University of Delaware. Can I have the permission to use the following figures in the WVASE manual in my dissertation?

Figure 2.3 and figure 13.70 from "Guide to using WVASE 32".

The figures will be used in my PhD dissertation and I will credit the source.

Thanks,
Jing

Figure A.10: Permission for figure 4.11 and 4.13.

American Physical Society
Reuse and Permissions License

17-Oct-2018

This license agreement between the American Physical Society ("APS") and Jing Zhang ("You") consists of your license details and the terms and conditions provided by the American Physical Society and SciPris.

Licensed Content Information

License Number:	**RNP/18/OCT/008589**
License date:	17-Oct-2018
DOI:	10.1103/PhysRevB.71.045202
Title:	Fully first-principles screened-exchange LDA calculations of excited states and optical properties of III-V semiconductors
Author:	S. H. Rhim et al.
Publication:	Physical Review B
Publisher:	American Physical Society
Cost:	USD $ 0.00

Request Details

Does your reuse require significant modifications: No

Specify intended distribution locations:	United States
Reuse Category:	Reuse in a thesis/dissertation
Requestor Type:	Student
Items for Reuse:	Figures/Tables
Number of Figure/Tables:	1
Figure/Tables Details:	figure 7
Format for Reuse:	Electronic

Information about New Publication:

University/Publisher:	University of Delaware
Title of dissertation/thesis:	Novel Upconversion Nanostructure for High Efficiency Photovoltaics: Theoretical Model and Material Study
Author(s):	Jing Zhang
Expected completion date:	Oct. 2018

License Requestor Information

Name:	Jing Zhang
Affiliation:	Individual
Email Id:	zjing@udel.edu
Country:	United States

Page 1 of 2

Figure A.11: Permission for figure 4.12.

AIP PUBLISHING LICENSE
TERMS AND CONDITIONS

Oct 30, 2018

This Agreement between University of Delaware -- Jing Zhang ("You") and AIP Publishing ("AIP Publishing") consists of your license details and the terms and conditions provided by AIP Publishing and Copyright Clearance Center.

License Number	4451520978779
License date	Oct 17, 2018
Licensed Content Publisher	AIP Publishing
Licensed Content Publication	Applied Physics Letters
Licensed Content Title	Effects of molecular beam epitaxy growth conditions on composition and optical properties of InxGa1−xBiyAs1−y
Licensed Content Author	Y. Zhong, P. B. Dongmo, J. P. Petropoulos, et al
Licensed Content Date	Mar 12, 2012
Licensed Content Volume	100
Licensed Content Issue	11
Type of Use	Thesis/Dissertation
Requestor type	Student
Format	Electronic
Portion	Figure/Table
Number of figures/tables	1
Title of your thesis / dissertation	Novel Upconversion Nanostructure for High Efficiency Photovoltaics:Theoretical Model and Material Study
Expected completion date	Nov 2018
Estimated size (number of pages)	1
Requestor Location	University of Delaware 201 Du Pont Hall University of Delaware Material science and engineering NEWARK, DE 19716 United States Attn: Jing
Billing Type	Invoice
Billing Address	University of Delaware 201 Du Pont Hall University of Delaware Material science and engineering NEWARK, DE 19716 United States Attn: Jing
Total	0.00 USD

Figure A.12: Permission for figure 5.1.

American Physical Society
Reuse and Permissions License

17-Oct-2018

This license agreement between the American Physical Society ("APS") and Jing Zhang ("You") consists of your license details and the terms and conditions provided by the American Physical Society and SciPris.

Licensed Content Information

License Number:	**RNP/18/OCT/008590**
License date:	17-Oct-2018
DOI:	10.1103/PhysRevB.75.045203
Title:	Valence-band anticrossing in mismatched III-V semiconductor alloys
Author:	K. Alberi et al.
Publication:	Physical Review B
Publisher:	American Physical Society
Cost:	USD $ 0.00

Request Details

Does your reuse require significant modifications: No

Specify intended distribution locations:	United States
Reuse Category:	Reuse in a thesis/dissertation
Requestor Type:	Student
Items for Reuse:	Figures/Tables
Number of Figure/Tables:	1
Figure/Tables Details:	figure 4 (a)
Format for Reuse:	Electronic

Information about New Publication:

University/Publisher:	University of Delaware
Title of dissertation/thesis:	Novel Upconversion Nanostructure for High Efficiency Photovoltaics: Theoretical Model and Material Study
Author(s):	Jing Zhang
Expected completion date:	Oct. 2018

License Requestor Information

Name:	Jing Zhang
Affiliation:	Individual
Email Id:	zjing@udel.edu
Country:	United States

Page 1 of 2

Figure A.13: Permission for figure 5.2(a).

SPRINGER NATURE LICENSE
TERMS AND CONDITIONS

Oct 30, 2018

This Agreement between University of Delaware -- Jing Zhang ("You") and Springer Nature ("Springer Nature") consists of your license details and the terms and conditions provided by Springer Nature and Copyright Clearance Center.

License Number	4451521268175
License date	Oct 17, 2018
Licensed Content Publisher	Springer Nature
Licensed Content Publication	Springer eBook
Licensed Content Title	Dilute Bismuthides on an InP Platform
Licensed Content Author	Yujun Zhong, Pernell Dongmo, Joshua Zide
Licensed Content Date	Jan 1, 2013
Type of Use	Thesis/Dissertation
Requestor type	academic/university or research institute
Format	electronic
Portion	figures/tables/illustrations
Number of figures/tables/illustrations	1
Will you be translating?	no
Circulation/distribution	<501
Author of this Springer Nature content	no
Title	Novel Upconversion Nanostructure for High Efficiency Photovoltaics:Theoretical Model and Material Study
Institution name	University of Delaware
Expected presentation date	Nov 2018
Portions	figure 4.1
Requestor Location	University of Delaware 201 Du Pont Hall University of Delaware Material science and engineering NEWARK, DE 19716 United States Attn: Jing
Billing Type	Invoice
Billing Address	University of Delaware 201 Du Pont Hall University of Delaware Material science and engineering NEWARK, DE 19716 United States

Figure A.14: Permission for figure 5.2(b).

AIP PUBLISHING LICENSE
TERMS AND CONDITIONS

Oct 30, 2018

This Agreement between University of Delaware -- Jing Zhang ("You") and AIP Publishing ("AIP Publishing") consists of your license details and the terms and conditions provided by AIP Publishing and Copyright Clearance Center.

License Number	4451521444393
License date	Oct 17, 2018
Licensed Content Publisher	AIP Publishing
Licensed Content Publication	Applied Physics Letters
Licensed Content Title	Contactless electroreflectance study of E0 and E0 ΔSO transitions in In0.53Ga0.47BixAs1−x alloys
Licensed Content Author	R. Kudrawiec, J. Kopaczek, J. Misiewicz, et al
Licensed Content Date	Dec 19, 2011
Licensed Content Volume	99
Licensed Content Issue	25
Type of Use	Thesis/Dissertation
Requestor type	Student
Format	Electronic
Portion	Figure/Table
Number of figures/tables	1
Title of your thesis / dissertation	Novel Upconversion Nanostructure for High Efficiency Photovoltaics:Theoretical Model and Material Study
Expected completion date	Nov 2018
Estimated size (number of pages)	1
Requestor Location	University of Delaware 201 Du Pont Hall University of Delaware Material science and engineering NEWARK, DE 19716 United States Attn: Jing
Billing Type	Invoice
Billing Address	University of Delaware 201 Du Pont Hall University of Delaware Material science and engineering NEWARK, DE 19716 United States Attn: Jing
Total	0.00 USD

Figure A.15: Permission for figure 5.3.